Winter 2013

# A Polymer-Based Microfluidic Device with Electrolyte-Enabled Distributed Transducers (EEDT) for Distributed Load Detection

Peng Cheng
*Old Dominion University*

# A POLYMER-BASED MICROFLUIDIC DEVICE WITH ELECTROLYTE-ENABLED DISTRIBUTED TRANSDUCERS (EEDT) FOR DISTRIBUTED LOAD DETECTION

by

Peng Cheng
B.S. July 1996, Xi'an Mining Institute, China
M.S. July 2008, Xi'an University of Science and Technology, China

A Dissertation Submitted to the Faculty of
Old Dominion University in Partial Fulfillment of the
Requirements for the Degree of

DOCTOR OF PHILOSOPHY

MECHANICAL ENGINEERING

OLD DOMINION UNIVERSITY
December 2013

Approved by:

Zhili Julje Hao (Advisor)

Han Bao (Member)

Gene Hou (Member)

Michael Stacey (Member)

# ABSTRACT

## A POLYMER-BASED MICROFLUIDIC DEVICE WITH ELECTROLYTE-ENABLED DISTRIBUTED TRANSDUCERS (EEDT) FOR DISTRIBUTED LOAD DETECTION

Peng Cheng
Old Dominion University, 2013
Advisor: Dr. Zhili Julie Hao

The capability of detecting distributed static and dynamic loads is indispensable in a wide variety of applications, such as examining anatomical structures of biological tissues in tissue health analysis and minimally invasive surgery (MIS) and determining the texture of an object in robotics. This dissertation presents a comprehensive study of a polymer-based microfluidic device with electrolyte-enabled distributed transducers and demonstrates a new concept on using a single microfluidic device for distributed-load detection, which takes advantage of the low-cost microfluidic fabrication technology and the low modulus and biocompatibility of polymer. The core of the device is a single deformable polymer microstructure integrated with electrolyte-enabled transducers. While distributed loads are converted to different levels of deflections by the polymer microstructure, the deflections of the microstructure are translated to resistance changes by the five pairs of distributed transducers underneath the microstructure. Firstly, the design and working principle of the device is described. Then, due to its simple but efficient configuration, a standard fabrication process well developed for polydimethylsiloxane(PDMS)-based microfluidic devices is detailed and employed to fabricate this device. After that, the experimental setups for characterizing the device performance in static, step and sinusoidal inputs are illustrated. The experimental data then are collected and processed by using custom-built electronic circuits and custom

LabVIEW/Matlab program to characterize the device performance. Lastly, the performance analysis of the device is conducted to obtain the performance parameters such as device sensitivity and load resolution. In summary, this polymer-based microflidic device not only demonstrates the new concept and the capability of detecting distributed static and dynamic loads with a single device, with a thorough experimental study on the performance and characterization of this PDMS-based microfluidic device to correlate the device performance to its design parameters, but also the potential application of directly adopting this experimental method to measure the elasticity/viscoelasticity of a soft tissue.

# ACKNOWLEDGMENTS

I would like to express my sincere gratitude to my Ph.D. advisor, Dr. Julie Zhili Hao, for her tremendous support and for offering me this excellent opportunity in graduate research. Her extensive knowledge, creative thinking and assiduous research attitude have guided me throughout my research work. Without her guidance and persistent help, this dissertation would not have been possible.

I would like to express my gratitude to Dr. Han Bao, Dr. Gene Hou, and Dr. Michael Stacey for taking an interest in my work and serving on my Ph.D. dissertation committee. I would like to thank Dr. Ali Beskok for taking an interest in my proposal. It has been a privilege to benefit from their feedback and advice in the construction of my dissertation.

I would like to express my appreciation to the members of the entire research group, for their help and useful discussions. Thanks go to Wenting Gu, Jiayue Shen, providing a friendly and stimulating atmosphere in research, as well as brightening the long hours spent in the lab. Their help benefitted me both academically and socially. The home-like atmosphere made the research work easier. Thanks also go to Yuxi Liao for his support on circuit design and Arindam Ghosh for his training on device fabrication.

Also, many thanks go to Diane Mitchell and June Blount for all their administrative help.

This dissertation is dedicated to my wife Yanan Wang and my daughter Yixuan Cheng for their unselfish sacrifice, enormous patience, and full support throughout the completion of my Ph. D degree.

# NOMENCLATURE

*Abbreviations:*

AFM: Atomic Force Microscopy

DMA: Dynamic Mechanical Analysis

EEDT: Electrolyte-Enabled Distributed Transducers

EMIDCA: 1-Ethyl-3-methylimidazolium dicyanamide electrolyte

FEA: Finite Element Analysis

MEMS: Micro-electro-mechanical System

MIS: Minimally Invasive Surgery

PCB: Printed Circuit Board

PDMS: Polydimethylsiloxane

PVDF: Polyvinylidene fluoride

*Notation:*

$L_d$: Length of the device

$b_d$: Width of the device

$h_d$: Thickness of the device

$w_E$: Top plate width of microstructure

$b_E$: Width of the PDMS microstructure

$d_E$: Length of an individual segment

$h_M$: Top-plate thickness of microstructure

$a$: Length of the microchannel

$b$: Width of the microchannel

$h_E$: Height of the microchannel

$d_E$: Transducer spacing

$E$: Young's modulus of PDMS

$\upsilon$: Poisson's ratio of PDMS

$\rho$: Density of PDMS

$Q$: the mechanical quality factor of the microstructure

$\omega_d$: the angular natural frequency of the microstructure

$k_d$: the stiffness of the microstructure

$\rho_v$: Density of EMIDCA

$\rho_E$: Electrical resistivity of EMIDCA

$\mu_E$: Viscosity of EMIDCA

# TABLE OF CONTENTS

Page

# LIST OF TABLES

# LIST OF FIGURES

# CHAPTER 1

# INTRODUCTION

Detecting static and dynamic loads has a wide variety of applications in biomedical, biological, robotics and industrial automation fields [1, 2]*, such as examining anatomical structures of biological tissues in tissue health analysis and minimally invasive surgery (MIS), and determining the texture of an object in robotics. In general, many devices focus on single point detection [3], but in most cases, the detection of non-uniform distributed loads is needed, especially in micro or millimeter scale [4, 5]. Therefore, the capability of detecting distributed static and dynamic loads is especially indispensable since distributed loads is a more common loading condition and cannot be avoided in MIS, robotics, etc. Meanwhile, the spatially-varying elasticity/viscoelasticity or the heterogeneous property of a tissue specimen can be detected more efficiently under distributed loads.

## 1.1 Background

To detect the static or dynamic loads, a deformable microstructure is needed and a transduction mechanism is also necessary to convert the mechanical deformation to a detectable electronic signal, an optical signal or other form of signals. In a microfluidic device, polymer-based microstructure is widely chosen to generate the mechanical deformation, and electrolyte-enabled transducers are selected to convert the mechanical deformation to detectable electrical signal.

* This thesis follows the IEEE style documentation.

As a part of microfluidic device, polymer-based mechanical microstructure is widely used to form microchannels or microchambers, which allow the flow of the micro-fluids. In recent years, microfabrication technology makes it possible to precisely control the fabrication process to fabricate a predefined polymer-based mechanical structure with microchannels or microchambers. Moreover, polymers consist of large covalently bonded molecules, making them an ideal material for engineering structural building in measurement techniques. A polymer-based microfluidic device contains this mechanical structures and microchannels or microchambers, which can be filled with fluids or electrolyte, according to the different purpose of applications, to do the property measurement or external loading detection. Thus, polymer-based devices are widely used in commercial and engineering fields, with the higher possible aspect ratios, advantages of disposability, loss cost, weight savings and ease to fabricate [6, 7].

In this dissertation, electrolyte-enabled transducers are used to convert the mechanical deformation to electrical signal. It is known to all that a transducer is a device or component which can transfer the energy from one form to another, such as conversion of the mechanical deformation to electrical signal or in other way round. Furthermore, electrolyte-enabled transducers use electrolyte as the medium to convert the mechanical deformation to electrical signal because electrolyte is a conductive compound with ionized solution or sometimes organic solution, also because of its incompressibility and fluidity. After electrolyte is filled into the microchannel under the microstructure, the electrolyte together with a pair of electrodes forms a transducer. A few kinds of transducers aligned along the microchannel will compose an electrolyte-enabled distributed transducers (EEDT).

A few different types of devices can be utilized to detect static and dynamic loads according to the transduction mechanism of the devices such as capacitive sensors, resistive sensors, piezoresistive sensors, piezoelectric sensors and inductive sensors [1-3]. Every type of device has different transduction mechanism. For example, capacitive sensors use the change of capacitance to detect the external loads but resistive sensors utilize the change of resistance. Also, every different type of device has its own advantages and drawbacks. For instance, capacitive sensors have excellent sensitivity, good spatial resolution and large dynamic range, but are easily disturbed by environmental noises [1-3]. For resistive sensors, they have good sensitivity, low cost and good sensing range, but one of the problems is the non-linearity. Piezoelectric sensors also have high sensitivity and high dynamic range, but cannot be used for static sensing [1-3]. Table 1.1 compares the transduction mechanisms of three types of widely used sensors and their advantages and disadvantages.

Table 1.1 Comparison of three widely used sensors

| Type | Mechanism | Advantages | Disadvantages |
|---|---|---|---|
| Capacitive sensors | Change in capacitance | Excellent sensitivity;<br>Good spatial resolution;<br>Large dynamic range. | Noises susceptible;<br>Complexity of measurement electronics. |
| Resistive sensors | Change in resistance | Good sensitivity;<br>Low cost ;<br>Good sensing range. | Non-linearity. |
| Piezoelectric sensors | Strain(stress) polarization | High sensitivity;<br>High dynamic range. | Dynamic sensing only. |

These above mentioned sensing devices can be used in many fields such as biomedical and biological fields as well as robotics and industrial automation [1, 2]. If these devices are designed to mimic the sense of touch of human beings or detect and collect information through the touch of certain area of the samples, they can be called tactile sensing devices [3], no matter what kinds of transduction mechanism are used. Devices can be resistive, piezoresistive or capacitive tactile sensors. With the development of micro-fabrication methods such as photolithography and plasma bonding, tactile sensing technology becomes a feasible technology, and the materials it used extend from silicon to various polymers because polymer materials have their advantages including low elastic strength, biocompatibility and removal of the need for protective packaging.

## 1.2 Applications of load detection

Through detecting non-uniform distributed loads, sensors can be widely used to determine the surface texture of an object or classify the objects [1, 4, 8], examine anatomical structures of tissues [2, 3, 5], provide haptic feedback in heterogeneous biomedical studies [2, 9-12], or analyze elasticity or viscoelasticity of a biomaterial or soft materials [13-22]. These applications mainly attracted attentions from biomedical and medical field especially in minimally invasive surgery (MIS) and tissue health diagnostics fields, as well as robotic fingertips in robotic fields and manufacturing industries automation [23-28].

One example for the application of classification is the paper from Drimus et al. [4]. They presented a piezoresistive-based tactile-array sensor. This sensor has two flexible

PVC substrates and a sandwiched piezoresistive rubber layer with the conductive tread electrodes. When the device is fixed on a gripper and grasps the objects, according to the haptic feedback, they can classify and recognize the objects.

Kimotoet al. [8] demonstrated a piezoelectric tactile sensor using polyvinylidene fluoride (PVDF) films for material identification. This sensor is fixed to a robotic arm which is used to apply force to the samples that is set on the black acrylic plate. The robotic arm with the tactile sensor is vertically moved down to press the samples. Because of the piezoelectric effects, mechanical force is converted to the voltage output, and this output is used to identify the materials. There are a few drawbacks of the piezo type of sensors. One of the drawbacks of this device is that the piezo material is very sensitive to the temperature, and will introduce noises to the device. Another disadvantage is piezoelectric sensors can just measure dynamic force but not static force.

Examining anatomical structures of tissues is normally applied in minimally invasive robotic surgery. For instance, an optical fiber tactile sensor is elaborated by Ahmadi et al. [5]. This sensor has the ability of detecting heterogeneous tissues when minimally invasive robotic surgery is processed. They assemble a distributed-load sensor that is comprised of a polycarbonate beam and three optical transducers (fibers) underneath the beam. When a probe is utilized to press a tissue specimen against the beam, the optical transducers record the continuous distributed deflection of the beam at three discrete locations along the beam length. From one measurement, the relative deflection magnitude of the beam can identify the existence of a lump/tumor or abnormality in the tissue. This distributed-load sensor is shown in Figure 1.1. This MRI compatible design just uses a simple structure to detect the hidden anatomical structure

under both the static and dynamic loading condition. This work is perhaps the only study on using a single device to examine spatially-varying mechanical properties of a material. Since this device is manually assembled, its miniaturization and batch fabrication becomes challenging.

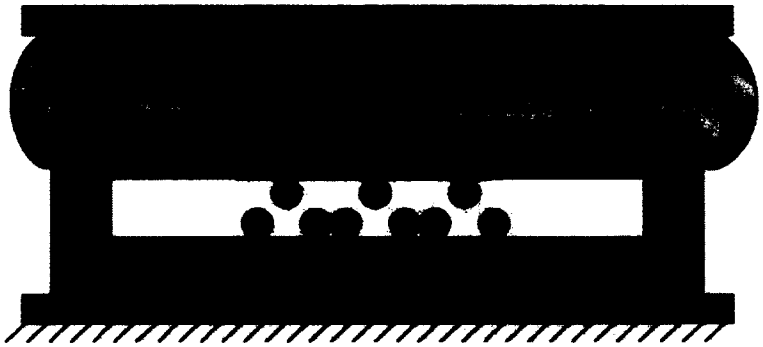

Figure 1.1 A schematic view of a distributed-load sensor with a hyperelastic tissue. [5]

An example of the application for providing haptic feedback in minimally invasive surgery is the work from King et al. [9]. They provide a tactile feedback system which contains a very important element, a piezoresistive force sensor. This piezoresistive force sensor can sense the force and give a feedback to the system when the whole system is turned on, and then the system could adjust the grip force from a very high level to a proper level.

A few papers [13-22] are focusing on the measurement of elasticity or viscoelasticity of a material and various experimental techniques have been developed for measuring the mechanical properties of soft biomaterials and soft biological tissues at the micro-scale [18-20].

Hohne et al. [13] demonstrated a flexible microfluidic device to analyze viscoelasticity of a biomaterial. A thin polydimethylsiloxane (PDMS) membrane is utilized to detect the deformation of the specimen which is put underneath the PDMS device when a fixed pressure is applied to the air channel of the PDMS device. The membrane deflection further is monitored by a confocal laser scanning microscope.

Peng [14] demonstrated a novel capacitance device which can be used for both normal and shear modulus measurement. There are several cells in a device, and one cell of this PDMS-based device contains two metal layers, an isolator layer with some supporting pillars, a bump on the top, and some air spaces in the middle between two electrode layers allowing the deflection of the microstructure. Figure 1.2 shows the schematic view of a single tactile cell of the device. The drawbacks of this device are the fabrication complexity and the noise treatment due to the instinctive property of the capacitance sensor.

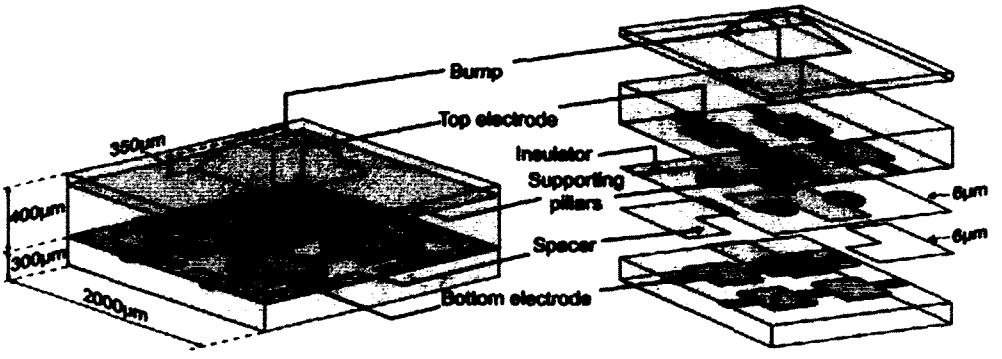


Figure 1.2 Schematic diagram of a single tactile cell of the proposed stiffness sensor. [14]

Static nanoindentation techniques based on atomic force microscopy (AFM) [18, 20] and customized micro/nano-probes [20-22] have also been developed to measure elasticity of a specimen, and their dynamic counterparts have been developed to measure viscoelasticity of a specimen through conducting quasi-static, stress relaxation, and dynamic mechanical analysis (DMA) tests [19, 22]. The measured experimental data are translated to elasticity/viscoelasticity of a specimen through related formulas [19] or finite element analysis [22].

Since heterogeneity at the micro-scale is inherent to native soft biological tissues and cell-seeded scaffolds in tissue engineering [19], measuring the spatially-varying elasticity/viscoelasticity of such materials is critically important for revealing the physiological process and functionality of native and engineered tissues, as well as metabolic activities of cells [19, 29]. Toward this end, nanoindentation experiments need to be conducted across a specimen in a sequential manner for mapping out its spatially-varying elasticity/viscoelasticity and thus do not allow efficient acquisition of such measurement data [30, 31]. Figure 1.3 shows the schematic view of an indentation of a biological sample by using a triangle probe from Zhu et al. [18] to illustrate the static nanoindentation techniques based on atomic force microscopy (AFM).

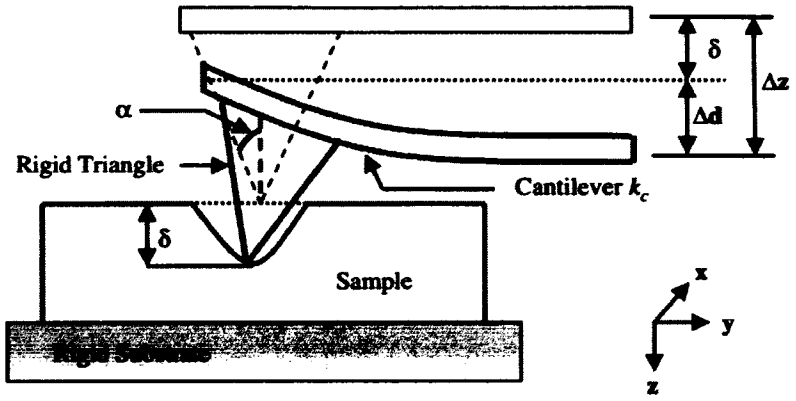


Figure 1.3 A schematic view: indentation of a biological sample by a triangle probe. [18]

Meanwhile, micro-electro-mechanical System (MEMS)-based devices have recently been developed to measure elasticity of soft materials [15-17]. As compared with nanoindentation techniques, these MEMS-based devices have the potential of being mounted on a handheld probe for in situ elasticity measurement. Although a 2D array of these MEMS-based devices would allow measuring the spatially-varying elasticity of a specimen [16], no such results have so far been reported in the literature. Moreover, these MEMS-based devices require rather complicated fabrication processes, including multiple etchings, depositions and bondings, and thus result in high fabrication costs and non-disposability [15-17].

As shown in Figure 1.4, Fath El Bab et al. [17] shows a micromachined piezoresistive tactile sensor with two serpentine springs and 500-μm cubic mesas. This sensor uses the stiffness differences between two springs and soft tissue for compliance detection.

Figure 1.4 Specimen chip with two equal serpentine springs. [17]

## 1.3 Current research status of microfluidic devices for load detection

The realization and application of microfluidic devices are well known for various biological and chemical applications [32] to analyze the fluids or particles in microchannels. Although different devices have various configurations, they all comprise polymer microstructures with microchannels or microchambers, electrodes, electronic connections and embedded electrolyte. The microchannel with electrolyte will be deflected in response to an external change such as load or internal change such as particles in the electrolyte. This deflection will be converted to impedance change which is the function of the cross-section of the microchannel or microchambers.

One example of analyzing the particles in microchannels is Jagtiani et al. [33]. They demonstrated a microfluidic multichannel sensor to count the high throughput. 30μm polystyrene particles were suspended in a 0.154M NaCl solution and pressure-driven flowed from one side of the device to another side passing through a 50μm-width microchannel. The principle of the device is that the resistance between each pair of

electrodes will change in a very short time and form an output pulse when a particle passes through the microchannel. By counting the pulses, they can count the micro particles.

Recently, microfluidic devices have been studied for detecting the load, especially for single-load. The principle of these devices primarily relies on the resistive or capacitive changes while pressures or forces are applied on the devices, and these resistive or capacitive changes are the function of the electrolyte cross section. Certainly, microstructures are still needed to form the microchannels and microchambers which allow the flow of the liquid or electrolyte. For microfluidic devices, the building material is a big concern. Because of the advantages mentioned before, polymer becomes commonly utilized building material of the microstructure. Among many different polymers, polydimethylsiloxane (PDMS) [34] is one of the most commonly used building materials. PDMS has some very important characters such as biocompatibility, non-conductivity and low cost. It can also be easily patterned using standard fabrication technologies such as photolithography, or bonded with glass substrate using oxygen plasma bonding.

A few papers show that PDMS-based sensors with embedded microfluidic structure. One example is Gutierrez et al. [26]. They developed a parylene-base force sensor which contains an electrolyte-filled parylene microstructure, a pair of micro-fabricated thin-film electrodes and fluidic access port and channel. This parylene-base impedance sensor can detect very small force (about 10mN). It demonstrated the capability of force measurement using electrochemical impedance and also showed the potential application of examining human tissues. But the disadvantages of this device involve complex

fabrication process and operation only in aqueous environments due to the method of electrolyte immersion. Also because this device only has one pair of electrodes, they need to use an array for distributed load measurement, and this will introduce the fabrication complexity and the difficulties of electronic connection.

Tseng et al. [27] demonstrated a PDMS/polyimide multilayer structure for mimicking the slow-adapting receptors in human skin. This sensor contains a hemispheric microchamber filled with 1M NaCl electrolyte and an initially empty microchannel. It is designed to detect the impedance change through the resistance change of the electrolyte solution between a pair of electrodes. The downside of this device is the inability to detect distributed loads in a single device since this device has just only one pair of electrodes. Also the electrolyte filling is complex since it needed to be operated in a vacuumed environment.

Park et al. [28] also developed a PDMS resistance-based pressure sensor encompassing a PDMS microchannel filled with conductive liquid eutectic gallium-indium (eGaIn). This device can detect the surface pressure by using the cross-section change of the microchannel and this change causes the resistance change of the electrical resistance between the electrodes. This paper showed great fabrication simplicity because they just used a maskless soft lithography and didn't need to deposit the electrode layer. This device also showed an ease of electrolyte filling by using a syringe for filling. The microstructure they used is PDMS based polymer and the electrolyte is a conductive liquid called eutectic gallium-indium (eGaIn). Because of a lack of electrodes, they avoided the electrolyte-electrode interface effect, but also because of the lack of

electrodes, this device cannot distinguish the location of the pressure or force, and therefore, cannot be used to detect the distributed force along microchannel.

Nie et al. [35] demonstrated a novel droplet-based pressure sensor which can measure blood pressure. This capacitive sensor has a very simple structure and also a pretty simple fabrication process. When the device is applied on the surface of the human skin throughout cardiovascular cycles, the blood pressure will cause the capacitance changes of the electrolyte, and the output can be read from the electronic connection. This device has the ability to detect the dynamic blood pressure but failed to detect the distributed force.

Wu et al. [36] also elaborated a pressure sensor with integrated ionic liquid-based electrofluidic circuits and fabricated with PDMS-based microstructure using soft lithography process. This device is a resistive sensor based upon the changes of the resistance of the electrolyte with the cross-section and the circuit can transfer the resistance change to the voltage output. The disposability and effective cost are the advantages; but still, this device can just measure the pressure of a point and cannot be used to detect the distributed load.

All these microfluidic devices mentioned above could detect external load and convert the deflection of the microstructure to the impedance change, but only for point load detection. In many practical applications, in order to acquire the details of heterogeneous biological materials in biomedical studies [2, 5], the capability of detecting distributed loads at the micro-millimeter scale is necessary. This requirement is not just for biomedical field but also for the robotic application to determine the texture

of an object [1, 24, 37]. Therefore, the lack of the capability of detecting distributed loads will limit the application of the above mentioned devices.

In order to make up the lack of detecting distributed load, array can be used to do the detection. But normally, this will introduce the difficulty of fabrication. Wong et al. [38] elaborated a flexible microfluidic normal force sensor. This sensor takes advantage of capacitive sensors, using a 5×5 taxel array with liquid metal-filled microfluidic channels to measure the capacitance change, and then to detect the normal force at the range of 0 to 2.5N. This device is fabricated with several PDMS layers using soft lithography techniques, injected conductive fluid Galinstan and bonded together using Oxygen plasma.

Another example of microfluidic sensors using array is the device presented by Wettels et al. [39]. They developed a microfluidic tactile sensor array that can detect the force ranging from 0.1N to 30N. This device embedded the conductive fluid and mimicked the human touch receptors of the fingertip. It consists of a rigid finger core which looks like a finger shape and the electrodes are located on its surface. The sensor array is utilized to detect the deformations of the electrolyte in different locations, and these deformations can be converted to the impedance changes. Since the fabrication process is mold-based process, the size of the device is relatively large, and the spatial resolution (2mm) is relatively low.

## 1.4 Motivation

Among the above mentioned devices, some can only detect a point load [28, 36] and some can detect dynamic force but failed to detect the static forces [8, 14, 35]. Some

introduced the fabrication complexity [26], and some need to be operated in a vacuumed environment [27] or need to deal with the noise [14]. The only study on using a single device to examine spatially-varying mechanical properties of a material is manually assembled, so it cannot be batch fabricated and thus cannot be disposable [5]. All of these factors will introduce the difficulties of detection of distributed loads and limit the applications.

In order to efficiently detect both the static and the dynamic distributed loads for measuring the spatially-varying elasticity/viscoelasticity of a soft specimen, or the other potential of applications such as the heterogeneity of a tissue in micro scale in biomedical studies, at the same time as simplifying the fabrication process and lowing the cost, a simple designed, easy fabricated and low cost device is needed. To this end, a polymer-based microfluidic device with electrolyte-enabled distributed transducers (EEDT) is designed and fabricated.

Compared with those above mentioned MEMS-based sensor arrays and the assembled distributed-load sensor, our PDMS-based microfluidic device features great fabrication simplicity and low cost, thus promising to be disposable [40]. Conversely, compared with nanoindentation techniques, this device allows efficient acquisition of spatially-varying elasticity/viscoelasticity of a specimen. The advantages of this design, compared with the above mentioned other type of sensors or different design, are the capability of detecting distributed loads in one single device, great fabrication simplicity, ease of electrolyte filling, and the adaptability of operating in various conditions and ambient such as dry and aqueous environments.

This dissertation is aimed to achieve the following goals: 1) to demonstrate the feasibility and capability of detecting distributed load using this polymer-based microfluidic device with EEDT. 2) to establish an experimental method for characterization of the device performance under different types of inputs such as static, step and sinusoidal input signals and, 3) to relate the device performance to the device design parameters.

## 1.5 Scope of the dissertation

In this dissertation, a PDMS-based microfluidic device with an embedded electrolyte-filled microchannel is demonstrated to show the ability of detecting distributed loads. Also a proof-of-concept demonstration is made to illustrate the common applications in biomedical [5], robotics [37], food processing and manufacturing fields [13]. One potential application of this device is to measure spatially-varying elasticity/viscoelasticity of a heterogeneous soft material. The core of this design is a sensing platform which contains a polymer-based microstructure integrated with electrolyte-enabled distributed transducers. A microchannel under the microstructure is filled with electrolyte and fabricated using standard lithography procedure. Underneath the microchannel, five pairs of distributed electrodes align along the microchannel length and a pyrex substrate supports the whole structure. This device is then bonded to the printed circuit board (PCB), which connects the input AC voltage and the custom-built electronic circuit. When external loads are applied, the microstructure generates deflections. These deflections cause resistance changes which can be detected by five pairs of impedance transducers. Because of the resistance changes, the output of the

signal from the circuit also changes, and the output data can be collected and processed by a custom-built LabVIEW program. Above all, this device can be tailored and scaled up easily for measuring soft materials with elasticity/viscoelasticity in different ranges and heterogeneity varying at different feature sizes at the micro-scale, without sacrificing its fabrication simplicity and ease of operation.

Evidently, these devices not only are aimed to demonstrate the feasibility of detecting distributed loads using a single device, but also provide a thorough experimental and analytical study on the device performance under different loading conditions such as static, step and sinusoidal loading condition. Before these devices can be utilized to measure a specimen, their performance needs to be examined and characterized under static, step and sinusoidal loading inputs, since these inputs correspond to those for measuring elasticity/viscoelasticity of a specimen through quasi-static, stress relaxation and DMA tests.

The rest of the dissertation is organized as follows.

Chapter 2 describes the design and working principle of the PDMS-based microfluidic device. It provides fundamentals of this device including device configuration, device design, polymer rectangular microstructure and electrolyte-based distributed transducers.

Chapter 3 focuses on the fabrication process of the polymer-based microfluidic device with EEDT. Two masks are used to fabricate the device, with one for the electrodes fabrication and another one for the PDMS structure fabrication. Also, a plasma bonding process is needed to bond the PDMS structure and the electrodes together.

Chapter 4 presents the experimental setup and method. In this chapter, two different experimental setups are described: one is the experimental setup for static analysis and step function analysis using a micropositioner as the input of displacements. And the other setup is the one for dynamic analysis using a shaker to generate a sinusoidal input. The measurement method will also be clarified in this chapter.

Device characterization is demonstrated in Chapter 5. In this chapter, three different signal inputs are used to generate static, step or dynamic responses. According to the different inputs, data from these three different outputs are collected and plotted. This chapter will use these outputs and figures to characterize the device.

In Chapter 6, after the device characterization, device performances are analyzed to get the parameters of the device such as device spatial resolution, load resolution and the sensitivity of the device.

Finally, Chapter 7 is the conclusion of this research, providing an the overview of the contributions and possible future works in this polymer-based microfluidic device with electrolyte-enabled distributed transducers (EEDT) for distributed load detection.

# CHAPTER 2

# DESIGN AND WORKING PRINCIPLE

## 2.1 Device configuration and working principle

To enable detecting the distributed static and dynamic load, A PDMS-based microfluidic device with electrolyte-enabled distributed transducers is designed. Figure 2.1 shows a schematic view of this simple single device which consists of a pyrex substrate slide, a polydimethylsiloxane (PDMS) polymer rectangular microstructure, an electrolyte-filled microchannel with reservoirs embedded in the microstructure, and five pairs of electrodes equally spaced along the microstructure length. Across the microchannel width, five pairs of electrodes with electrolyte-filled microchannel function as five distributed transducers, which can record the resistances of the portion of electrolyte between the two opposing electrodes [33, 40, 41]. Above the microchannel, the PDMS microstructure has excellent pliability, flexibility and elasticity, and allows the distributed loads to apply on the top of the structure without damaging the device. For the ability of injecting the electrolyte into the channel and confining the electrolyte within the device, two reservoirs at the ends of the microchannel are utilized due to the incompressibility of the electrolyte. Thus, these two reservoirs not only completely confine electrolyte within the device, but also allow electrolyte to freely flow during the device operation.

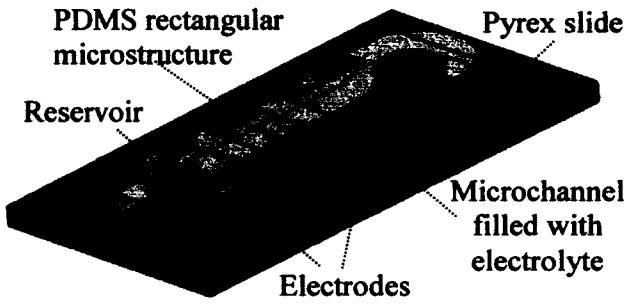


Figure 2.1 Schematic view of the PDMS-based microfluidic device.

Table 2.1 shows the dimension and some key design parameters of the PDMS-based microfluidic device with EEDT. Since the microstructure and microchannel are most important parts for device, some key parameters for them also are shown in this table. It should be noticed that the top plate thickness of the microstructure will vary for different devices because of the fabrication variation.

The embedded electrolyte-filled microchannel together with five pairs of electrodes formed five transducers.

Table 2.2 lists the physical properties of PDMS [42] and 1-Ethyl-3-methylimidazolium dicyanamide electrolyte (EMIDCA) (H26901-06, Alfa Aesar) [36], which is the electrolyte used in the device.

Table 2.1 Dimension and key design parameters of the PDMS-based device

| Geometrical design parameter | symbol | value |
|---|---|---|
| *Device* | | |
| Length of the device | $L_d$ | 22mm |
| Width of the device | $b_d$ | 15mm |
| Thickness of the device | $h_d$ | 2.2mm |
| *Microstructure* | | |
| Top plate width | $w_E$ | 1mm |
| Width of the PDMS microstructure | $b_E$ | 6mm |
| Length of an individual segment | $d_E$ | 1.5mm |
| Top-plate thickness | $h_M$ | 1mm~3mm |
| *Microchannel* | | |
| Length of the microchannel | $a$ | 12000μm |
| Width of the microchannel | $b$ | 1000μm |
| Height of the microchannel | $h_E$ | 80μm |
| Transducer spacing | $d_E$ | 1500μm |

Table 2.2 Physical properties of PDMS and EMIDCA

| Physical property | Symbol | Value |
|---|---|---|
| *PDMS* | | |
| Young's modulus | $E$ | 350kPa |
| Poisson's ratio | $\upsilon$ | 0.45 |
| Density | $\rho$ | 1000kg/m$^3$ |
| *EMIDCA* | | |
| Electrical resistivity | $\rho_E$ | 0.2Ω·m |
| Viscosity | $\mu_E$ | 0.021Pa·s |
| Density | $\rho_v$ | 1.06g/cm$^3$ |

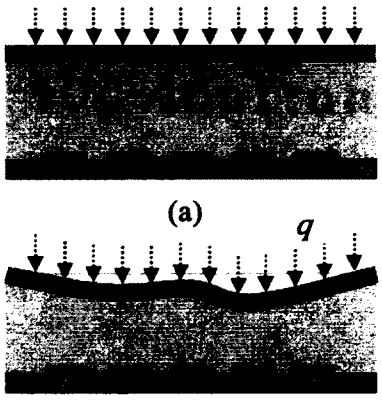


Figure 2.2 (a) side view of microchannel (b) when non-uniform distributed loads applied.

Figure 2.2 describes the operation principle of the device. When distributed loads $q$ are applied along vertical direction on the top of the PDMS microstructure, because of the deflection of the microstructure, the electrolyte inside of the microchannel will get squeezed and the microchannel will be deformed. This deformation will cause the change of the cross-section's area, and therefore, will cause the resistance change of each transducer. In a different location, if the distributed loads are non-uniform, five distributed transducers will detect different resistance changes. This device here can only detect one-dimensional (1D) distributed loads, and it can be easily modified by adding several microchannels in parallel to detect two-dimensional (2D) distributed loads. It should be noticed that spatial resolution in this device can be determined by transducer spacing, which is the distance between each pair of electrodes.

Figure 2.3 illustrates the side view and top view of device to show the working principle, with its key design parameters being symbolized. While the microstructure converts continuous distributed loads to continuous z-axis deflection along its length (x-

axis), the distributed transducers translate the continuous deflection to discrete resistance changes at specific locations along the microstructure length. During operation, partial electrolyte in the microchannel flows into the reservoirs and thus alleviates the time delay for detection of dynamic loads.

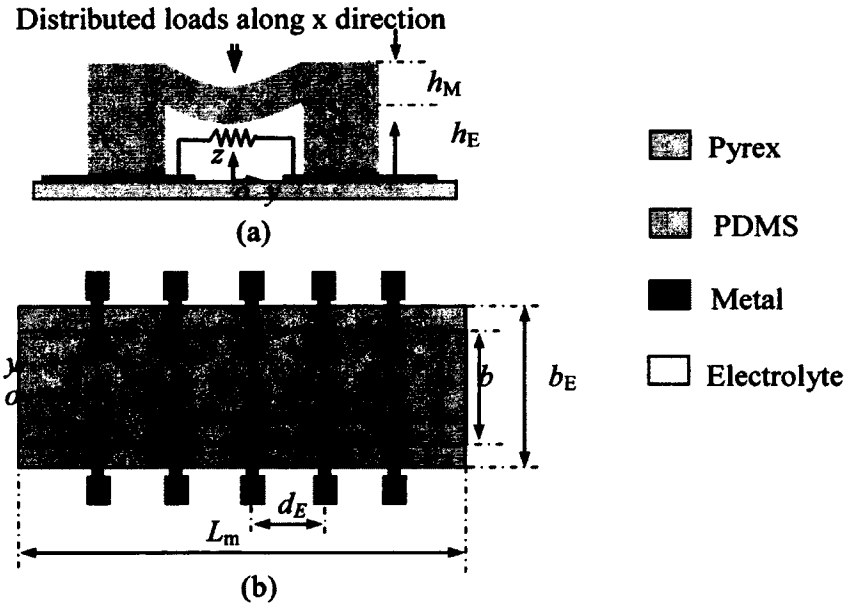


Figure 2.3 Working principle of the device (a) Side view and (b) top view.

Figure 2.4 illustrates one potential application of the device for measuring spatially-varying elasticity/viscoelasticity of a soft material. A specimen is placed on the device, and a rigid probe is utilized to press the specimen against the device with precisely controlled displacements. Consequently, the spatially-varying elasticity or viscoelasticity of the specimen is captured by the continuous distributed loads acting on the microstructure and is further recorded by the distributed transducers. For elasticity measurements, different static probe displacements can be applied to the specimen, and

then spatially-varying elasticity of the specimen registers as continuous distributed static loads acting on the device. For viscoelasticity measurement, different types of the probe displacement need to be exerted on a specimen for conducting quasi-static, stress relaxation and DMA tests [43, 44].

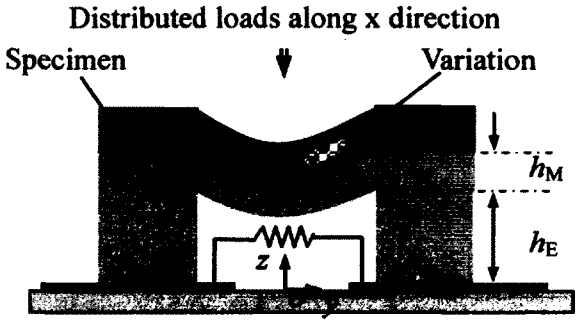


Figure 2.4 Schematic of measuring the spatially-varying elasticity/viscoelasticity of a specimen using the PDMS-based microfluidic device.

## 2.2 Device design

### 2.2.1 Polymer rectangular microstructure

The polymer rectangular microstructure, which is located above the microchannel, can be divided into two rigid sidewalls and a rectangular compliant top plate. During the operation, two rigid sidewalls experience longitudinal deflection and the top plate undergoes flexural deflection. The deflection of the rigid sidewalls is much smaller than the deflection of the top plate, so it can be neglected. Therefore, the top plate can be treated as a spring and the load-to-deflection conversion of the microstructure is solely determined by its stiffness. To correlate the stiffness of the microstructure to its design

parameters, as shown in Figure 2.5, the microstructure can be approximately treated as five identical segments with a length of $d_E$, whose centers coincide with the locations of their electrode pairs, and each segment is treated as a spring with an identical stiffness of $k_d/5$, with $k_d$ representing the overall stiffness of the microstructure. Consequently, the key geometrical design parameters of the microstructure are the transducer spacing, width and thickness of the top-plate.

By treating a segment as a rectangular thin-plate, the stiffness of a segment is related to the device design parameters by [45]:

$$\frac{k_d}{5} \propto \frac{E h_M^3 d_E}{(1-\upsilon^2) w_E^3} \tag{1}$$

where $E$ and $\upsilon$ denote the Young's modulus and Poisson's ratio of PDMS, respectively. Here, it must be emphasized that the input of the device is the applied displacement of a rigid probe and it is equal to the microstructure deflection. Then, by simplifying the microstructure as a spring, the resulting overall load, $F_d$, acting on the microstructure can be obtained by:

$$F_d(z_p) = k_d \cdot z_p \tag{2}$$

The load acting on a segment, $F$, is approximately one fifth of the overall load, $F = F_d/5$. Effective length of a resistive transducer is $d_{eff} \approx d_E/2$ and the length of an isolation zone is $d_{iso} \approx d_E/2$ as shown in Figure 2.5.

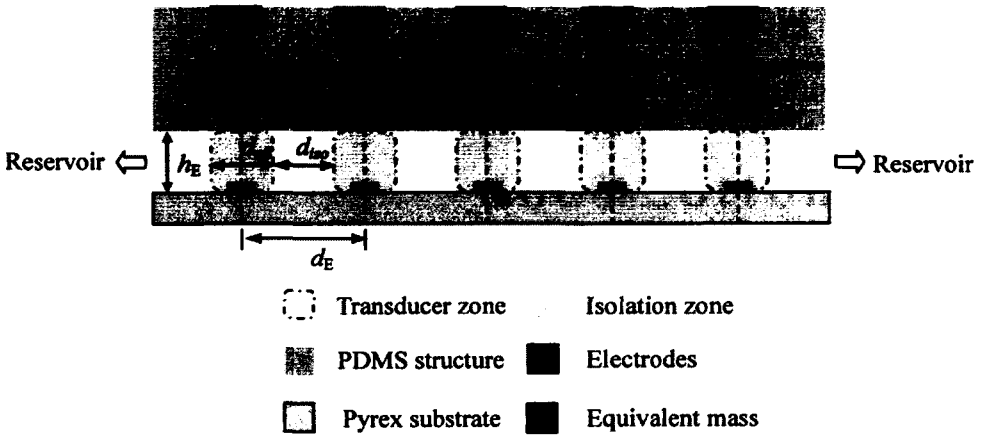


Figure 2.5 Schematic of the identical segments of the microstructure and discrete resistive transducers realized by one body of electrolyte in the microchannel.

### 2.2.2 Electrolyte-based distributed transducers

As mentioned before, this PDMS-based microfluidic device comprises of five transducers which are formed by five pairs of electrodes with the electrolyte across the microchannel. These five transducers can be treated as five impedances. Each pair of electrode can be simplified as impedance $Z_s$, including a resistor $R_s$ and a capacitor $C_s$. There are also electrolyte-electrode interfaces between the electrolyte and electrodes. Every single electrolyte-electrode interface can be treated as a double layer capacitor, $C_{dl}$, and a charge transfer resistor, $R_{ct}$, in series [26, 27]. The impendence of each electrolyte-electrode interface can be denoted as $Z_{DL}$.

The impedance of a transducer is written as:

$$Z = 2Z_{DL} + Z_s \tag{3}$$

where

$$Z_{DL} = R_{ct} + \frac{1}{j\omega C_{dl}} \tag{4}$$

where $\omega$ denotes the frequency of the AC voltage signal, $v_{ac}(\omega)$, which is applied to electrodes during operation.

Compared to the impedance that generated by electrolyte, the impedance of the electrolyte-electrode interfaces are small enough to neglect if an appropriate electrolyte and operation frequency are chosen. Meanwhile, a higher operation frequency can also reduce the effect of the capacitance and the resistance will dominate. In this high frequency range, the impedance will not change much due to that the capacitance will be almost zero, leaving the transducer of each pair of electrodes a resistor. It should be noticed that resistive sensing is chosen due to the interference from the working environment when capacitive sensing is used [1]. Figure 2.6 shows the equivalent circuit for a single pair of electrode as a resistor.

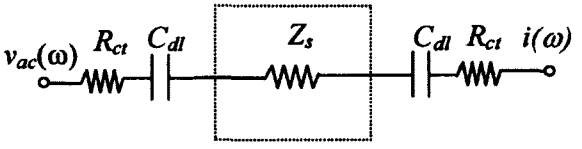


Figure 2.6 Equivalent electrical circuit across one pair of electrodes of the PDMS-based microfluidic resistive sensor.

As mentioned before, in high frequencies, for example $f = 100kHz$, the capacitor has very low impedance and the resistor will dominate the device. Here, five pairs of electrodes can be treated as five independent impedances because the crosstalk between electrodes can be ignored when the transducer spacing is larger than the microchannel width ($d_E > w_E$), so each impedance of the device will approximately be equal to

$$Z_R \approx R_S \propto \frac{\rho_E w_E}{d_E h_E(z_p)}$$

where $\rho_E$ is the electrical conductivity of the electrolyte; $d_E$ is the transducer spacing, or the distance between two neighboring transducers; $w_E$ is the width of the microchannel and $h_E$ is the microchannel height, which is the function of the deflection of the microstructure at the location of the transducer.

When distributed loads are applied, the electrolyte in the microchannel flows into the two reservoirs because of the incompressibility of the electrolyte. This free flow of the electrolyte allows the change of the microchannel height under the distributed loads, and then changes the resistance of the each transducer. Five pairs of metal pads of the device, which connect to the electrodes from one side, will be connected to the PCB board from the other side using wire bonding machine, and the change of the outputs will be also detected by the custom PCB board. Here, the key design parameters of the transducers are the width, height and transducer spacing of the microchannel. It's worth mentioning that the microchannel width and transducer spacing coincide with the top plate width and segment length. One body of electrolyte in the microchannel is utilized to realize the distributed transducers for monitoring the continuous deflection at different locations along the microstructure length.

As shown in Figure 2.5, a resistive transducer is realized by a portion of electrolyte with its center coinciding with its electrode pair, and an isolation zone exists between two neighboring transducers. The effective length of both a transducer, $d_{eff}$, and an isolation zone, $d_{iso}$, is roughly half the transducer spacing, $d_{eff} \approx d_E/2$ and $d_{iso} \approx d_E/2$. The discrete distributed transducers are connected in parallel.

Prior to subjecting to an applied displacement, the initial resistance, $R_0$, of a transducer is calculated as:

$$R_0 = \frac{\rho_E \cdot w_E}{d_{eff} h_E} \tag{5}$$

Upon subjecting to an applied displacement, $z_p$, the resistance, $R(z_p)$, of a transducer becomes a nonlinear function of this applied displacement:

$$R(z_p) = \frac{\rho_E \cdot w_E}{d_{eff}.h_E} \cdot \frac{1}{1 - \frac{z_p}{h_E} \cdot \eta} = \frac{R_0}{1 - \frac{z_p}{h_E} \cdot \eta} \tag{6}$$

where $\eta < 1$ is a coefficient for taking non-uniform deflection across a segment of the top plate into account. Therefore, the resistance change, $\Delta R$, of a transducer is a function of the applied displacement:

$$\Delta R(z_p) = R_0 \cdot \left( \left( 1 - \frac{z_p}{h_E} \cdot \eta \right)^{-1} - 1 \right) \tag{7}$$

From Equation (7), it is easy to see the $\Delta R - z_p$ relation is nonlinear, therefore, the $\Delta R - F_d$ relation which is established by combining Equation (2) and (7) is also nonlinear:

$$\Delta R(F_d) = R_0 \cdot \left( \left( 1 - \frac{F_d}{k_d \cdot h_E} \cdot \eta \right)^{-1} - 1 \right) \tag{8}$$

Under a uniform distributed load, the $\Delta R - F$ relation can be rewritten as

$$\Delta R(F) = R_0 \cdot \left( \left( 1 - \frac{5F}{k_d \cdot h_E} \cdot \eta \right)^{-1} - 1 \right) \tag{9}$$

where $F$ denotes the load acting on a segment. In terms of the device response to an applied displacement or an overall load, the sensitivity of the device from a transducer is given by the slope of the $\Delta R - z_p$ relation or the slope of the $\Delta R - F_d$ relation, respectively:

$$S_{z_p} = \frac{d\Delta R}{dz_p} = R_0 \frac{\eta / h_E}{\left(1 - z_p \eta / h_E\right)^2} \ (Unit: \Omega/\mu m) \tag{10}$$

$$S_{F_d} = \frac{d\Delta R}{dF_d} = R_0 \frac{\eta}{k_d h_E \left(1 - \frac{F_d \eta}{h_E k_d}\right)^2} \quad (Unit: \Omega/\mu N) \tag{11}$$

It is clear that, due to the nonlinearity of the $\Delta R - z_p$ relation, the sensitivity of the device is a function of the applied displacement or the overall load. Under a uniform applied displacement input, the sensitivity of a segment to an applied displacement is identical to Equation (10), but the sensitivity of a segment to its own load is five times of that of the device in Equation (11). However, for a non-uniform load, different segments will have different loads, so the resistance change and sensitivity of each segment will be different.

# CHAPTER 3

# FABRICATION PROCESS

Fabrication technology such as micromachining is mainly used in semiconductor field to create the integrated circuits. Normally, a multiple-step sequence of process steps such as photolithography and chemical treatment is involved. Even though silicon is the dominant material for semiconductor products and most of the MEMS devices, it is still not an ideal material for microfluidic devices due to its cost and poor biocompatibility. Instead, owing to low cost, clarity, easy fabrication and biocompatibility, polydimethylsiloxane (PDMS) has become one of the most commonly used building materials for microfluidic devices[34, 46]. Polydimethylsiloxane, or PDMS, more specifically, with properties like unusual rheological properties, non-toxicity and non-flammability, is an optically clear, silicon-based organic polymer. PDMS contains two components: silicone elastomer curing agent and silicone elastomer base. Before mixing, they are in liquid form; they will be in a solid state after being mixed by specific ratio and cured in certain temperature.

In comparison with silicon-based microfabrication process, polymer-based fabrication process is simpler and does not require so much precision. Normally, only a few masks are needed to make the microstructure, microchannel and electrodes. For our devices, to reduce the complexity of fabrication process and to increase the robustness of the device, the related fabrication process should be well-developed and easily-fabricated. Meanwhile, the advantages of the microfabrication technology should be taken to achieve the batch fabrication and to make the device low cost and disposable.

Therefore, the fabrication process based upon photolithography and plasma bonding for this PDMS-based microfluidic device with EEDT is quite simple. Basically, the fabrication process for our devices involves three steps: deposition of the metal layer, PDMS microstructure fabrication, and device bonding. In each step, several stages are introduced to achieve the fabrication requirement such as mask layout, photolithography process or patterning, and plasma bonding.

## 3.1 Mask layout

In order to pattern electrodes to a pyrex slide or make a mold for microstructure, masks, or photo masks, are utilized to transfer a defined pattern to thin films through controlling the dose of UV light in certain range of wavelength. This process is photolithography or mask lithography, which is borrowed from semiconductor industry to pattern the metal or other layers on printed circuit boards. Masks are normally made on Soda Lime glass, Fused Silica (Quartz) or on polyester film with opaque or transparent areas that allow UV light to penetrate in a predefined pattern. The device is not very small, and the smallest feature of the structure is around 100μm. Thus, polyester film gives us enough precision and accuracy of the pattern geometry, as well as a lower cost. Accordingly, transparencies, which are made of polyester film, are selected as the material for masks. In this polyester film, some areas are black coated and other areas are bare areas. These bare areas allow the light to shine through while the black areas block the light. So the bare areas will be the exposed areas.

Normally, photoresist, which is sensitive to the light and can change the material property when it is exposed to UV light, is evenly spin-coated to the pyrex slides first. Then the coated pyrex slides are put under the UV light with the mask covering them.

According to the designed structure and predicted fabrication process, one positive resist S1800 and one negative photoresist SU-8 50 are utilized for patterning five pairs of electrodes and microstructure mold respectively.

In this design, two masks were designed to make five pairs of electrodes and the SU-8 mold for patterning the microstructure. The first mask that was used to pattern the sacrificial layer of photoresist was a reversed pattern of electrodes. When this mask was put on top of the Pyrex slide with photoresist on it, this reversed pattern was exposed and transferred to the photoresist. Figure 3.1(a) shows the pattern of the first mask which was drawn using software AutoCAD. In this pattern, five pairs of electrodes with five pairs of metal pads that are used for the wire connections can be clearly seen.

Figure 3.1 (b) shows the pattern of the second mask that is used to transfer the pattern to SU-8 photoresist to make a mold for the device's microchannel. Because SU-8 is a negative photoresist, a reversed pattern is drawn in AutoCAD in order to pattern and make a mold. This pattern of mold includes a microchannel, which has a length of 12mm and a width of 1mm, and two reservoirs at the two ends of the microchannel.

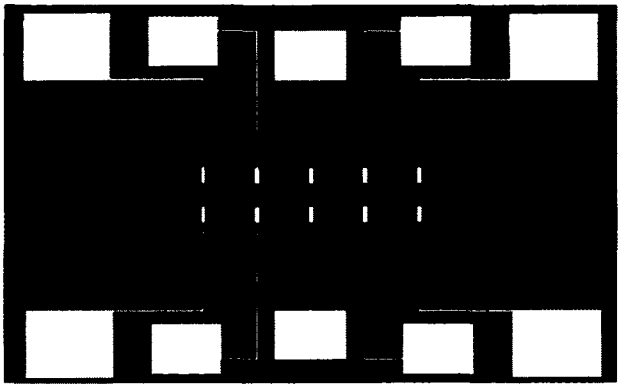

(a)

(b)

Figure 3.1 The AutoCAD pattern of two masks for (a) electrodes (b) microchannel.

## 3.2 Fabrication process

### 3.2.1 Electrodes fabrication

Five pairs of electrodes were fabricated using sputtering process. First, preparation of Pyrex slides was needed in order to thoroughly clean the glass substrate. Pyrex slides were prepared and cleaned by using Potassium hydroxide (KOH) in ultrasonic cleaner for 10 minutes, and put into acetone in ultrasonic cleaner for 10 minutes. Then, the Pyrex slides were rinsed using isopropyl alcohol and DI water respectively. Lastly, they were dried by using Nitrogen gas.

When the Pyrex slides were ready, a sacrificial positive photoresist S1800 layer was spin-coated on top of the Pyrex slides in a spin speed of 500rpm for 10 seconds and 2000rpm for 30 seconds. After the slides were soft baked at temperature of 90°C for 1 minute and hard baked at 90°C for 1 minute, the first mask was utilized for patterning and creating an inverse pattern of five pairs of electrodes using Exoteric 405nm UV Flood Source for 5 seconds at attenuation 3, which has an energy density of 11.74mW/cm$^2$. Then the photoresist was developed using developer MF24 and the inverse pattern was formed.

Before the next step, the slides were put into the oxygen plasma machine to be thoroughly cleaned again. Also, this step is a good preparation for sputtering process to get a better adhesion of the metal layer.

The next step is the sputtering process to deposit the target metals for electrodes. The sputtering equipment we used was EMITECH K675X Turbo Large Chromium Coater. By using predefined program, 10nm-thick Cr was sputtering deposited on the patterned Pyrex slide, and then the 100nm-thick Au was deposited as well.

The last step is washing out the sacrificial layer of photoresist and extra metal layer using lift-off process. Because the sacrificial photoresist was already patterned, some parts of the target metal directly contacted with the substrate glass slide and others covered the sacrificial photoresist layer. In this step, the metals which covered the sacrificial photoresist were washed out with the photoresist, and the directly contacted parts were remained and patterned. It should be noticed that the washing out process should be done in ultrasonic cleaner for at least 10 minutes to get rid of the unwanted

metal parts. The five pairs of metallic electrodes on a Pyrex slide finally were formed by using this liftoff process. The electrodes fabrication process is shown in Figure 3.2.

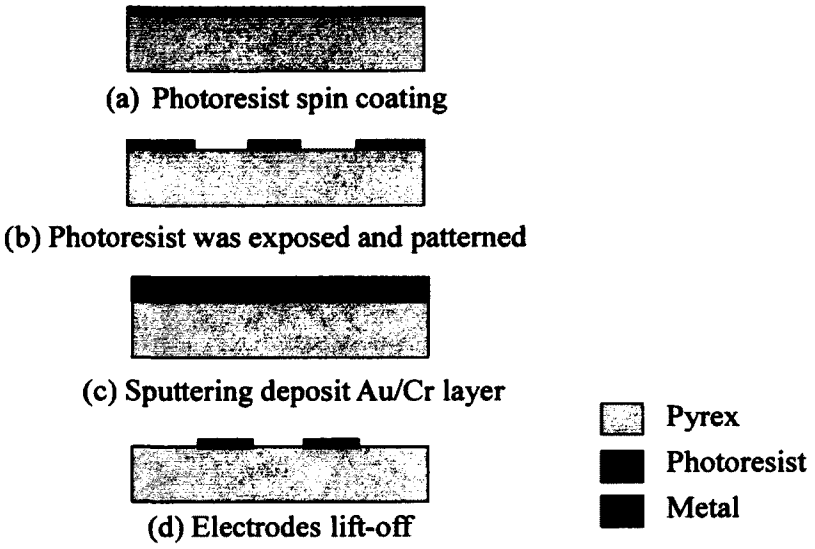


Figure 3.2 Fabrication process of the electrodes using liftoff process.

### 3.2.2 PDMS structure fabrication

Another pretreated Pyrex slide was used to make a SU-8 mold for the microchannel of the device. Since the needed microchannel is about 80μm thick, a material that can be spun or spread over to get a thickness ranging up to 100 micrometer should be chosen. Because SU-8 is a viscous polymer and commonly used epoxy-based negative photoresist, it is a very good material for making a mold. Here SU-8 50 series is utilized on Pyrex slide for 80μm thick mold.

First step is spin-coating. SU-8 50 is statically dispensed to the center of the slide and let to rest for 30 seconds. Then spin coating 500rpm for 5 seconds and 1500rpm for

30 seconds. This slide with SU8 is then pre-baked at 65°C for 10minutes and soft-baked at 95°C for 30 minutes.

The next step is the exposure. Different photoresists have different absorption spectra. For SU-8, it absorbs well at 365nm. So, this time the equipment here we used is an i-line Karl Suss MJB3 mask aligner. According to the thickness of SU-8, type of mask aligner, and required exposure energy, the calculated exposure time is about 15 seconds. After 15 seconds of exposure, post exposure bake (PEB) #1 is applied at 65°C for 1 minute and PEB #2 at 95°C for 10 minutes.

Developing is the last step of SU-8 mold fabrication. SU-8 developer is utilized to develop the slide for 5 minutes. Because SU-8 is a negative photoresist, the unexposed part will be developed and the exposed part will be the microchannel pattern. Isopropyl and DI water is then utilized to clean the slide, and the slide with the SU-8 mold is ready to use after the slide is dried with a gentle stream of nitrogen.

After the mold is formed, the mixture of 10:1 ratio of PDMS elastomer base to curing agent (Sylgard 184kit, Dow Corning Corp.) is poured over the mold and cured at room temperature to form the PDMS rectangular microstructure. It needs to be noticed that a hot plate can be used to cure the PDMS microstructure, but a de-bubble process should be used to make the PDMS structure bubble free afterwards. This process can be omitted in room temperature since the cure process will be 24 hours long, and the bubbles will escape from the PDMS mixture in such a long time period. Finally the PDMS structure is cured and peeled off from the SU8 mold. This technology of pouring the PDMS base and curing agent to a mold to form the microstructure also can be called soft lithography, which refers to fabricate structures by using soft material like PDMS.

Compared with the traditional lithography, this technology has several advantages: low cost, suitable for biological, plastic material and much thicker structures. Figure 3.3 shows the fabrication process of the SU-8 mold.

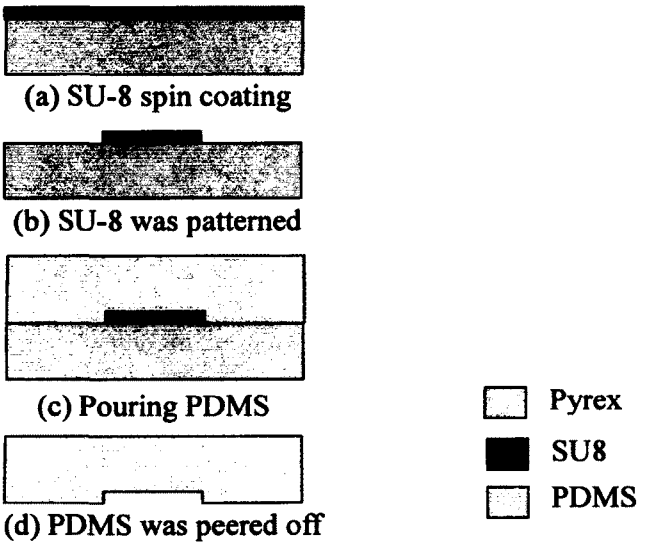


Figure 3.3 Fabrication process of the SU-8 mold.

### 3.2.3 Device bonding

Once the electrode slide and PDMS structure are ready, the plasma bonding process is applied to assemble the device and seal the PDMS and the glass slide tightly. First, the electrode slide and PDMS structure are cleaned using ethanol in ultrasonic cleaner for about 10 minutes. Then, place all the parts on the hot plate at 130°C for 5 minutes to dehydrate the components. After that, all the device components are put into the oxygen plasma chamber. When the chamber is vacuumed, the valve of oxygen gas is turned on for 1 minute, and the plasma power is turned on to high level. It needs 1 minute to get

exposed in oxygen plasma when the plasma becomes bright, uniform, and stable. Then the power and oxygen gas should be shut down and the air should be in.

After taking the device parts out, the microchannel of PDMS structure should face up under the microscope and ready to bonding and seal. Pick the electrode slide and let the electrode face downward, gently push the electrode slide to the PDMS structure and align them precisely. It should be noticed that the height of the microchannel is very small, only 80μm. Thus, avoiding applying large pressure is very necessary to make sure not to collapse the microchannel. After bonding, put this new device on top of the hot plate and cure it about 5 minutes at 130°C. Thus the PDMS microstructure and the Pyrex slide with patterned 5 pairs of electrodes are bonded together. Figure 3.4 shows the bonding process of the PDMS-based microfluidic device with EEDT and Figure 3.5 shows the three-dimension bonding process of the PDMS-based microfluidic device with EEDT.

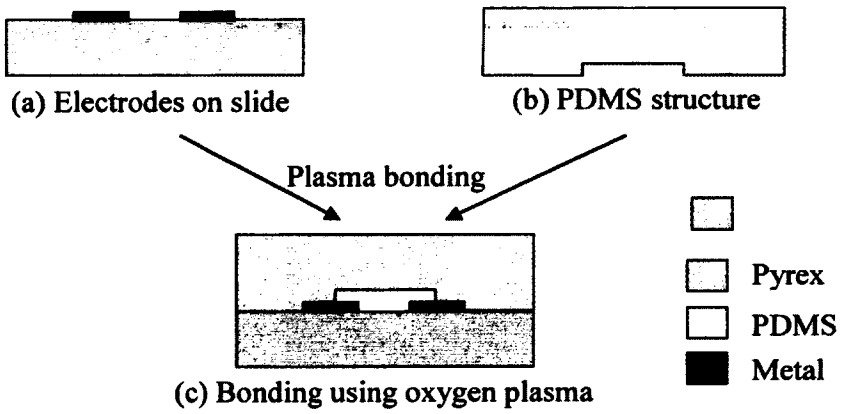


Figure 3.4 Bonding process of the PDMS-based microfluidic device with EEDT.

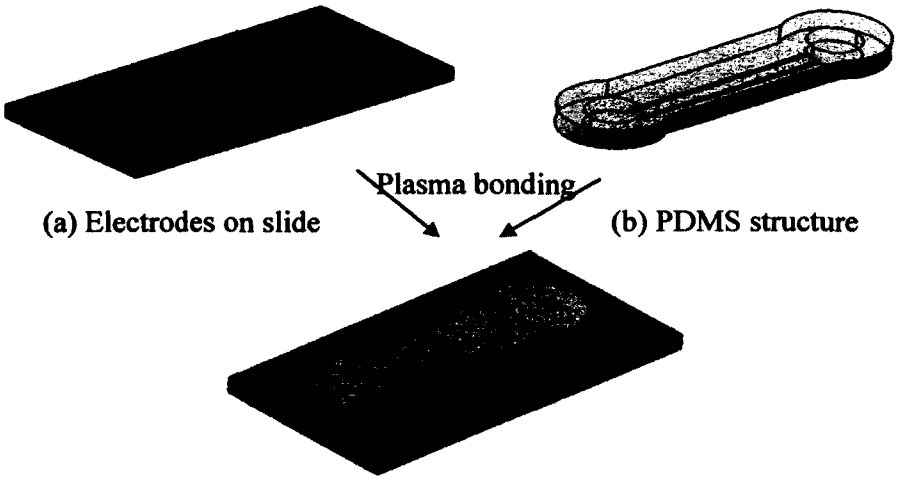


Figure 3.5 3D bonding process of the PDMS-based microfluidic device with EEDT.

### 3.3 Electrolyte filling and electrical connection

After the device is fabricated, two holes are drilled into each reservoir to fill with electrolyte solutions using a syringe and these holes can be further optionally connected to tubes to avoid leakage during the operation.

An ionic liquid named 1-Ethyl-3-methylimidazolium dicyanamide (98%), or EMIDCA, is used as the electrolyte for its low viscosity (17 mm/s 25 °C), high conduct (27ms/cm) and considerable large electrochemical window (5.9V) [47]. Actually, before EMIDCA is used, 0.1mol NaCl was used as electrolyte, and the results will be shown in chapter 5 for comparison and feasibility check. According to the experiments, the first problem 0.1mol NaCl electrolyte has is evaporation. This electrolyte cannot remain in a liquid form for a long time, and the output value will slowly change during the experiments because the electrolyte concentration changed with its evaporation. Besides

an evaporation problem, another problem of NaCl electrolyte is electrolysis. After a period of operation, NaCl electrolyte will deteriorate the electrodes, making the device fail to operate. In contrast, because EMIDCA has features of free of evaporation, high fluidity, good conductivity, and perfect stability, devices filled with EMIDCA exhibits much better performance than the devices that filled with NaCl.

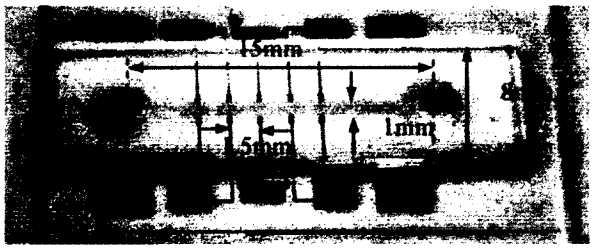


Figure 3.6 Picture of a fabricated PDMS-based microfluidic device with EEDT

Figure 3.6 shows the fabricated device, which is filled with colored liquid for illustrating the microchannel and reservoirs. This PDMS-based microfluidic device has an approximately dimension of 25mm×10mm×2mm and the microchannel has a dimension of 12mm×1mm×80μm. The PDMS microstructure has a length of 25mm and a width of 8mm. The transducer spacing, or spatial resolution, is 1.5mm. Several critical parameters will decide the sensitivity of the device, and one of them is the thickness of the PDMS layer above the microchannel. This parameter can be controlled by pouring different amount of PDMS into the mold, so the thickness of the microstructure will vary among different devices, normally between 1mm~3mm. The distance between the centers of the two reservoirs is 15mm. The five pairs of electrodes extend to outside of the

PDMS structure, forming five pairs of metal pads which allow the wire bonding connection between the device and the PCB board using wire-bonding machine.

# CHAPTER 4

# EXPERIMENTAL SETUP AND METHOD

The experimental setup of this PDMS-based microfluidic device with EEDT and the experimental method is shown in this chapter. For better performance, the experimental setup needs to be characterized carefully to reduce the influences from the setup itself. Meanwhile, for different performances such as static or dynamic behavior, the setup will vary according to the input differences. Also, in this chapter, the experimental method is specified in order to get efficient and accurate output data.

## 4.1 Experimental setup

The whole experimental setup for this PDMS-based microfluidic device with EEDT is shown in Figure 4.1. It contains a few parts: a device fixture system including optical table, a 5-axis manipulator and bonding PCB (printed circuit board), an input system which comprises a function generator and a micropositioner or a vibration shaker, an assembled stack of the probe holder, load cell and probe, an electrical circuit with five identical PCBS and a data collection system such as custom PCBs, DAQ board and LabVIEW program.

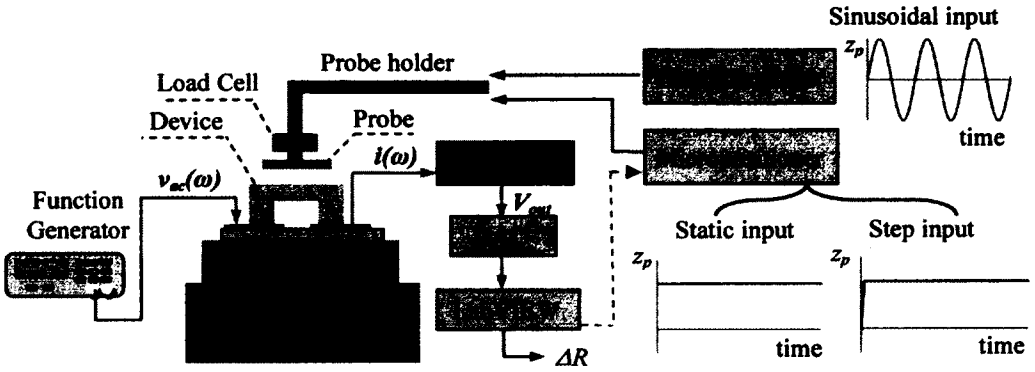


Figure 4.1 The schematic view of experimental setup.

The first part of the setup is the fixture system for the device. As shown in Figure 4.2, the device is firstly mounted on a custom PCB, which is designed to connect the electrodes of the device to metal pads of PCB using wire bonding machine. This wire bonding PCB also connects the input sinusoidal signal which is generated from the function generator to the device. Moreover, it connects the device to the circuits to get the output. Then this PCB is fixed on a 5-axis manipulator on the optical table to assure the stability of the operation. Here, this 5 axis manipulator, which can be seen in Figure 4.3 and Figure 4.4, functions as an adjustable plat form or stage. This manipulator (NBM513, NanoBlock 5-Axis Waveguide Manipulator with Differential Drive Actuators from Thorlabs) has five degrees of freedom for motion in micro scale, which is *x*, *y*, *z*, pitch and yaw, so it can be easily used to adjust the device location to touch the probe in a proper position. It also realizes the precise alignment in pitch and yaw direction to reduce the tilt problem.

Figure 4.2 The PCB for connecting the device to input AC voltage and the circuit.

The second part is the input system. Figure 4.3 and Figure 4.4 show two different displacement input setups for static and step input and dynamic input respectively. As shown in Figure 4.3, the micropositioner is used to perform the static and step analysis. In both static and step measurement, micropositioner MP-285 with custom probes is used to precisely control the displacement with a resolution of 0.2μm. This micropositioner also can be controlled by a custom LabVIEW program, and the input of displacement can be converted to the electrical signal by the device. The device itself also has an input source from function generator, which generates an input signal to cross through the microchannel of the device. After the displacement is applied by the micropositioner, the amplitude of the output signal will change due to that the electrolyte is squeezed, and therefore the resistance of the transducers gets changed.

In dynamic analysis, a shaker is used to replace the micropositioner and generate the vibration wave with different frequencies. This shaker is controlled by another function generator with amplifier to get the dynamic displacement input. The whole setup for dynamic analysis is shown in Figure 4.4.

Figure 4.3 Experimental setup for static and step analysis with a micropositioner.

Figure 4.4 Experimental setup for dynamic analysis with a shaker.

The third part is the probing system. The whole stack of the probing system consists of a long probe holder, which is called probe holder #1, a piezo type load cell (Kistler-9712B5), probe holder #2, and the most important part: custom probe. The long probe holder or probe holder #1 is used to connect the micropositioner or shaker to the load cell, and probe holder #2 is utilized to connect the load cell and hold the custom probe. Here, this load cell can capture the overall load experienced by the device, which results from the applied displacement of the probe. A custom probe is shown in Figure 4.5 and Figure 4.6. From Figure 4.5, the length of this rigid probe is 11mm and from the schematically side view of this probe in Figure 4.6, it has a radius of 0.792mm and a height of 1.448mm. It can be mounted on the probe holder #2 and then fixed to either a micropositioner or a vibration shaker to press against the device, with specific applied displacements precisely controlled by the micropositioner or the shaker.

Figure 4.5 An assembled stack of the probe holder, load cell and probe.

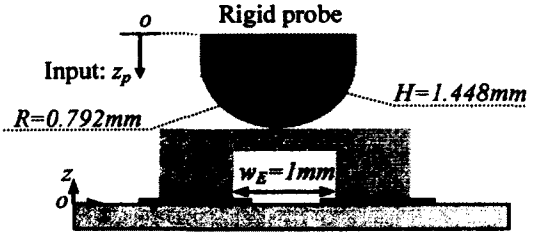


Figure 4.6 A side view of the custom probe.

The fourth part of the setup is the electronic circuit. An AC voltage is generated from function generator HP33220A, separated to five identical inputs, and connected to all the electrodes on one side of the device, while electrodes on the other side of the device are connected to their own circuit implemented on PCBs for converting AC current signals to DC voltage outputs. The DC outputs from the five electrodes will be treated by five PCBs simultaneously.

The last part is a DAQ board and LabVIEW program. The DC voltage outputs from five PCBs are collected by NI DAQ board PCI-6133 and recorded using custom LabVIEW program. LabVIEW can also be used to control the micropositioner to precisely control the movement of the probe. And then the output voltage can be converted to resistance for the data processing. Figure 4.7 shows the NI BNC 2110 board which is connected to the DAQ board PCI-6133 for colleting the experimental data. Figure 4.8 illustrates the costumed LabVIEW VI block diagram for static and step function analysis, while Figure 4.9 shows the LabVIEW VI block diagram for vibration analysis.

One of the difficulties of this setup is the alignment of the probe to the device. The device is fixed on the top of a 5-axis manipulator which can be used to control the alignment along $x$, $y$, $z$, pitch and yaw directions. It needs to be mentioned that micropositioner can be used to control the alignment along $x$, $y$ and $z$ directions, but not pitch and yaw directions. At the initial position, to make sure the probe is in contact with the surface of the device without causing deflection, a precise control should be done by moving the probe down little by little or gently adjusting the 5-axis manipulator until a small change of DC voltage outputs of all the transducers or the output of the load cell can be detected from oscilloscope. Once the alignment is done, the position of the probe can be set as the home position by using the micropositioner or the software LabVIEW. By doing this, the position can be easily labeled and read during experiments.

Figure 4.7 NI BNC 2110 board for collecting experimental data.

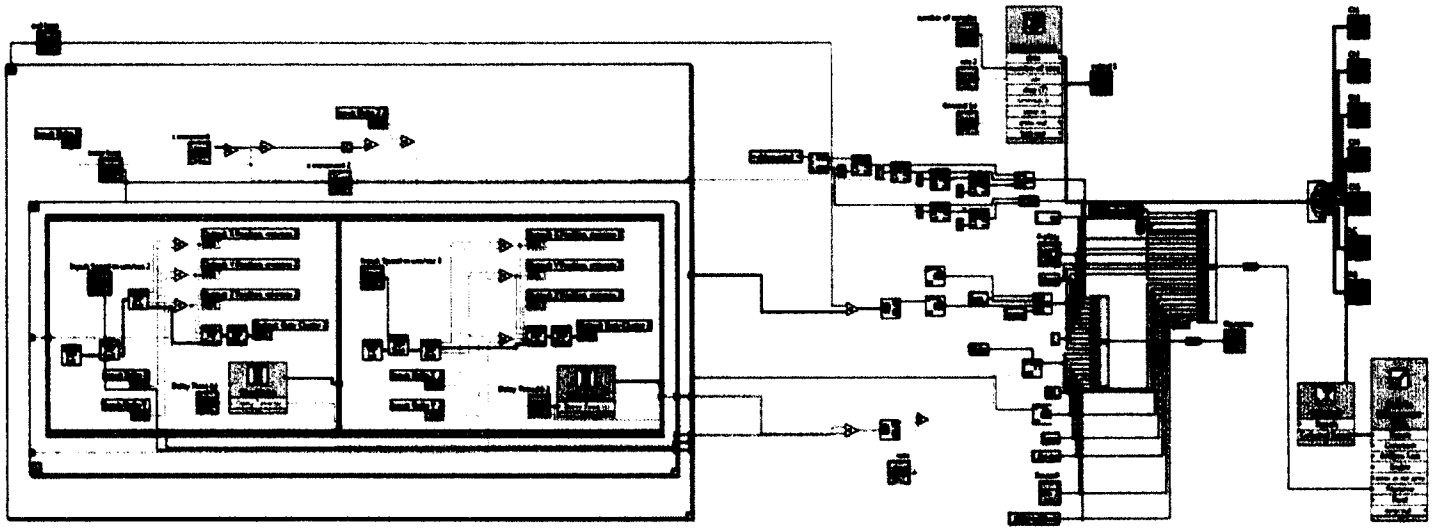

Figure 4.8 Costumed LabVIEW program for static and step function analyses.

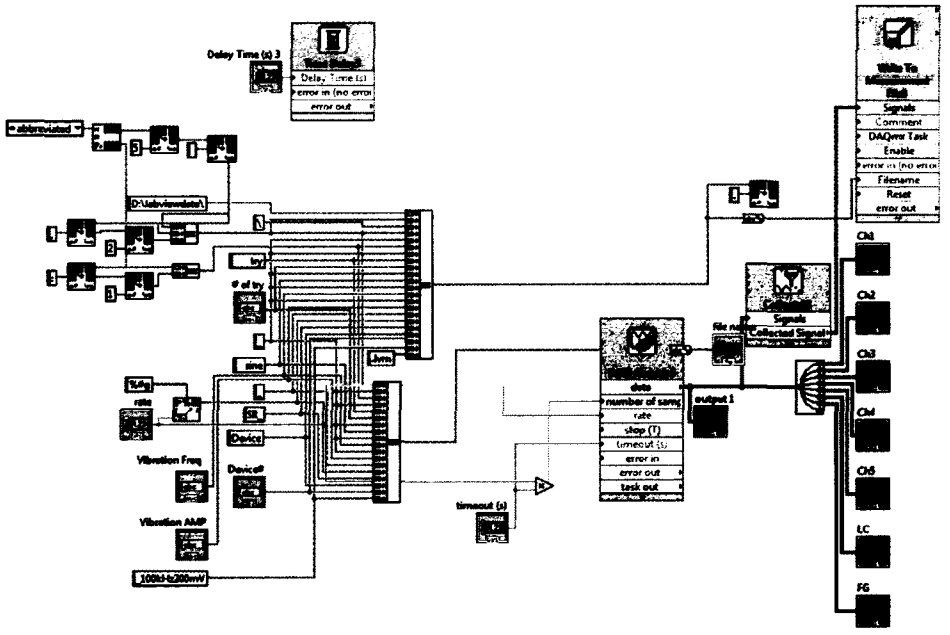

Figure 4.9 Costumed LabVIEW program for vibration analysis.

## 4.2 Electronic circuit

The electronic circuit is an important part of the whole system and it will determine the overall system performance. It is designed to detect, amplify and filter the electrical signals from the device. A high frequency AC voltage, which is used to generate the input signals, is applied to the electrodes of one side of the device, and the signals will go through the device and reach the other side of the electrodes. A custom electronic circuit

is utilized to connect to the metal pads which are connected to the electrodes, and also utilized to measure the signals.

The whole electronic circuit contains a transimpedance amplifier, a multiplier and a third-order low pass filter. First of all, an AC voltage with high frequency (100kHz) is generated by the function generator. After going through the transducers of device, the five pairs of electrodes or five transducers convert this AC voltage to a sensing AC current. This sensing AC current is stabilized and amplified by an OP-AMP(OPA656U). Here, an inverting amplifier configuration is utilized to minimize the parasitic effect on the current signal by virtual grounding the inverting input, as shown in Figure 4.10.

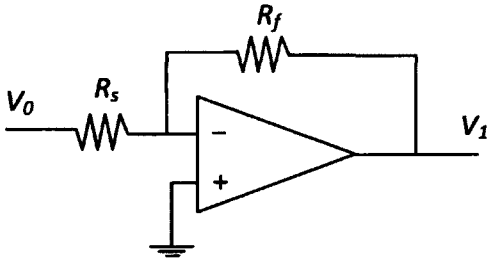


Figure 4.10 An inverting amplifier configuration

According to the Kirchhoff's voltage law, the loop equation for the input AC voltage $V_0$ and the output voltage $V_1$ of the Op Amp will be

$$V_0 = I_{in}R_s$$

$$V_1 = I_{in}R_f$$

Then the voltage gain $A$ will be

$$A = \frac{V_1}{V_0} = \frac{I_{in}R_f}{I_{in}R_s} = \frac{R_f}{R_s}$$

where $R_s$, $R_f$ are the input resistors, which are from the device and feedback resistors, respectively. It should be noticed that, because of the inverting amplifier configuration, the signal after the Op Amp will have a 180 degree phase difference. Also, by adjusting the value of feedback resistor $R_f$, the open loop gain $A$ can also be adjusted. The input AC voltage can be expressed as

$$V_0 = v_{ac} = \frac{v_{PP}}{2}\sin(\omega t)$$

where $v_{PP}$ denotes the peak-peak value of the AC voltage, and $\omega$ denotes the frequency of the AC voltage. Then the output after the Op Amp will be

$$V_1 = v_1 = \frac{v_{ac}}{R_s}R_f = Av_{ac}$$

The second part of the electronic circuit is the demodulation stage consisting of multiplier and a third-order low pass filter. To avoid the phase difference between inputs, the output $v_1$ from Op Amp will be split to two identical inputs for the multiplier AD835. Therefore, after these two identical inputs are multiplied, the output becomes

$$V_{out} = v_1^2 = A^2\left(\frac{v_{PP}}{2}sin(\omega t)\right)^2 = A^2\frac{v_{PP}^2}{8}(1 - cos(2\omega t))$$

It is very clear, after the multiplier, that the output of the voltage contains two parts: a DC voltage part $A^2v_{PP}^2/8$ and an AC voltage part. To make the output stable and easy to observe, the second AC voltage part can be eliminated by using a low pass filter and the DC output is kept and recorded accordingly.

Certainly, following the multiplier is a third-order low-pass filter to cut off the frequencies larger than 100Hz. This third-order low-pass filter is a combination of a first-order and a second-order low-pass filter. It contains two Op Amps OPA656U and a few resistors and capacitors with different value to make sure the output after the

demodulation stage will maintain the voltage gains to be 1. Here, the Op Amps, both in the first-order and second-order, use non-inverting amplifier configuration to stabilize the output. Figure 4.11(a) and (b) show the first-order and second-order non-inverting amplifier configuration, respectively.

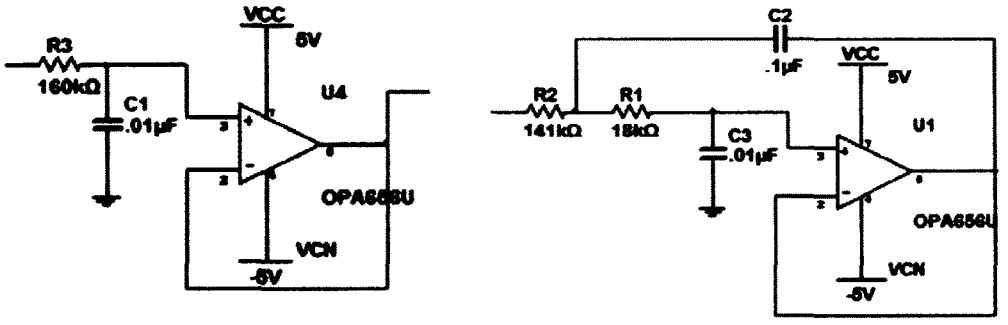


(a) (b)

Figure 4.11 The configuration of the low-pass filter (a) first-order (b) second-order.

After the filter, the AC input voltages will be converted to a DC voltage $V_{out}$. So the output after the multiplier becomes

$$V_{out} = \frac{v_{PP}^2 R_f^2}{8R_s^2} \tag{12}$$

Here, the output from the multiplier $V_{out}$ can be easily detected, and the input AC voltage $v_{PP}$ and the feedback resistor $R_f$ are known. Thus, the resistor of the device $R_s$ can be obtained from the following equation, which is derived from the previous equation.

$$R_s = \frac{v_{PP} R_f}{2\sqrt{2V_{out}}} \tag{13}$$

Accordingly, the overall voltage-to-resistance sensitivity of the circuit can be derived as:

$$S = \frac{\partial V_{out}}{\partial R_s} = -\frac{v_{PP}^2 R_f^2}{4R_s^3}$$

Therefore, in order to get a higher sensitivity of the circuit, a higher peak-peak value of the AC input voltage and a larger feedback resistance should be chosen within the operation range. But a larger peak-peak value of the AC voltage will cause a significant phenomenon called electrolysis [26], which will deteriorate the metal electrodes and affect the function of the device. Therefore, the AC voltage amplitude should not be too high to avoid the occurrence of electrolysis. Figure 4.12 and Figure 4.13 show the schematic view of a custom electronic circuit and the configuration of circuit respectively.

The configuration of the whole circuit is then implemented on five identical PCBs as shown in Figure 4.14 for collecting the resistance changes of the five transducers simultaneously. Five PCBs allow accurate measurements for separate transducers, and also give us a concept whether there are cross-talks or not. According to this configuration, the simulated result for the time delay of this circuit is about 12.5ms. Figure 4.15 shows the simulated result for time delay of the circuit.

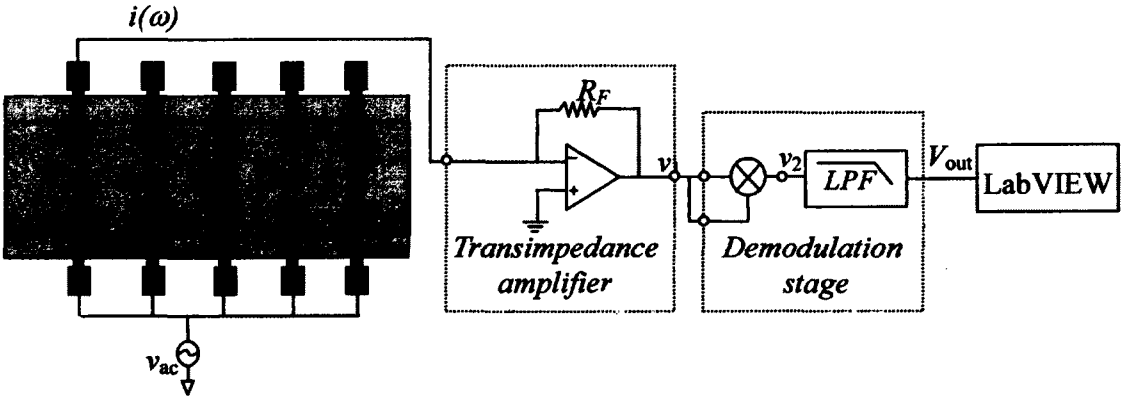


Figure 4.12 Schematic view of a custom electronic circuit.

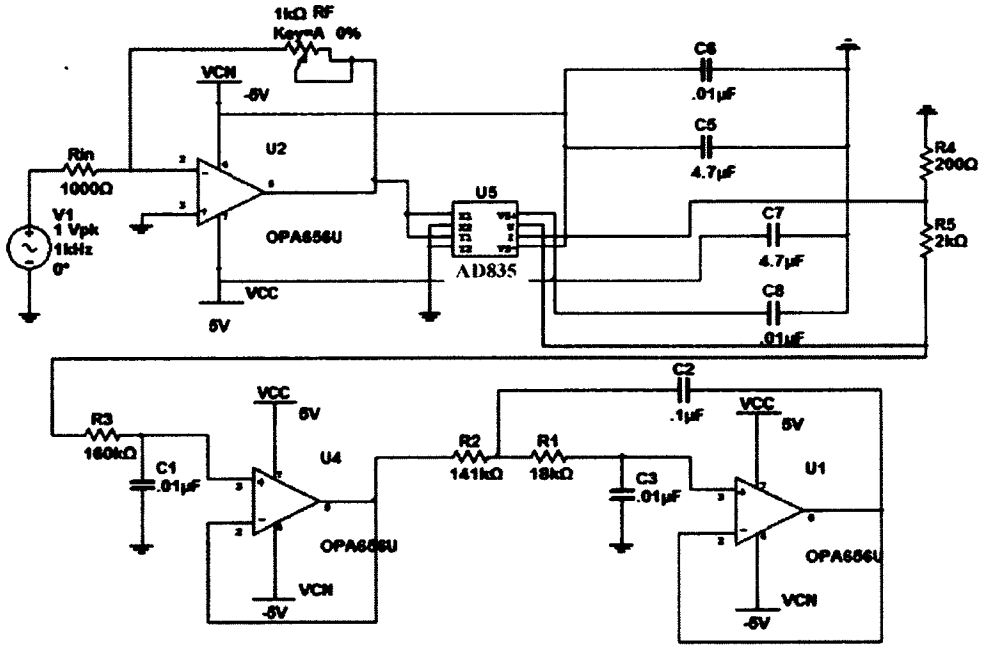


Figure 4.13 The configuration of circuit.

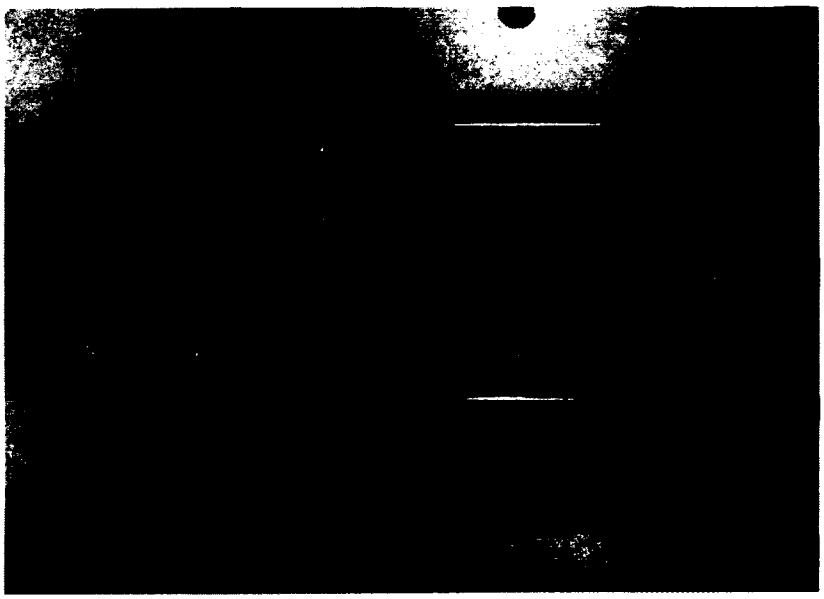

Figure 4.14 The PCB of electronic circuit.

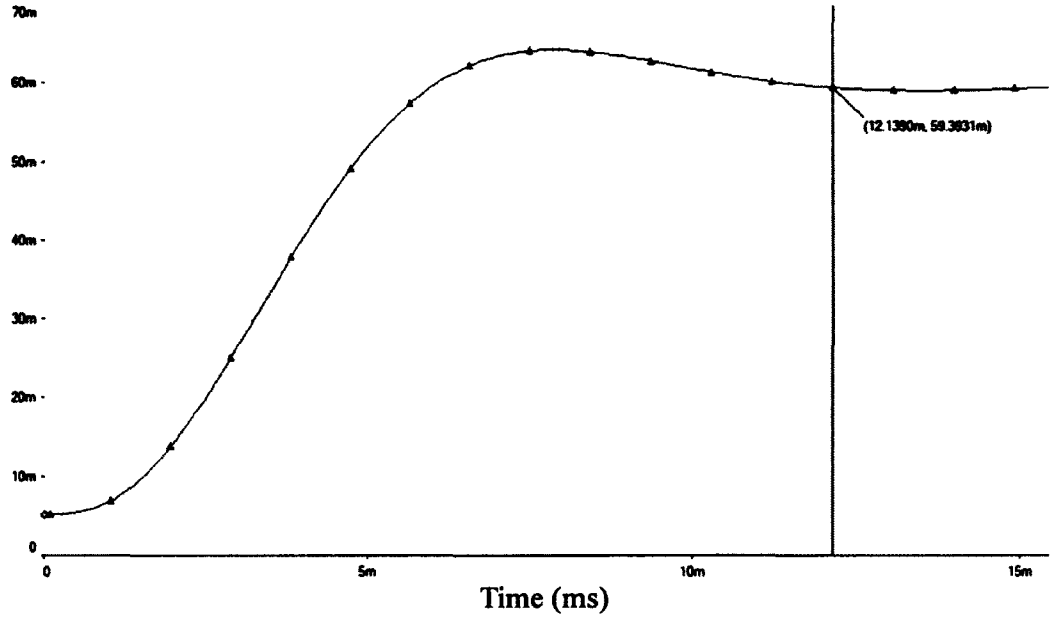


Figure 4.15 The simulated result for the time delay of the circuit.

## 4.3 Experimental method

In order to monitor the resistances of the transducers of the device, an AC voltage, $v_{ac}(\omega_0)$, is applied to the electrodes on one side of the device, while the electrodes on the other side are connected to their own interface electronics for converting an AC current signal $i(\omega_0)$, to a DC voltage output, $V_{out}$. The interface electronics for the transducers are identical and contain a transimpedance amplifier and a demodulation stage. As mentioned before, the DC voltage output is the function of applied displacement. Therefore, the relation between the DC voltage output and the AC current input from the electronics is given by Equation (12):

$$V_{out}(z_p) = \frac{v_{pp}^2 R_F^2}{8R^2(z_p)}$$

where $v_{pp}$ is the peak-to-peak value of the AC voltage signal, RF is the feedback resistance of the electronics and R is the resistance of a transducer, which is a function of the applied displacement, $z_p$, of a probe. Consequently, the resistance of a transducer can be extracted from the recorded DC voltage output by the following relation:

$$R(z_p) = \frac{v_{pp} R_F}{2\sqrt{2V_{out}(z_p)}}$$

Consequently, the resistance change as a function of the applied displacement is expressed as:

$$\Delta R(z_p) = \frac{v_{pp} R_F}{2\sqrt{2}} \left( \frac{1}{\sqrt{V_{out}(z_p)}} - \frac{1}{\sqrt{V_{out0}}} \right) \tag{14}$$

Prior to characterizing the device response to different types of inputs, the noises of the whole circuit without the input of the AC voltage, the initial values of the five transducers are measured. For different devices, the initial values are different and will be shown in the next chapter. And the discrepancy in the initial resistance among the transducers is believed to be caused by the variations in fabrication tolerance and channel alignment. Since it is the resistance change of a transducer that captures the microstructure deflection above it, this discrepancy is not expected to affect the functionality of the device. The values of the operation parameters for characterizing the device performance are summarized in Table 4.1.

Table 4.1 Operation parameters for performance characterization of the PDMS-based microfluidic device

| | Device | Symbol |
|---|---|---|
| Peak-peak value of the AC voltage | 200mV | $v_{PP}$ |
| Frequency of the AC voltage | 100kHz | $\omega/2\pi$ |
| Feedback resistance | 25kΩ | $R_F$ |

There will be three different responses to characterizing the device: static response, step response and dynamic or sinusoidal response. To characterize the static response of the devices, the probe is mounted on the micropositioner and is brought down from 0μm to a certain displacement at an increment of 10μm. The readout of the load cell and the voltage outputs of the device are recorded after a steady state is reached from each displacement increment. To characterize the device response to step inputs, the probe mounted on the micropositioner is brought down by different final displacements at a high speed, the readout of the load cell and the voltage outputs of the device are recorded at a sampling rate of 5kHz. To characterize the device response to sinusoidal inputs, the probe is mounted on the shaker and exerts a sinusoidal vibration signal on the device. The frequency and the amplitude of the vibration signal of the probe can be easily controlled by a function generator connected to the shaker. Even though the displacement of the shaker cannot be obtained directly, the probe displacement of sinusoidal response can be calculated by using the characterized data from static and step response.

# CHAPTER 5

# DEVICE CHARACTERIZATION

In this chapter, two devices are characterized in three different types of inputs, static, step and sinusoidal. Before the device characterization, a circular flat probe is used for feasibility study and two devices are tested using different electrolyte under static and step input to find out in which condition the device will have a better performance.

## 5.1 Feasibility study using a circular flat probe

Preliminarily, a circular flat probe is customized to meet the requirement of the feasibility study. As shown in Figure 5.1, this probe has a diameter of 4mm, and it can be directly fixed to the micropositioner or a shaker.

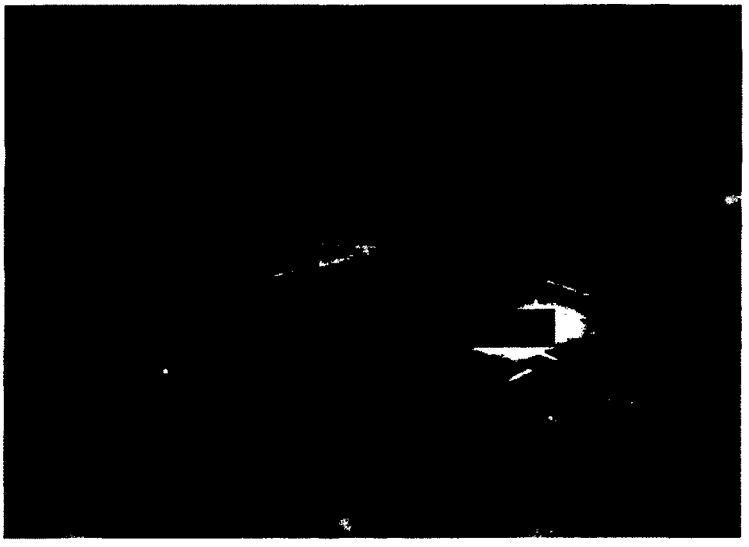

Figure 5.1 A picture of a circular flat probe.

Two devices (device #1 and device #2) are tested using different electrolytes for feasibility study. Devices firstly are used to measure the static response, and then several loops of step function response are done to mimic a low frequency dynamic response. Figure 5.2 shows that two fabricated devices are tested using different electrolyte and also the locations of the probe are different. The key parameters used for testing the two devices are summarized in Table 5.1.

The first device is filled with electrolyte 0.1M NaCl and a circular probe is located at the middle of the 3rd and 4th transducers, as shown in Figure 5.2 (a). The second device is filled with 1-Ethyl-3-methylimidazolium dicyanamide electrolyte (EMIDCA H26901-06, Alfa Aesar) and the circular probe is located at the top of the 3rd transducer, as shown in Figure 5.2 (b). The dimension of these two devices is identical with a thickness around 2mm.


(a) Device #1 with a circular probe located at the middle of the 3rd and 4th transducers

(b) Device #2 with a circular probe located at the top of the 3rd transducer

Figure 5.2 The location of the probe in different devices.

Table 5.1 The key parameters used for testing device #1 and device #2

| | Symbol | Device 1 | Device 2 |
|---|---|---|---|
| Peak-peak value of AC voltage (mV) | $V_{PP}$ | 400 | 250 |
| Frequency of the AC voltage (kHz) | $\omega/2\pi$ | 100 | 100 |
| Feedback resistance (kΩ) | $R_F$ | 35 | 25 |

### 5.1.1 Static response

Device #1 is the one with 0.1M NaCl electrolyte using circular flat probe as shown in Figure 5.2 (a). This circular flat probe aligned at the middle of the 3rd and 4$^{th}$ transducers. From 2$^{nd}$ to 5$^{th}$, four transducers are connected to the PCBs, and the outputs from the four PCBs are collected by using a custom LabVIEW program. During this time, transducer #1 is excluded. Similar to the setup shown in Figure 4.3, LabVIEW program controls the movement of micropositioner in micro scale, and the circular flat probe is completely fixed to the micropositioner which can be controlled either by Rotary Optical Encoder (ROE) of the micropositioner or by LabVIEW program. A custom Matlab filter program is utilized to filter the noise from the four outputs which is collected by LabVIEW program and these voltage outputs are filtered with a cutoff frequency of 1Hz. The voltage outputs are converted to the resistance values, and the results are plotted in Figure 5.3(a) which is the resistance values against the probe displacement. From this figure, it is noticed that the initial resistance is in the range of 15kΩ ~ 19kΩ, and the resistance values varies with the change of the probe displacement. The four outputs of the device are further converted to resistance changes ΔR and are plotted in Figure 5.3(b). As shown in this figure, because of the ability of

measuring distributed load, the resistance changes of the four transducers are different due to the location and displacement of the probe. The third and fourth transducers experience larger resistance changes since the probe is located at the middle of the 3rd and 4th transducers, and the third one is larger than the fourth one. This proves that the probe is leaned to 3rd since the probe is visually aligned and not aligned perfectly at the middle. The second and fifth transducers don't experience much resistance changes since they are far away from the probe, and the fifth one shows even smaller resistance change again proving that the probe is leaned to the third one. From these figures, it is very clear that the resistance changes vary with the amplitude of the probe displacement.

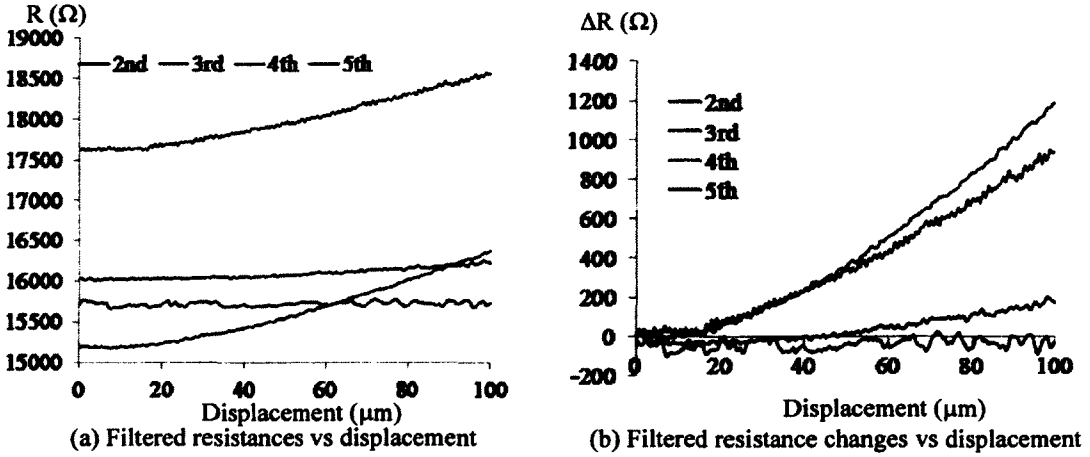


(a) Filtered resistances vs displacement

(b) Filtered resistance changes vs displacement

Figure 5.3 Static performance of device #1.

Device #2 is the one with 1-Ethyl-3-methylimidazolium dicyanamide (EMIDCA) electrolyte using circular flat probe as shown in Figure 5.2(b). This circular probe is aligned in the middle of the microchannel, which is on the top of the 3rd transducers. Four transducers, which are the first four transducers, are connected to the PCBs, and the fifth transducer is connected to a breadboard circuit. Again, LabVIEW program controls the

micropositioner precisely, and collects the outputs data from the four PCBs and 1 breadboard circuit. As stated before, Matlab filter program is used to remove the noise and five voltage outputs from five transducers are collected using LabVIEW program. These voltage outputs are converted to resistance values and are plotted versus probe displacement in Figure 5.4(a). This time, because of the high electrical conductivity of the new electrolyte, EMIDCA, a lower AC voltage amplitude and a lower feedback resistance are used as shown in Table 5.1. The initial values of the resistances, which are around the range of 3800Ω ~ 4050Ω, are much smaller compared with device #1. As shown in Figure 5.4(b), the resistance changes versus probe displacement is plotted and demonstrated that the 3rd transducer experiences the largest resistance change due to the probe is located on the top of the 3rd transducer. Comparing to the value of the 2nd and the 4th transducers, we can easily conclude that the probe is not aligned perfectly in the middle of the device but more leaned toward the 4th transducer's side.

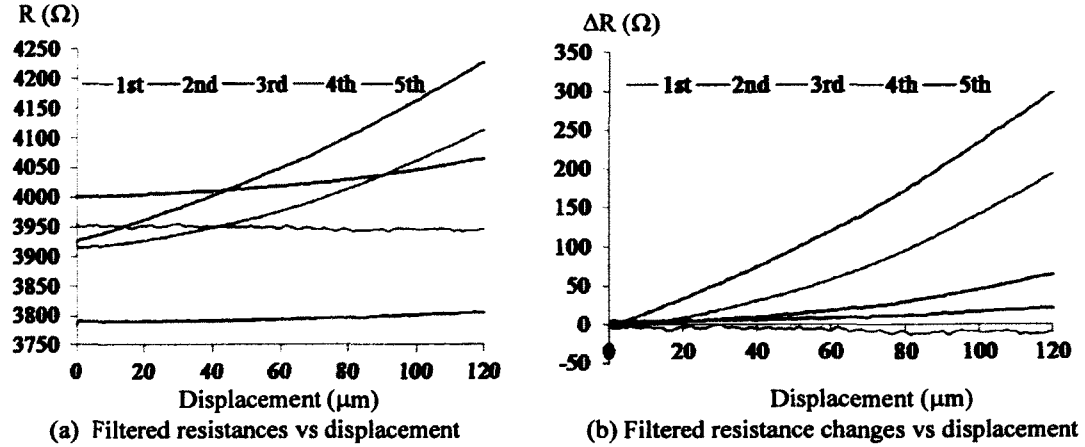


(a) Filtered resistances vs displacement

(b) Filtered resistance changes vs displacement

Figure 5.4 Static performance of device #2.

### 5.1.2 dynamic response

The same setup is utilized for step response. A predefined displacement pattern is generated by micropositioner and controlled by LabVIEW. First, the probe moves downward from the initial position to 100μm in a defined speed of 100μm/s. After it reaches the final displacement, it stays there for 6 seconds. Then the probe moves up and goes back to the initial position with the same speed. As same as before, there is also a 6-sencond-stay. This cycle repeats several times in order to mimic a low frequency dynamic response. The circle probe generates distributed dynamic loads on the top of microstructure between the position of 3$^{rd}$ and 4$^{th}$ transducers and then the loads are converted to voltage outputs through the four transducers. Figure 5.5 illustrates the filtered resistance changes of the four transducers versus the dynamic displacement pattern of the probe. It is very clear that the four transducers demonstrated in the same pattern as the predefined displacement pattern. These changes also reflect the various distributed loads in different position. As stated before, the probe is located on the top of the 3$^{rd}$ and the 4$^{th}$ transducers and leans a little bit towards the 3$^{rd}$, so the resistance changes of four transducers show the same trends as the static performance: the 3$^{rd}$ transducer has the largest change of resistance value.

Another critical parameter in the dynamic performance is the time delay. Since the filter program may introduce extra retard, the unfiltered data is used to obtain the time delay. Figure 5.6 shows that the time delay of device #1 is less than 200ms. This time delay includes electronic time constant 12.5ms, the response time from the LabVIEW program to controlling the probe, and the real time delay from device itself. Therefore, the time delay from the device itself should be smaller than 200ms.

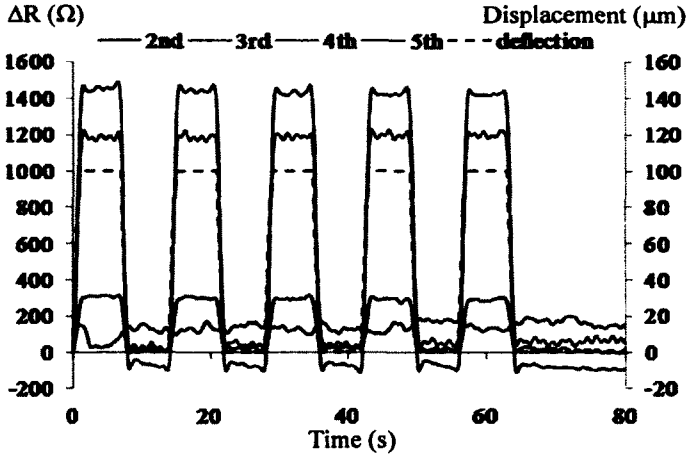


Figure 5.5 Step response of device #1: filtered resistances against displacement.

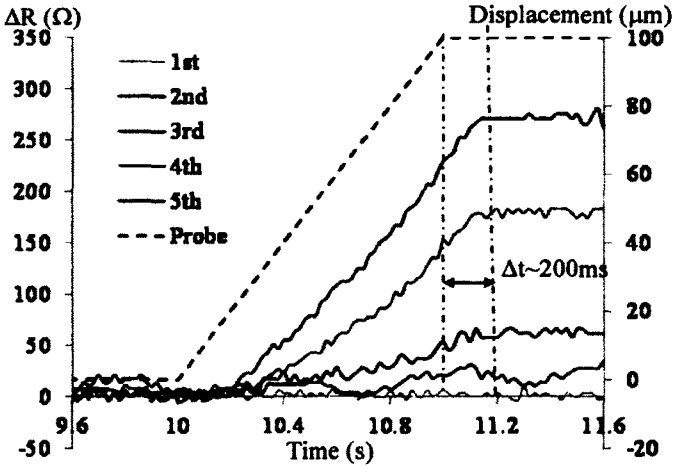


Figure 5.6 Step response of device #1: time delay of 200ms.

The step response of device #2 is also achieved by using a predefined displacement pattern which is generated by micropositioner. The patterns are almost the same as device #1 but this time the travel distance varies and the stay time is shorter, 4 seconds instead of 6 seconds in device #1. The travel distance, or the deflection of the microstructure is predefined as 100μm and 120μm, and the speed of probe also varies with the travel

distance, 100μm/s and 120μm/s respectively. The circle probe moves down 100μm or 120μm in one second and after reaching the predefined position, the probe stays for 4s. The probe then goes up to a corresponding distance, reaches the initial position and stays there for 4s. This cycle repeats several times and plotted relation between resistance changes and time for 100μm and 120μm is shown in Figure 5.7 and Figure 5.8 respectively.

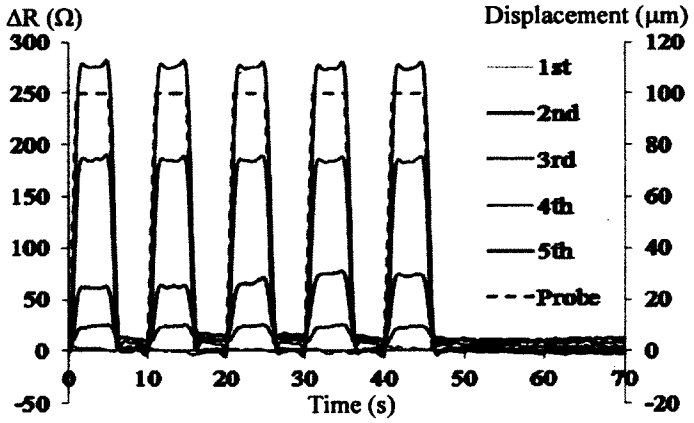


Figure 5.7 Step response of device #2: ΔR vs time at a displacement of 100μm.

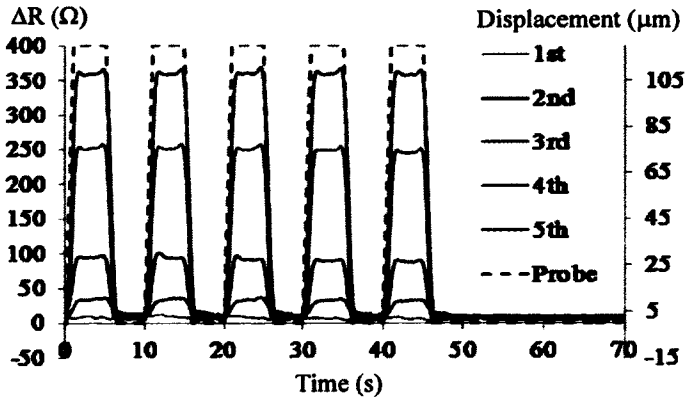


Figure 5.8 Step response of device #2: ΔR vs time at a displacement of 120μm.

To verify that the device can detect the distributed dynamic load, we changed the location of the probe from the top of the 3rd transducer to 2nd and 4th. Figure 5.9 clearly demonstrates that the device responses the displacement pattern differently. When the probe located on the top of the 2nd transducer, as shown in Figure 5.9(a), the resistance change of transducer #2 is the largest one and since the probe is a little bit leaned to 3rd transducer, the resistance change of transducer #3 is a little bit larger than the one of transducer #1. And because transducers #4 and #5 keep distance from the probe, the values of resistances did not change much. Similarly, as shown in Figure 5.9 (b), when the probe is located on the top of the transducer #4, the resistance change of transducer #4 is the largest one and then the second largest one is #5 since the probe is visually aligned and closer to transducer #5.

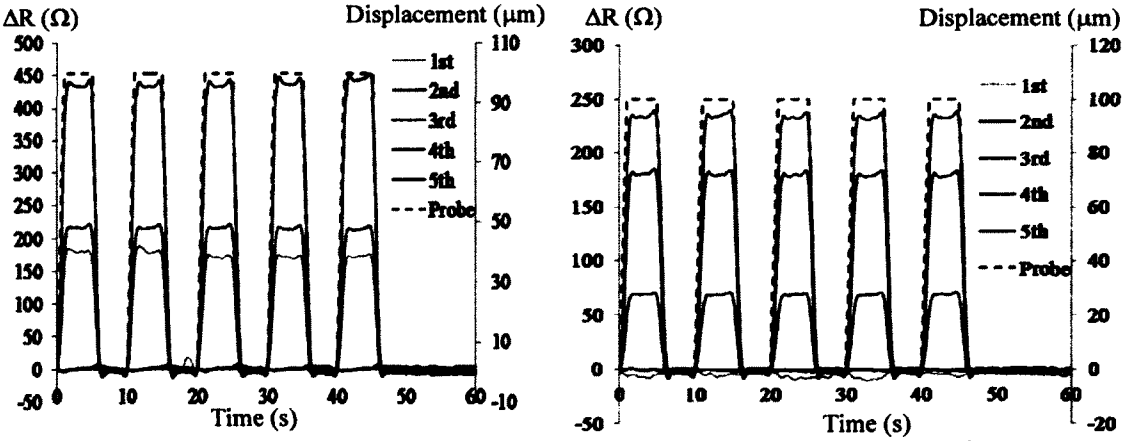


(a) Probe located on the top of 2nd transducer

(b) Probe located on the top of 4th transducer

Figure 5.9 Resistance changes with the different location of probe.

Meanwhile, to clarify the time constant, or the time delay, a predefined 5μm-step displacement pattern is applied on the top of the 3rd transducer of the device #2, the exact

location as the static performance. This pattern controls the probe moving downward 5μm each time, and then stays there for 5 seconds. After the stay, the probe continues moving downward 5μm and repeats the cycle until reaching the final displacement 100μm. The resistance changes of the transducers are shown in Figure 5.10 (a) along with the probe displacement pattern, and the time constant is around 200μm as shown in Figure 5.10(b) when we zoomed in one of the steps.

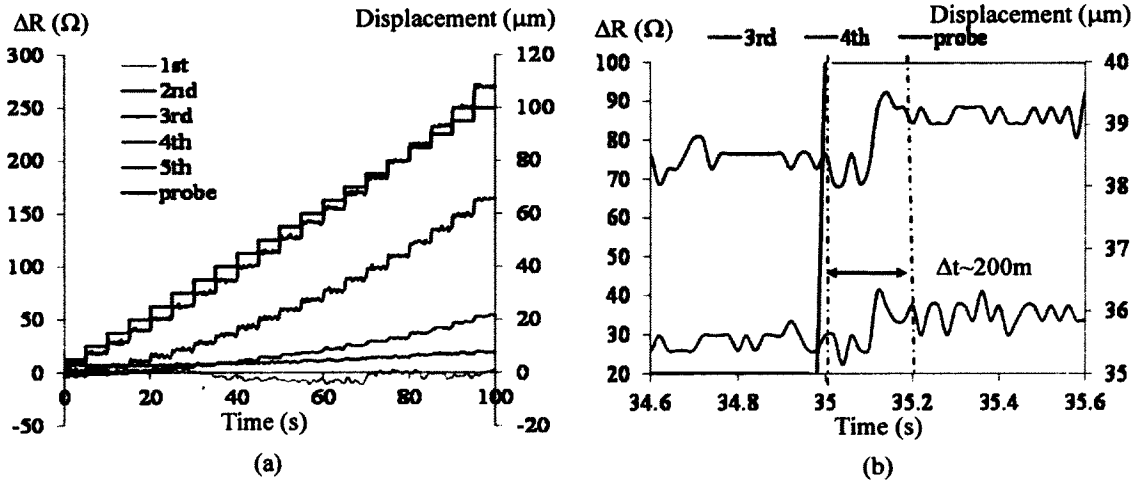


Figure 5.10(a) Filtered resistance changes with step-displacement pattern and (b) time delay of Device #2 in one of the steps.

### 5.1.3 Issues identification

According to the feasibility study, a few issues are addressed: the first one is the problem of electrolyte. As shown in Figure 5.11, the electrodes got slowly deteriorated and finally some metal deposition layers were totally destroyed when 0.1M NaCl electrolyte was used. This phenomenon of electrolysis gets more distinct if a higher AC

input voltage or longer operation time was involved. Also, because of the problem of evaporation, the solution concentration of 0.1M NaCl electrolyte increased with time, making the initial value of the device slowly change with time. But for EMIDCA electrolyte, because of its free of evaporation, it is always stable and will not deteriorate the electrodes. Thus, EMIDCA becomes a better choice for filling as an electrolyte. From Figure 5.11, some bubbles also can be seen between electrodes. Therefore, it is worth to mention that we need to pay attention to the filling process to make sure there are no air bubbles in the microchannel.

Figure 5.11 Phenomena of electrolysis in an electrolyte embedded device.

The second issue is alignment problems. From the section 5.1, it is very clear that the circular probe tilted to one side of the device #1 and #2. There are two associated alignment issues in these two devices. The first alignment issue is the alignment of the electrode pairs with the polymer microstructure during bonding in fabrication process. Actually, the bonding is done by visually alignment under a microscope without alignment marks, so the initial resistances of transducers are not same or symmetric. This

alignment cannot be changed after the fabrication. To solve this problem, a few alignment marks are needed during the mask drawing process. The second alignment issue is the alignment between the probe and the device in the testing process. Because of the absence of manipulator, it is very difficult to align the probe with the device. Therefore, the alignment problem shows up every time. By introducing a 5-axis manipulator, this problem is alleviated a lot. The alignment can be done by adjusting the manipulator in 5 directions: x, y, z, yaw and pitch, or adjusting the micropositioner in x, y and z direction.

Another issue is the use of probe. Devices #1 and #2 use a circular flat probe as shown in Figure 5.1. This probe worked well but had some limitations. For instance, it cannot be used for the whole length of the microchannel nor can it be assembled with load cell. To solve this problem, a custom probe with probe holder is made as shown in Figure 4.6. This custom probe can be held directly to the probe holder #1 or probe holder #2 with a load cell. Also, the half cylinder shape faced against the device allows the contact along the length of the microchannel.

The last issue is the lack of measurement of load. Because the loads could not be measured during the experiments, the relationship between the force and the displacement was unclear even a simulation could be introduced to mimic the relation. To solve this problem, a piezo type, commercial load cell Kistler-9712B5 is introduced here between the probe and probe holder to make it possible to measure the loads during the experiment.

From the previous experimental results, device-to-device variation from the identical device design is expected from unavoidable fabrication variations. Since this

type of device is aimed for disposable use, each individual device can be characterized prior to use and discarded after use. Thus, performance characterization of the $F_d$-$z_p$ relation and the $\Delta R$-$z_p$ relation is necessary for each individual device. Meanwhile, such performance characterization of a device can directly serve as a control experiment before proceeding to measure a specimen using the device.

Through the feasibility study of the device #1 and #2, the experimental setup is updated and modified to meet the experimental requirements.

## 5.2 Performance characterization using a cylinder probe

### 5.2.1 Static response

Two devices, device #3 and device #4, are used to do the static response analysis, step function and dynamic analyses. These two devices have the same dimension and configuration, and the only difference between them is that they are fabricated at different time. Consider the variation of the fabrication, these two devices are expected have little discrepancies.

The electrolyte, 1-Ethyl-3-methylimidazolium dicyanamide or EMIDCA, is used for these two devices due to its very low viscosity, free of evaporation, high fluidity, good conductivity and perfect stability. These can be seen from the comparison of the device #1 and #2 in the previous section.

Moreover, to generate a distributed load along the length of the microchannel, a long, high-stiffness metal probe with a half-cylinder shape against the device is used to mimic the uniform distributed load. This original probe is 15mm long with a needle end.

After the use on the device #3, a problem has been found for this long probe. That is: under a larger applied displacement, the probe will squeeze electrolyte in the reservoirs and affect the performance because of the long length. Later on, on device #4, this probe has been cut to only 11mm long, which is shown in Figure 4.5 and Figure 4.6. The dimension is shown in Table 2.1. Figure 5.12(a) shows that long probe applied to device 3 and (b) shows the short one which is applied to device #4.


(a) A 15mm probe applied to device 3 (b) A 11mm probe applied to device 4

Figure 5.12 Probes located at the top of the whole microchannel.

Besides, for measuring the force during the experiment, a load cell is added to the setup. For this purpose, a new probe stack is designed and fabricated. This new stack has two probe holders, a load cell and a half-cylinder shape probe, as shown in Figure 4.5: probe holder #1 is supposed to fix the whole stack to the micropositioner or vibration shaker; and probe holder #2 is to fix the load cell and the half-cylinder shape probe, while the load cell is fixed between the probe holder #1 and holder #2.

For the setup, one side of the electrodes of the device is connected to the input side of a bonding PCB, which is connected to the function generator to generate the input AC

signal. Here, the frequency and the amplitude of the input AC signal are kept in 100kHz and 200mV respectively as shown in Table 4.1. When micropositioner controls the displacement of the probe, the microstructure of the polymer-based device will be deflected to cause the resistance change of transducers. This change will be captured by five pairs of electrodes. On the other hand, the output side of the electrodes is connected to the output side of the bonding PCB and connected to five circuit PCBs to amplify, demodulate and filter the output signals. Finally, these signals will be sent to a costumed LabVIEW program to collect the data and then these data will be processed by Matlab and Excel.

Two different approaches are used to measure static response. One is a predefined displacement downward to push the device in a speed of 3000μm/s with a 10μm increment every time and then stay there for three seconds. This predefined displacement looks like going downstairs as shown in pattern #2 in Figure 5.13. Because the load cell can only measure the dynamic force, for each "stair", the load can be measured by calculating the differences of readouts of load cell. But if the overall load is needed after a large displacement applied, the load can only be obtained by adding the each value together, and this approach will introduce accumulated calculation errors.

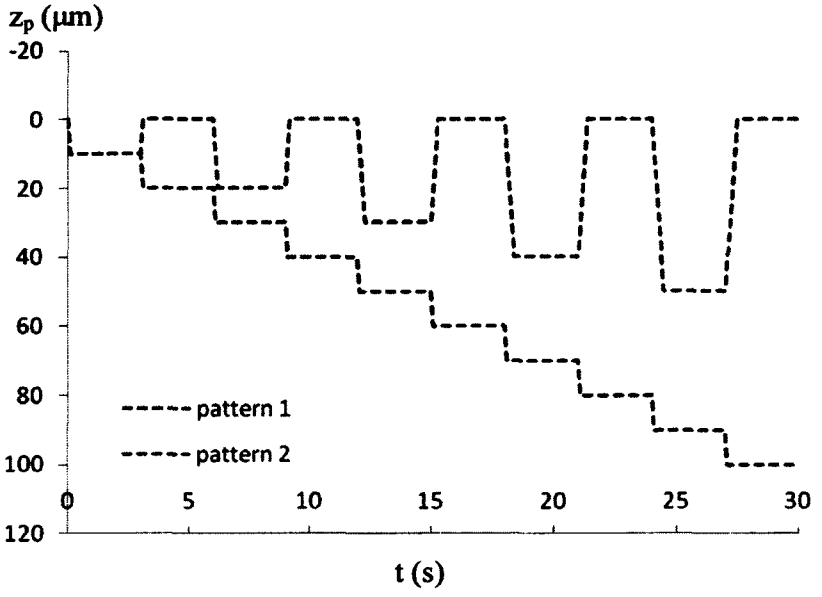


Figure 5.13 Two predefined patterns for static response.

Another approach is pushing down the device in a certain displacement and going back to the initial position, and next time going down to a new displacement with a 10μm increment and return to the initial position as the pattern #1shown in Figure 5.13. This pattern can be repeated with a 10μm increment until the designed displacement. By using this approach, the load measurement from load cell can be obtained more accurately since it will not introduce the accumulated calculation errors.

**a) Static response of device #3**

By using predefined displacement pattern #1, static response for device #3 can be obtained. Figure 5.14 to Figure 5.18 show the static response using this approach. Figure 5.14 plots the output voltages from five transducers against the displacement of

microstructure, and Figure 5.15 demonstrates the relation between resistance and the displacements, while Figure 5.16 gives the nonlinear relation between resistance change and applied loads, which are obtained from the readout of the load cell. From the figures, we can clearly see the transducers' resistance values changed with the applied displacement, and the resistance values of transducer #4 and #5 got to the maximum when the displacement reached around 460μm. Two reasons will cause this; one is the variation of the fabrication, and another one is the alignment problem because the probe tilted to transducer #5.

The maximum applied displacement and the overall load of the device are about 460μm and 1N, respectively, in the sense that the outputs of the 4th and the 5th transducers saturate beyond these values. Although the microchannel thickness is only 80μm, an applied displacement as high as 460μm can still cause a resistance change in the transducers, as the 2 mm thick PDMS microstructure top absorbs a certain amount of the load from the probe by generating deformation. Therefore, the resistances of the transducers of a device keep varying with the probe displacement.

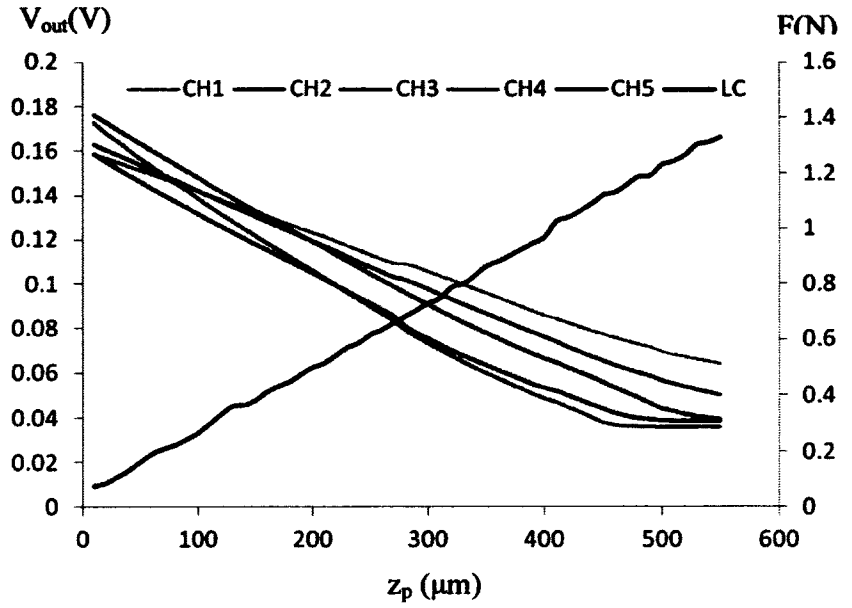


Figure 5.14 Recorded voltage outputs vs displacement of device #3.

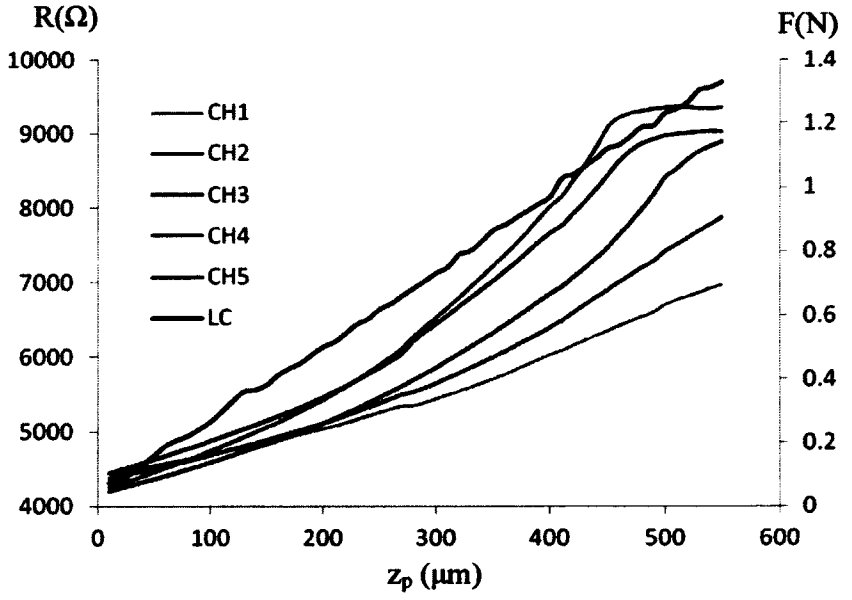


Figure 5.15 Resistance vs displacement of device #3.

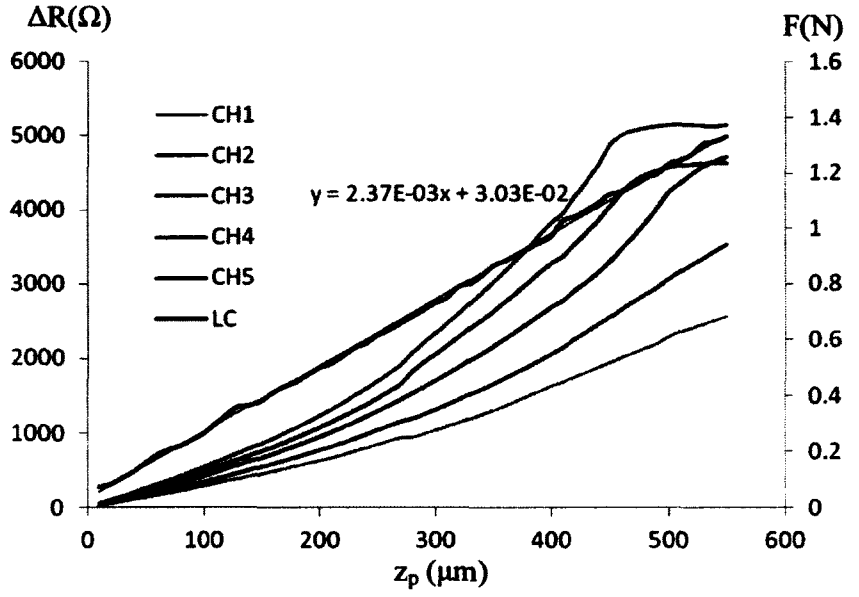


Figure 5.16 Resistance changes vs displacement of device #3.

It should be noticed that in Figure 5.16, load cell measurement is also shown in the black line. According to the Figure 5.16, the linear relation between the load and displacement is obtained by using curve fitting in Excel to find out the overall stiffness of the microstructure, and then this linear equation is used to convert the displacement values to load values. Figure 5.17 shows that the resistance changes versus the load values based upon the curve fitting equation. Also, for calculating the resistance change, the initial values of the resistances and the noises of the PCB boards have been recorded as shown in

Table 5.2. This table also shows the overall stiffness of the microstructure based upon the curve fitting. Since it is a curve fitting equation, unavoidably, small variances or

errors will be introduced. Another error is from the inaccuracy of the load cell measurement. Because the outputs of the five transducers are all converted to force values based upon the load cell measurement, small variance of the load cell measurement will affect the values of the transducers.

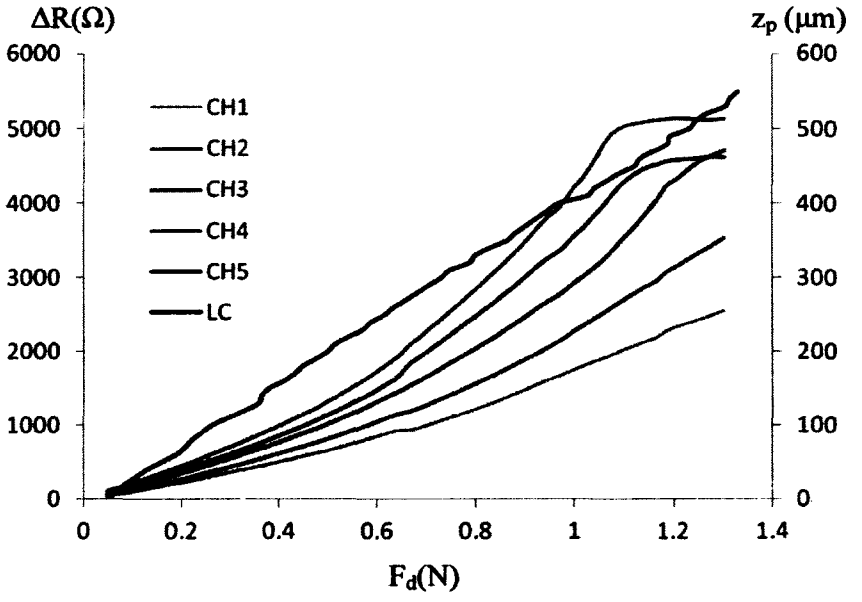


Figure 5.17 Device #3: Resistance changes versus force that measured from load cell.

Table 5.2 Initial resistance values and overall stiffness of device #3

| Transducer | 1st | 2nd | 3rd | 4th | 5th |
|---|---|---|---|---|---|
| Initial resistance, $R_{d0}(\Omega)$ | 4414 | 4349 | 4170 | 4207 | 4393 |
| PCB noise (V) | 0.0345 | 0.0326 | 0.0390 | 0.0337 | 0.0379 |
| Overall stiffness, $K_d(mN/\mu m)$ | 2.37 | | | | |

This time, since all the transducers experience a distributed load from one long probe, all the transducers have same trend of resistance changes but the 1st transducers

experience a relatively smaller resistance change compared to the 4th and the 5th. So we can conclude that this device can measure distributed load along microchannel length, also we can tell that this probe is a little bit leaning to 5th.

For better understanding of relation of resistance change and the applied displacement of the device, Equation (7) can be rewritten as

$$\frac{1}{\Delta R_d/R_{d0}+1} = 1 - \frac{\eta}{h_E}\cdot z_p \tag{15}$$

Here, it is clear that $1/(\Delta R_d/R_{d0}+1)$ is solely a function of the applied displacement of the device. Figure 5.18 illustrates this relation. Also from this figure, a transducer dependant parameter $\eta$ can be found if we assume the relation is linear. Definitely, since the transducers reached the limitation when the applied displacement is beyond 460μm, curve fitting has been done only up to 460μm. Table 5.3 shows the linear relation and 2nd degree polynomial relation of $1/(\Delta R_d/R_{d0}+1)$ ratio and applied displacement.

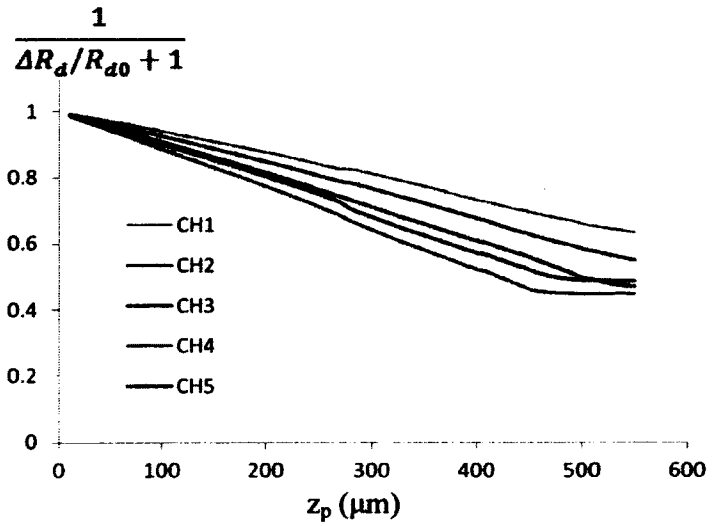


Figure 5.18 Relation of the resistance change ratio $1/(\Delta R_d/R_{d0}+1)$ versus the applied displacement of the device #3

Table 5.3 Linear and second degree polynomial curve fitting of transducers

| Transducer No. | Linear | 2nd degree polynomial |
|---|---|---|
| 1st | $-6.80 \times 10^{-4}z + 1.009$ | $-2 \times 10^{-7}z^2 - 0.0006z + 0.9994$ |
| 2nd | $-8.24 \times 10^{-4} + 1.010$ | $-3 \times 10^{-7}z^2 - 0.0007z + 0.9993$ |
| 3rd | $-9.90 \times 10^{-4} + 1.007$ | $-2 \times 10^{-7}z^2 - 0.0009z + 1.0003$ |
| 4th | $-1.20 \times 10^{-3} + 1.006$ | $-2 \times 10^{-7}z^2 - 0.0011z + 0.9995$ |
| 5th | $-1.08 \times 10^{-3} + 1.010$ | $-3 \times 10^{-7}z^2 - 0.001z + 0.9998$ |

Then, because the 3rd transducer is located at the device center and thus represents an approximately average performance of the device, a normalized resistance changes based upon the 3rd transducer can be given by using the resistance change amplitude of each of the transducers to divide the value of the 3rd transducer. Since ultimately it is the relative resistance change magnitude of the transducers that reveals the spatially-varying magnitude of continuous distributed loads, the relative resistance change magnitudes of the transducers are plotted in Figure 5.19(a).

By comparing the resistance changes of the transducers under the same applied displacement, the probe is tilted towards the 5th transducer. The relative resistance change magnitude also reflects a tilt misalignment between the probe and the device, but more importantly, the relative resistance change magnitude of the device is not affected by the non-zero initial applied displacement. Overall, the relative resistance change magnitude of the device is independent from the applied displacement. The sudden change in the normalized resistance changes of the transducers for the applied displacement above ~280μm is due to the fact that the 15mm-long probe has a tip toward

the 1st transducer end, as shown in the close-up picture in Figure 5.19(b), and comes across the two reservoirs. Thus, under a larger applied displacement, the probe effect of squeezing electrolyte in the reservoir toward the 5th transducer end becomes more severe. Also, this explains why the resistance change of the 5th transducer is smaller than that of the 4th transducer, although the probe is tilted toward the 5th transducer.

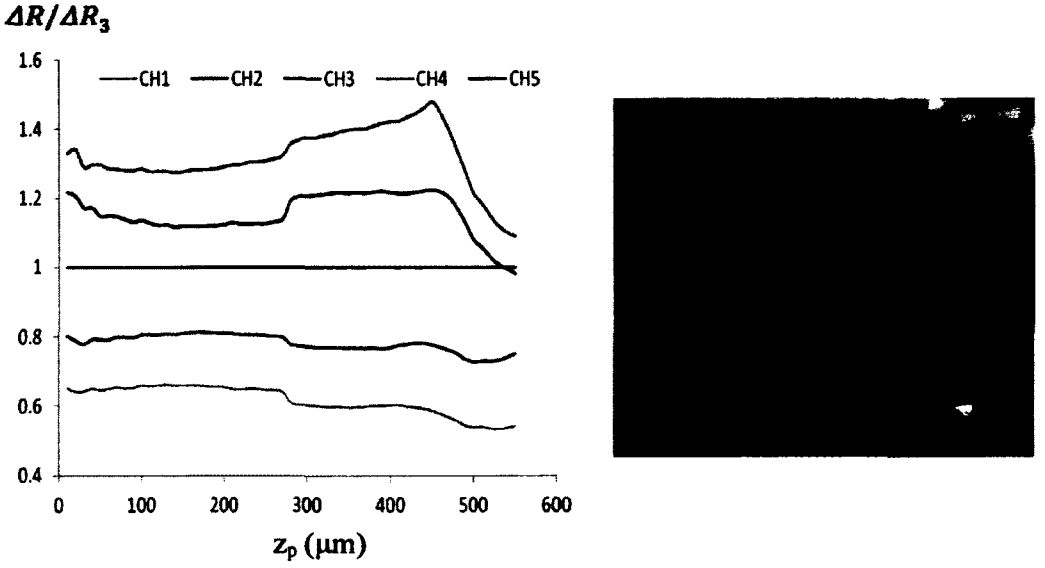


Figure 5.19 (a) the relative resistance change magnitude of the five transducers to the 3rd transducer (b) a close-up for mounting of the 15mm probe and load cell.

**b) Static response of device #4**

Device #4 has the same configuration as device #3, but was fabricated at a different time. Because of the fabrication variation, the thickness of the device #4 is a little bit different from device #3. Therefore, the performances of the devices are a little bit different. This difference is expressed in output voltages, initial resistances, resistance

changes and overall stiffness of the device. This difference also emphasized that the importance of the characterization of the device. The probe used here is the one with 11mm length, which is shown in Figure 4.5 and Figure 4.6.

Figure 5.20 to Figure 5.24 illustrate the static response for device #4. Recorded voltage output against the applied displacement is plotted in Figure 5.20. The recorded voltage outputs at different static applied displacements are then converted to resistance changes according to Eq.(12). Figure 5.21 represents the resistance of transducers as a function of the applied displacements or the $R$-$z_p$ relation. Figure 5.22 shows the resistance changes of the transducers as a function of the applied displacement ($\Delta R$-$z_p$ relation), together with the accompanying measured overall load. Additionally, the slope of the measured $\Delta R$-$z_p$ relation is the sensitivity of the device to the applied displacement.

Figure 5.22 also shows the linear relation between the overall force and the applied displacement. Therefore, overall stiffness of the device can be obtained by using the curving fitting of plotted $F$-$z_p$ relation. Table 5.4 shows the initial resistance values, PCB noises and the overall stiffness, which is obtained from the curving fitting of plotted $F$-$z_p$ relation. After curving fitting, the measured overall stiffness of the microstructure is $k_d$=3.15mN/μm. The offset (-3.4e-3N) in the $F_d$-$z_p$ relation represents an initial applied displacement of ~-1μm before the static test is conducted. That means the probe didn't contact the device yet when the test is conducted, but the overall distance between the probe and the device is just a little bit more than 1μm. The resistance change of the 3rd transducer can be represented by a 4th-degree polynomial of the applied displacement by curve fitting the ΔR-zp relation of the 3rd transducer:

$$\Delta R_3 = 6 \cdot 10^{-7} z_p^4 - 3 \cdot 10^{-4} z_p^3 + 0.0634 z_p^2 + 0.3228 z_p - 6.6015 \qquad (16)$$

where an initial resistance change of ~-6.6Ω corresponds to the initial applied displacement -8.07μm. This indicates that, in the initial position, probe and 3rd segment of the microstructure has not contacted yet, and there is a distance of 8μm between them.

Table 5.4 Initial resistance values and overall stiffness of device #4

| Transducer No. | 1st | 2nd | 3rd | 4th | 5th |
|---|---|---|---|---|---|
| Initial resistance, $R_{d0}(\Omega)$ | 4279.434 | 4242.929 | 4073.707 | 4182.688 | 4284.471 |
| PCB noise (V) | 0.0357 | 0.0376 | 0.0394 | 0.0332 | 0.0336 |
| Overall stiffness, $K_d(mN/\mu m)$ | 3.15 | | | | |

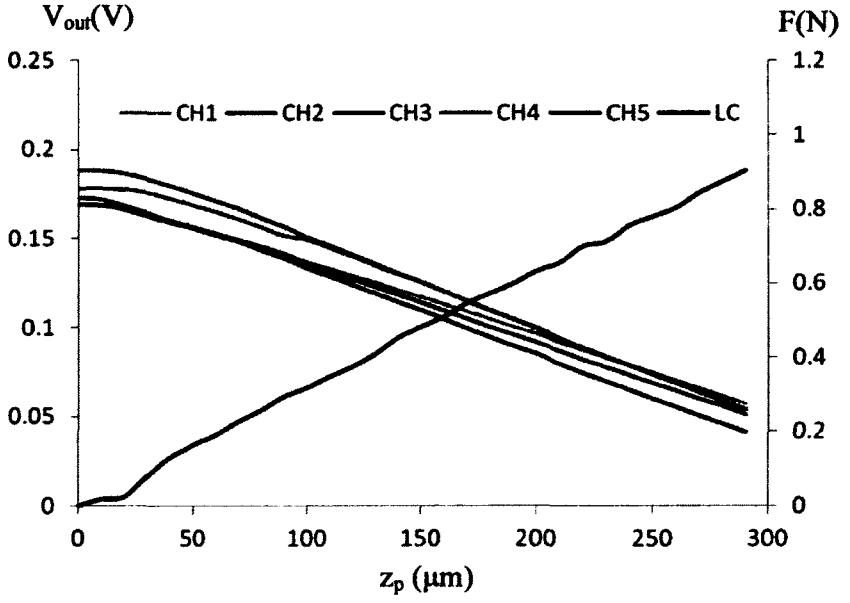


Figure 5.20 Recorded voltage outputs vs displacement of device #4.

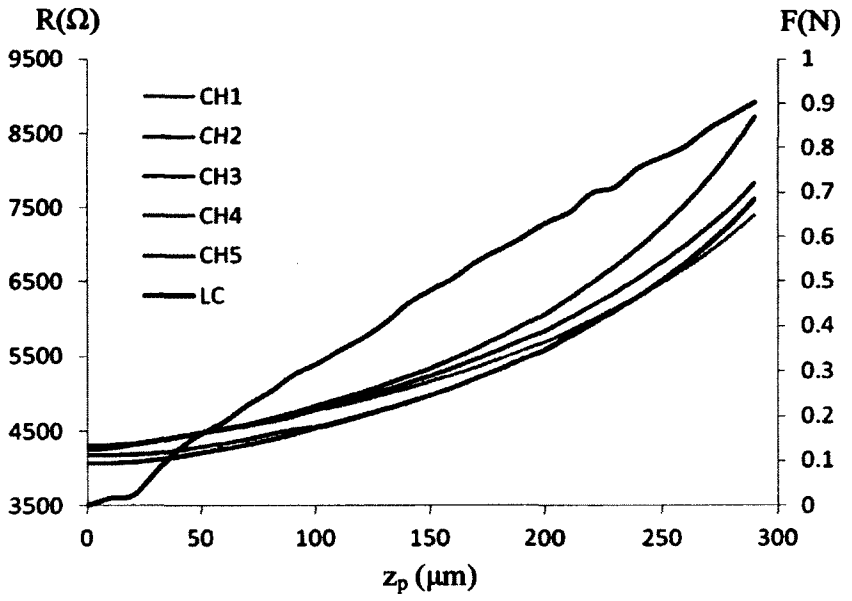


Figure 5.21 Resistance vs displacement of device #4.

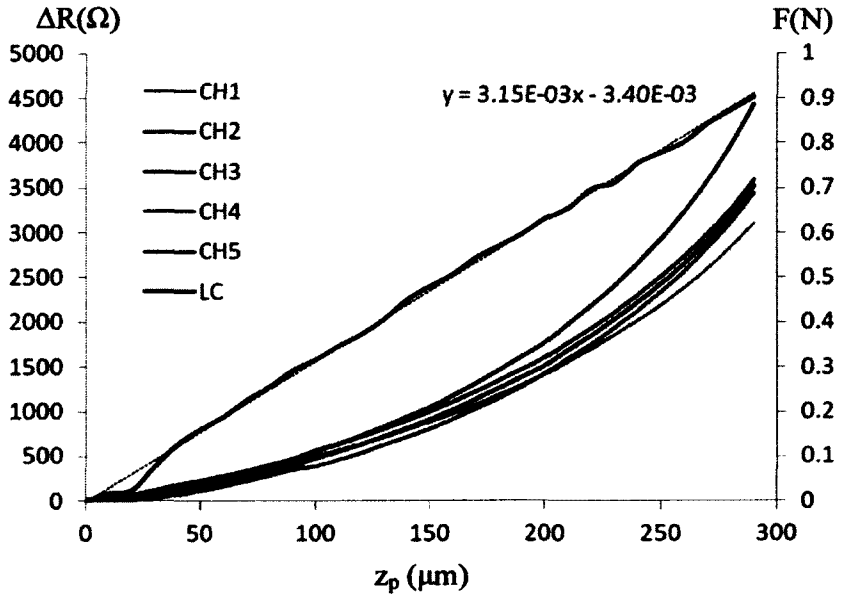


Figure 5.22 Resistance changes vs displacement of device #4.

By using the equation that is obtained from the curving fitting of the $F$-$z_p$ relation and shown in Figure 5.22, the applied displacements can be converted to applied force based upon the measured data from load cell. Figure 5.23 plots the resistance changes of the transducers as a function of the overall load ($\Delta R$-$F_d$ relation), while the slope of the measured $\Delta R$-$F_d$ relation is the sensitivity of the device to the overall load. Evidently, Figure 5.23 shows the clearly non-linear $\Delta R$-$F_d$ relation. Meanwhile, from the Eq. (15), $\Delta R$-$z_p$ relation also can be converted to a relation between the $1/(\Delta R_d/R_{d0} + 1)$ ratio and the applied displacement. This relation is shown in Figure 5.24 for a better understanding of the $\Delta R$-$z_p$ relation. It should be noticed that the flat line at the beginning indicates that the probe is not perfectly aligned. Therefore, when we do the linear curving fitting, we start from the displacement of 50μm.

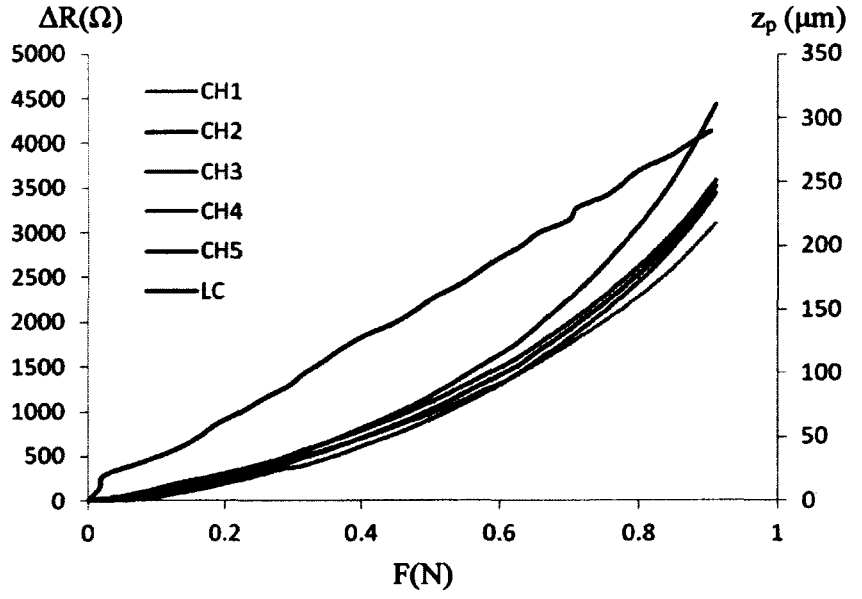


Figure 5.23 Device #4: Resistance changes versus force that measured from load cell.

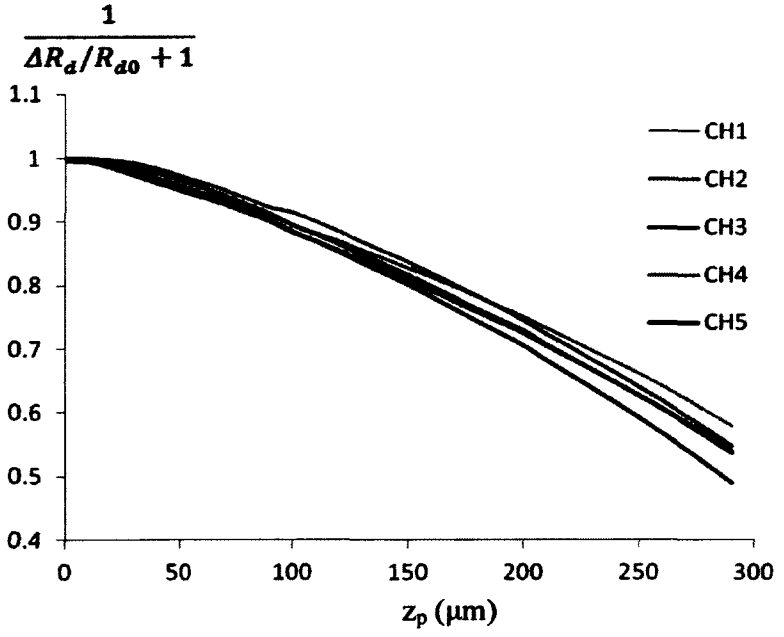


Figure 5.24 Relation of the resistance change ratio $1/(\Delta R_d/R_{d0}+1)$ versus the applied displacement of the device #4.

Table 5.5 Linear and second degree polynomial curve fitting of transducers of device #4

| Transducer No. | Linear | 2nd degree polynomial |
|---|---|---|
| 1st | $-0.0016z+1.0526$ | $-2\times10^{-6}z^2-0.0008z+1.0006$ |
| 2nd | $-0.0017z+1.0541$ | $-2\times10^{-6}z^2-0.001z+1.0025$ |
| 3rd | $-0.0018z+1.0757$ | $-3\times10^{-6}z^2-0.0009z+1.1032$ |
| 4th | $-0.0018z+1.0889$ | $-3\times10^{-6}z^2-0.0007z+1.0102$ |
| 5th | $-0.0019z+1.0803$ | $-3\times10^{-6}z^2-0.0009z+1.0069$ |

### 5.2.2 Step response

As same as the static response, the whole setup here is still the one shown in Figure 4.3. The location of the probe is also the same as before. Device #3 uses the 15mm probe and device #4 uses the 11mm one. All the experimental data of the step responses from device #3 and device #4 are collected under the same alignment as the static response, and all the electrolyte, load cell and probe stacks are in the same condition. In other words, for each different device, the setups in static response and step response are same, except for the applied input displacement functions.

**a) Step response of device #3**

Two step displacement inputs, 50μm and 100μm, are exerted on the device #3 at the speed of 3mm/s. In response to a step input of $z_p$=50μm , the probe takes 17ms to reach 50μm at the speed of 3mm/s. In Figure 5.25, the measured resistance changes of the device as a function of time for step displacement 50μm are illustrated, together with the recorded overall load which is measured from the load cell. For another step displacement input 100μm, the probe takes 33ms to reach the destination at the speed of 3mm/s. The measured resistance changes of the device as a function of time for step displacement 100μm is shown in Figure 5.27.

According to the measured overall stiffness of the device in the static response, the two step displacements of 50μm and 100μm correspond to two step loads of 120mN and 240mN, respectively. However, the overall loads recorded by the load cell are about 200mN and 300mN, respectively. The resistance changes of the 3$^{rd}$ transducer under the

step inputs of 50μm and 100μm are approximately 400Ω and 800Ω, respectively. These values are much higher than those obtained in the static measurements shown in Figure 5.16 (~200Ω and ~400Ω, respectively). Since the step response and the static response are measured under the same alignment between the probe and the device, this large discrepancy in the resistance change between the static response and the step response is believed to be caused by the mounting of the probe holder, load cell and the probe. As shown in Figure 4.5 and Figure 4.6, the mounting of these components is not rigid, and the large static displacement in the static measurement might have altered this mounting. The probe effect of squeezing the reservoir towards the $5^{th}$ transducer end is not manifested under a step input, since the resistance change of the $5^{th}$ transducer is larger than that of the $4^{th}$ transducer.

The oscillatory behavior of the resistance changes of the device is believed to result from the experimental setup, in particular, the non-rigid assembled stack of the probe holder, load cell and probe. In the previous study on this device as described in section 5.1, a single rigid probe was used, and this oscillatory behavior was not observed.

Figure 5.26 and Figure 5.28 show the power spectrum density analysis of the resistance change of the $3^{rd}$ transducer of the device, in response to the two inputs. A peak at a frequency of ~1.3kHz is observed in both analyses. This peak is believed to be the frequency of the experimental setup. As will be seen in the following subsection, the same peak is also observed in the sinusoidal response of the device.

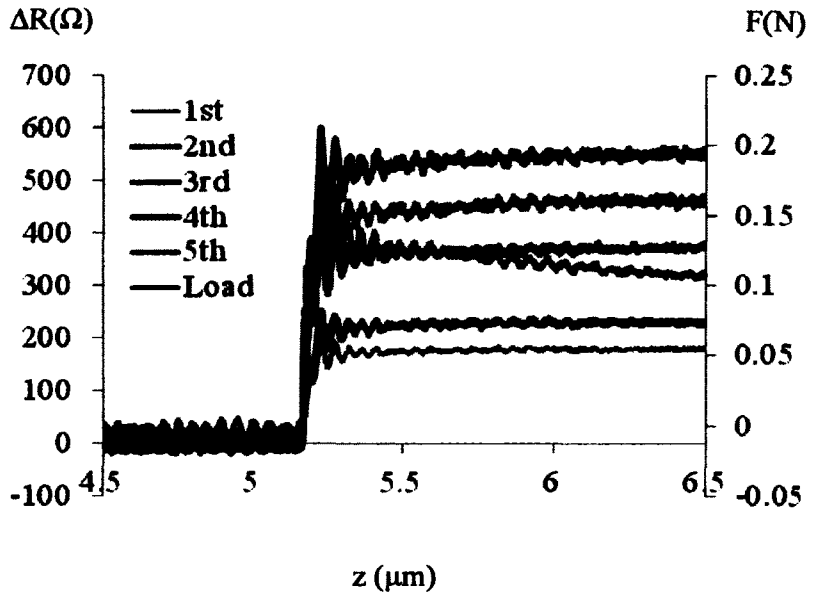


Figure 5.25 Measured resistance changes as a function of time of device #3 in response to a step input of $z_p$=50μm.

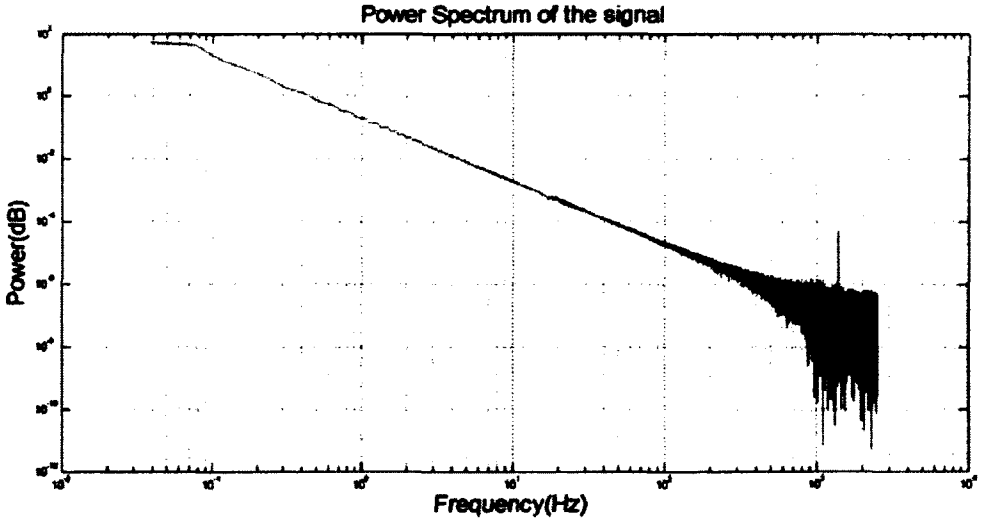


Figure 5.26 Power spectrum analysis of the voltage output of the 3rd transducer of device #3 in response to a step input of $z_p$=50μm.

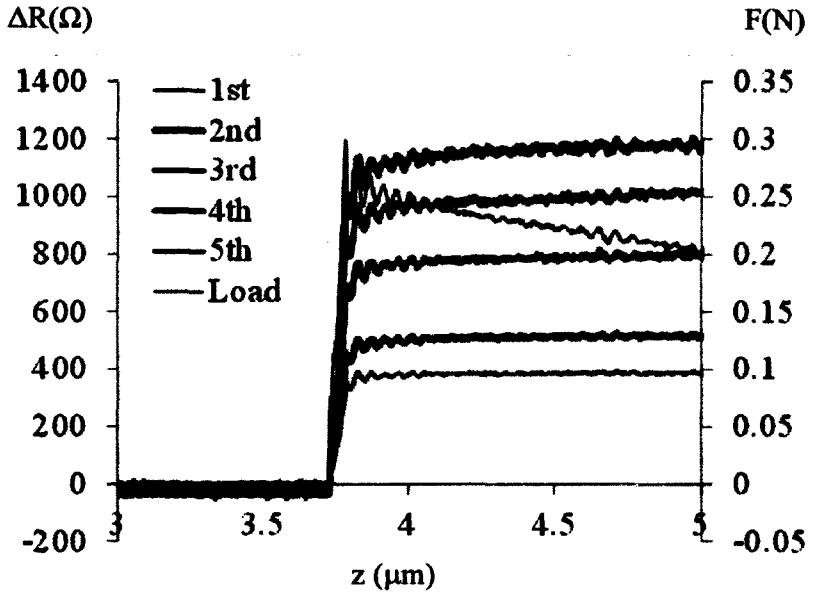


Figure 5.27 Measured resistance changes as a function of time of device #3 in response to a step input of $z_p$=100μm.

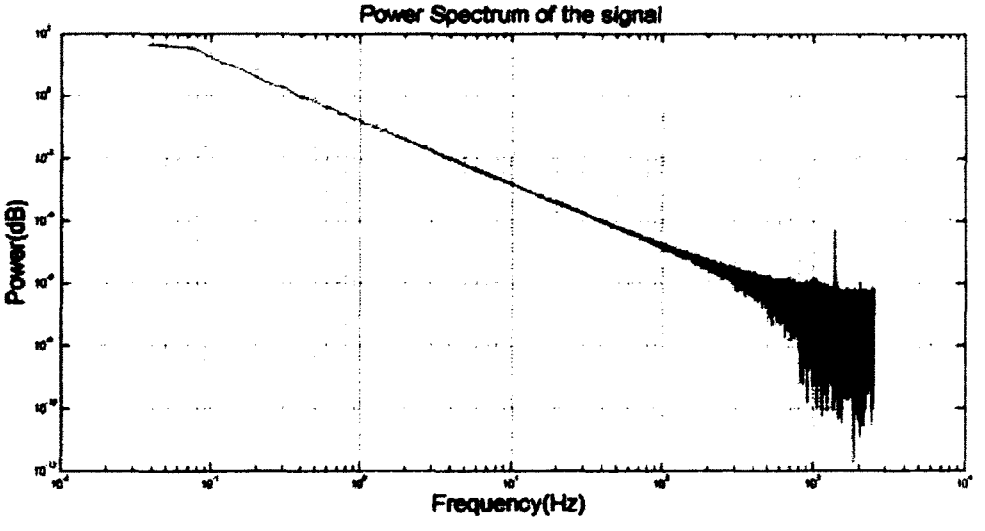


Figure 5.28 Power spectrum analysis of the voltage output of the 3rd transducer of device #3 in response to a step input of $z_p$=100μm.

**b) Step response of device #4**

For device #4, a step displacement input of 300μm is used for three times to check the stability of the device. Again, a speed of 3mm/s is exerted on the device #4. In response to a step input of $z_p$=300μm, it takes 100ms for the probe to reach 300μm at the speed of 3mm/s.

In Figure 5.29, Figure 5.30, the measured resistances and resistance changes of the device as a function of time for step displacement 300μm are illustrated respectively, together with the recorded overall load which is measured from the load cell. From these figures, it is very clear that the probe is also tilted to the 5$^{th}$ transducer. It should be noticed that the measured resistances and the resistance changes are the average values from three different measurements. As shown in Figure 5.31, a close-up plot is demonstrated there for a clearer showing of the standard derivations from the three measurements. The solid black bars represent the standard derivation and they clearly show that the three measurements are very close. That means the measurements from the device is very stable and reliable.

According to the measured overall stiffness which is obtained from the previous section in the static response of the device #4, the step displacements of 300μm correspond to a step load of 945mN since the overall stiffness is 3.15mN/μm. From the measured data, the load measured from the load cell is around 850mN and the resistance change of the 3$^{rd}$ transducer is about 2900 Ω, which also can be seen in Figure 5.29. Again, since the step response and the static response are measured under the same alignment between the probe and the device, this large discrepancy still can be considered

as the non-rigid probe setup stack, or caused by the mounting of the probe holders, load cell and the probe.

Also, this time, the whole setup stack and all the connections between the probe holders and the probe are tied up to minimize the effects of the non-rigid assembled stack. From all the plotted figures of device #4, the oscillatory behavior of the resistance changes of the device didn't show up. That verified that the problem of the oscillatory behavior in device #3 came from the non-rigid assembled stack of the probe holders, load cell and probe.

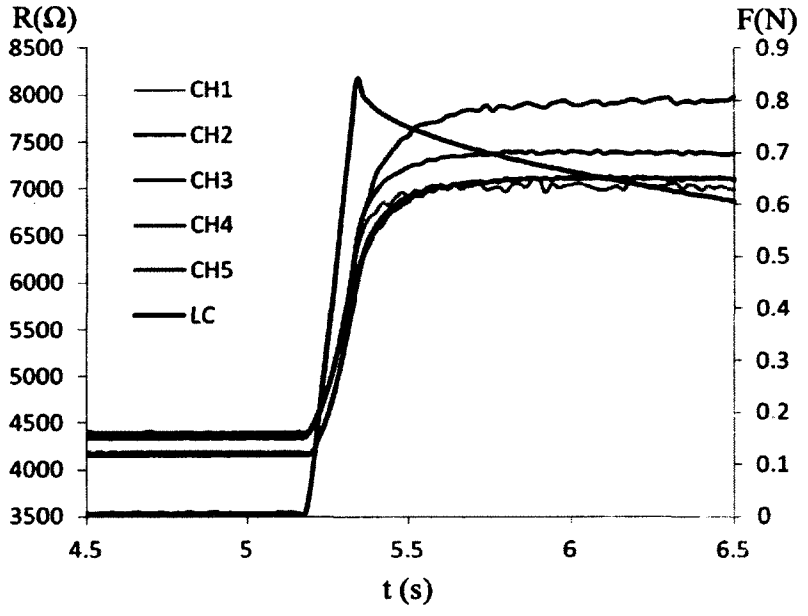


Figure 5.29 Average resistances of device #4 as function of time in response to a step of 300μm.

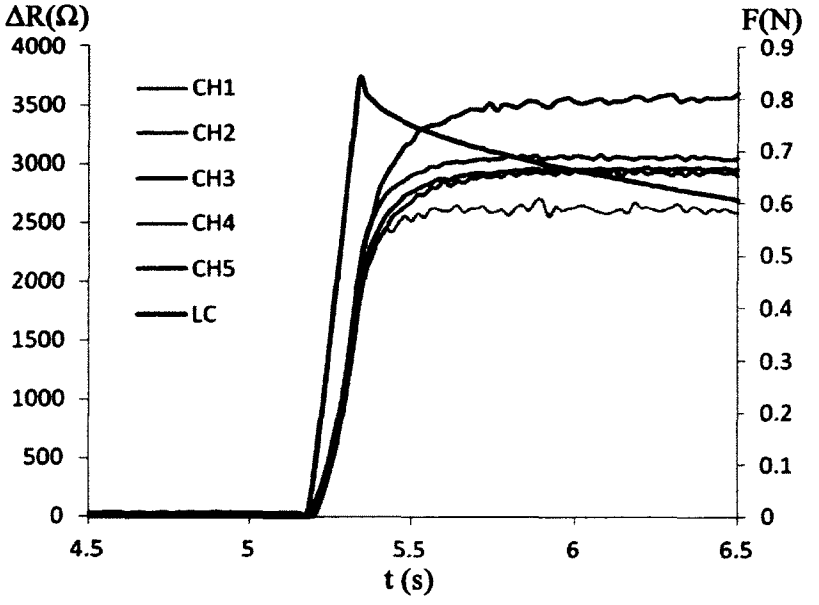


Figure 5.30 Average resistance changes of device #4 as function of time in response to a step of 300μm.

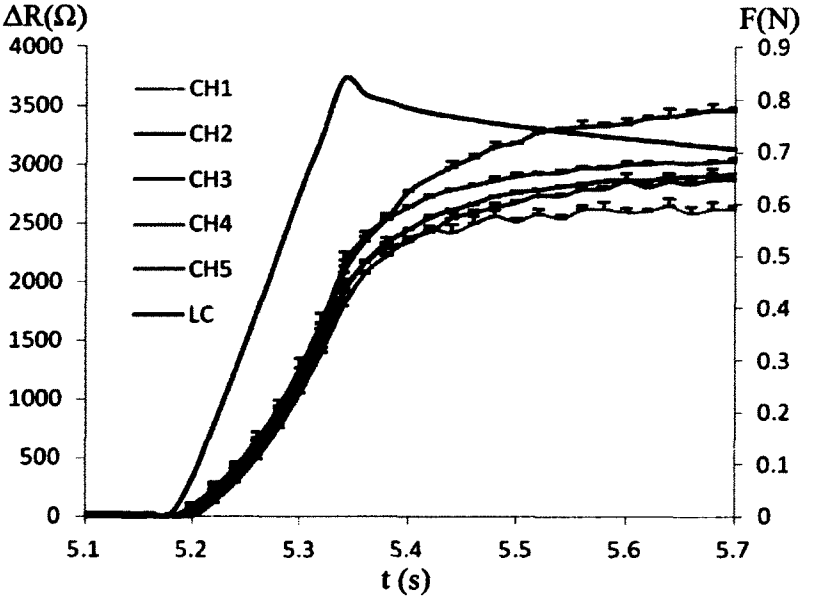


Figure 5.31 A close up of average resistance changes of device #4 as function of time with standard derivation in response to a step of 300μm.

### 5.2.3 Sinusoidal response

In this section, in order to generate a sinusoidal response, a function generator is used to control a shaker which is connected to an amplifier to amplify the signal from function generator. This shaker is from Linc Dynamic Systems and has a model number of 201. The whole setup of the sinusoidal or dynamic response is shown in Figure 4.4. From the figure, it is very clear that, compared to the static and step response, the micropositioner is replaced by this shaker, and this shaker can be controlled by the second function generator to have an input signal. Still, for device #3, that 15mm long probe is used and for device #4, the probe is the 11mm one. The location of the probe is shown in Figure 5.12.

Two different sinusoidal inputs are used to examine the devices. One input signal has a frequency of 10Hz and amplitude of 1V, and the other one has a frequency of 100Hz and amplitude of 3V.

#### a) Sinusoidal response of device #3

As mentioned before, two different sinusoidal inputs are used to examine the response of the device. In response to a sinusoidal input with a frequency of 10Hz and amplitude of 1V, Figure 5.32 and Figure 5.33 show the voltage outputs and the corresponding resistance changes of the device as a function of time, respectively. This input signal is represented by the signal of the function generator controlling the shaker. Unfortunately, the measurement of the overall load isn't plotted in the figures since the lack of the load cell measurement. Overall, the resistance changes of the device follow the pattern of the sinusoidal input. The voltage outputs and their corresponding resistance

changes are completely in phase, in that the resistance changes are calculated from the voltage outputs by using Eq. (7).

Apparently, a time delay is expected between the signal of the function generator and the true input signal (from the probe) exerted on the device, due to non-zero damping of the device. Please note that the resistance change of the 1st transducer is completely out of phase with the resistance change of the rest transducers. This is due to the fact that the probe with its tip toward the 1st transducer and the end is tilted toward the 5th transducer: when the microstructure deflection above the rest transducers is downward, the microstructure deflection above the 1st transducer is upward.

Owing to the nonlinear $\Delta R$-$z_p$ relation given in Eq. (14), neither the voltage outputs nor the resistance changes should contain a pure sinusoidal signal with a single frequency. In order to obtain the frequency characteristics of the device response to a sinusoidal input, power spectrum density analysis is conducted on the resistance changes in Figure 5.34, which shows the magnitudes of the resistance change of the 3rd transducer as a function of frequency. Clearly, there are two peaks at 10Hz and 20Hz, respectively, with the peak at 10Hz being dominant. The first peak corresponds to the input frequency, while the second peak happens at the frequency doubling the input frequency. Also from this figure, a frequency ~1.3kHz can be seen as the one in the step response is observed, it is further verified that this peak comes from this assembled stack.

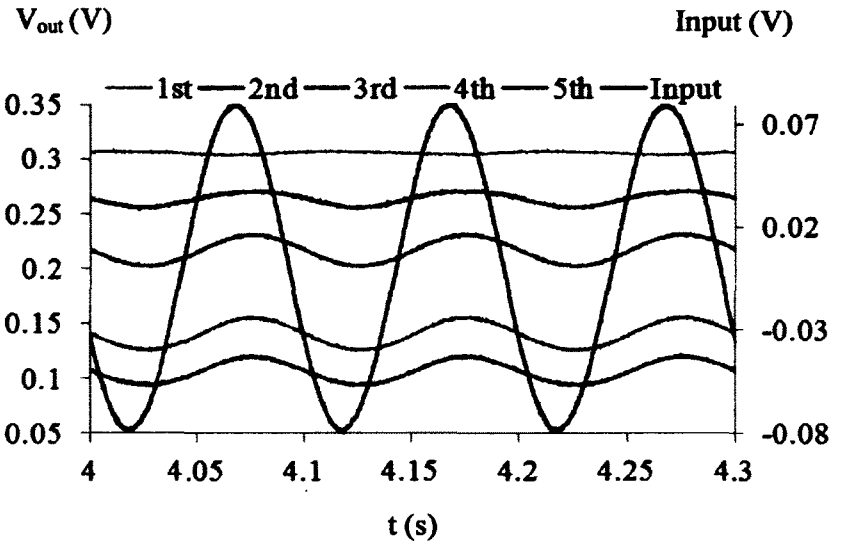


Figure 5.32 Measured voltage output of transducers as function of time of device #3 with a sinusoidal input of 10Hz and 1V.

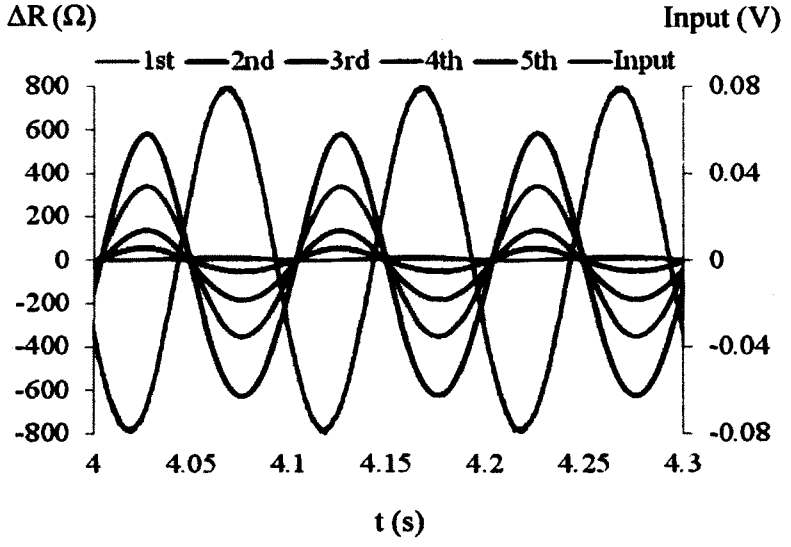


Figure 5.33 Resistance changes of transducers as function of time of device #3 with a sinusoidal input of 10Hz and 1V.

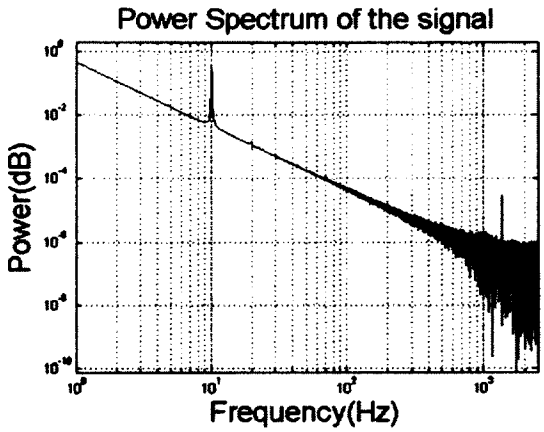


Figure 5.34 Power spectrum density of the voltage output of the 3rd transducer as a function of frequency, in response to a sinusoidal input signal with a frequency of 10Hz.

Figure 5.35 shows the measured voltage output against the applied displacement of the device #3, in response to a sinusoidal input with a frequency of 100Hz and amplitude of 3V. After this voltage output has been converted to resistance changes according to the Eq. (7), the result is plotted in Figure 5.36. It should be noticed that because the probe is tilted to the 5th transducer, the 1st transducer gives an opposite trend due to the area of the microchannel in the location of the 1st transducer enlarged when the others get squeezed and the electrolyte flow towards the 1st one. From the 2nd transducer, the effect of alignment also can be seen since the 2nd one shows a doubled frequency. That means the 2nd one get affected by both the 3rd one and the 1st one.

Again, a power spectrum density analysis has been conducted as shown in Figure 5.37, and this PSD analysis of the device, in response to a sinusoidal input with a frequency of 100Hz, giving rise to the same conclusion as those shown in Figure 5.34. Similar to the response with a frequency of 10Hz, this figure shows a clear peak in 100Hz

which indicated the operation frequency. Finally, it is worth pointing out that multiple peaks (overtones) at multiples of 100Hz in Figure 5.37 are more conspicuous than those at multiples of 10Hz in Figure 5.34. Note that the same assembled stack of the probe holder, load cell and probe was utilized for the sinusoidal response of the device, so that same peak at ~1.3kHz shows up again.

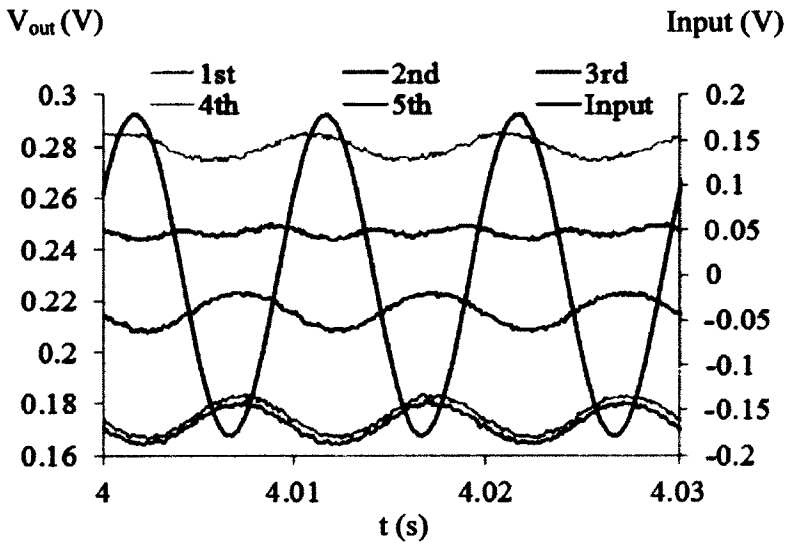


Figure 5.35 Measured voltage output of transducers as function of time of device #3 with a sinusoidal input of 100Hz and 3V.

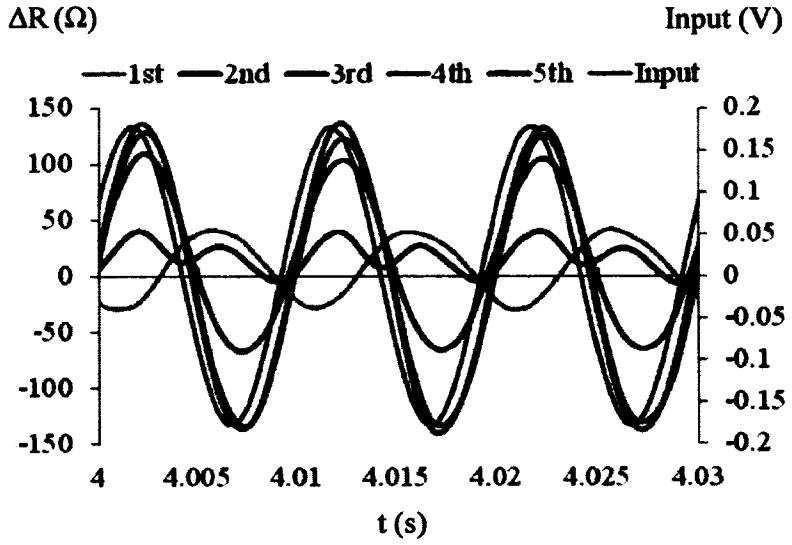


Figure 5.36 Resistance changes of transducers as function of time of device #3 with a sinusoidal input of 100Hz and 3V.

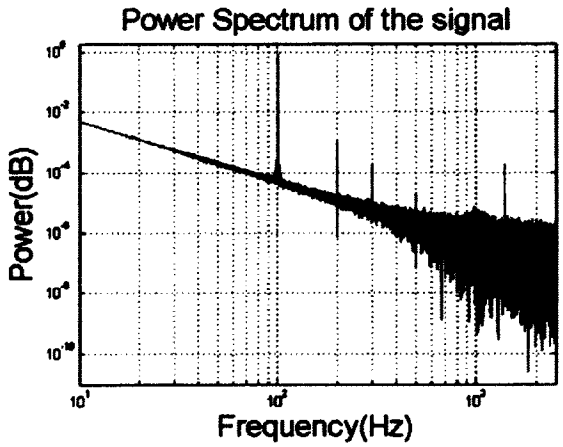


Figure 5.37 Power spectrum diagram of the voltage output of the 3rd transducer as a function of frequency, in response to a sinusoidal input signal with a frequency of 100Hz.

**b) Sinusoidal response of device #4**

The sinusoidal response of device #4 is shown in Figure 5.38 to Figure 5.46 for different sinusoidal inputs. As before, one input has a frequency of 10Hz and amplitude of 1V and the other one has a frequency of 100Hz and amplitude of 3V. This time, a measurement of force from load cell is included.

Figure 5.38 shows the resistance values of the five transducers as the function of the time, and Figure 5.39 represents the resistance changes as the function of time. It should be noticed that the displacement of the microstructure on top of the each transducer can be calculated using the relation of the resistance change ratio $1/(\Delta R_d/R_{d0}+1)$ versus the applied displacement of device #4, which is obtained from the static response as shown in Figure 5.24 and the curving fitting equations as shown in Table 5.5, the calculated results or the displacements as the function of time is shown in Figure 5.40 for the input signal of 10Hz and 1V. This method complements the lack of measurement of displacements from the vibration shaker.

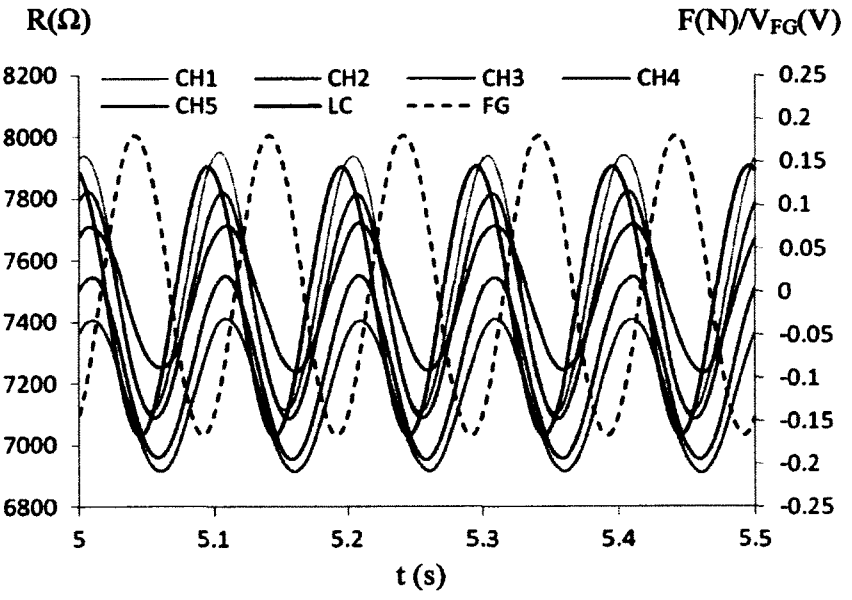


Figure 5.38 Resistance of transducers as function of time of device #4 with a sinusoidal input of 10Hz and 1V.

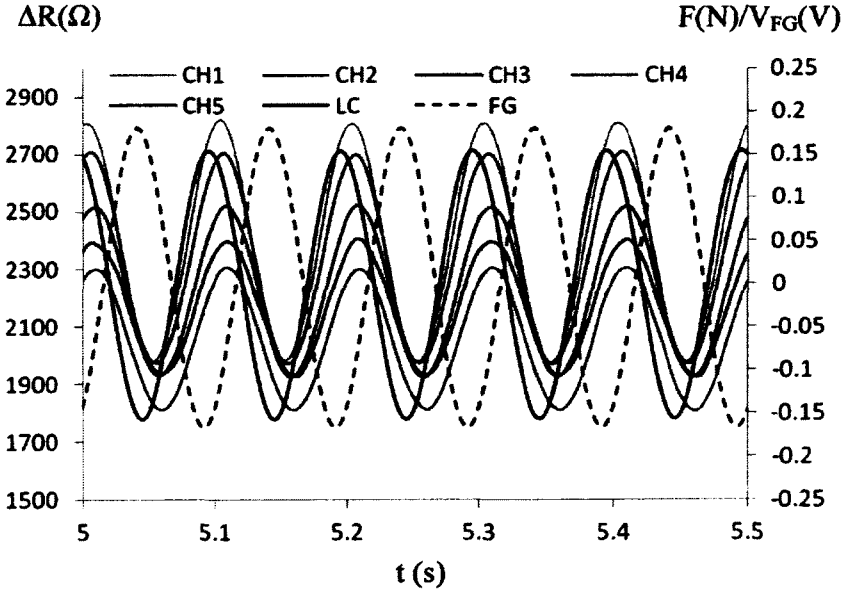


Figure 5.39 Resistance changes of transducers as function of time of device #4 with a sinusoidal input of 10Hz and 1V.

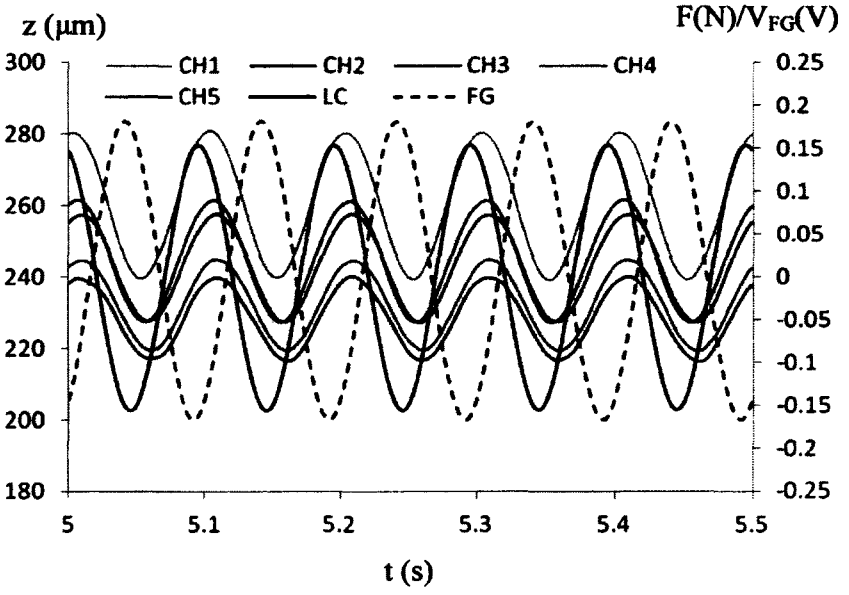


Figure 5.40 Defections of microstructure on top of different transducers as function of time of device #4 with a sinusoidal input of 10Hz and 1V.

Figure 5.41 shows the power spectrum diagram of the voltage output of the 3rd transducer as a function of frequency for device #4 with a sinusoidal input of 10Hz and 1V. It is very clear that the frequency response from the device shows the dominant frequency of 10Hz and this device can be used for a time harmonic detection.

Figure 5.42 plots the phase shift of the 3rd transducer with a sinusoidal input of 10Hz and 1V. According to the phase diagram of cross spectrum, the phase shift of the 1st transducers is around -150°, the 2nd one is -140°, and rest of the transducers are all around -130°, which response to time delay of 42ms, 39ms and 36 ms, respectively. That means the transducers have a time delay compared to the load cell. Based upon the different transducers, this time delay varies a little bit. Because the 3rd one is in the middle, thus

represents the average value of the time delay, we can say that the device has a time delay of 36ms. Compared to the time delay we got from the static and step response, this value is much smaller and dependable.

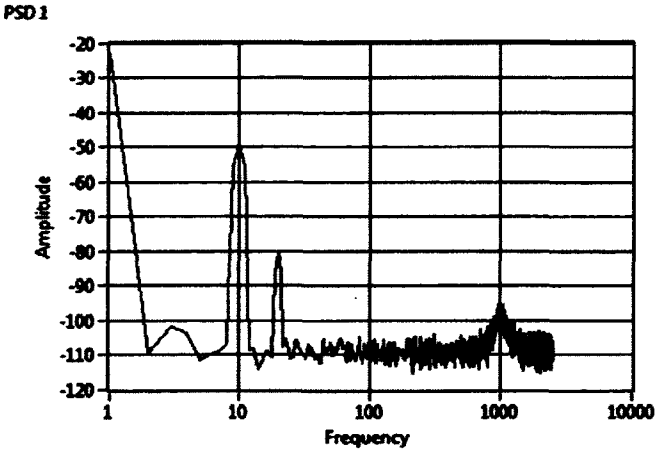


Figure 5.41 Power spectrum analysis of the voltage output of the 3rd transducer as a function of frequency for device #4 with a sinusoidal input of 10Hz and 1V.

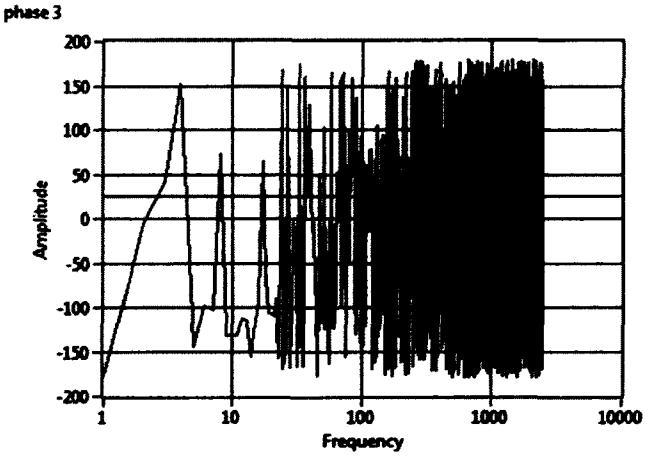


Figure 5.42 Cross spectrum analysis of the phase shift of the 3rd transducer as a function of frequency for device #4 with a sinusoidal input of 10Hz and 1V.

Figure 5.43 to Figure 5.46 show the dynamic response of the device #4 with an input frequency of 100Hz and amplitude of 3V. Again, the measurement of the load cell is included in a solid black line shown in these figures. Different from device #3, all measurements from device #4 are in phase. The differences of the resistance values and resistance changes for each transducer are believed from the fabrication variations as they keep the same trend from the static, step and dynamic response.

Figure 5.43 shows the resistance of transducers versus the time for a sinusoidal input of 100Hz and 3V, and Figure 5.44 shows the resistance changes of each transducer as the function of time. Figure 5.45 represents the calculated displacements according to the curving fitting equation which is obtained from Table 5.5. The reason we didn't use the value of load cell is that this piezo type of load cell can just measure the dynamic load. As a result, the load cell measurement can just be used to get the peak-to-peak load differences, not the real force from the initial position. So the load cell measurement in sinusoidal response only functions as a reference to check the calculation of the curving fitting equation.

Figure 5.46 represents the power spectrum density of the voltage output of the 3rd transducer as a function of frequency for device #4, in response to a sinusoidal input with a frequency of 100Hz and 3V. From this figure, a peak in 100Hz is clearly appeared, as well as the multiply peaks at multiples of 100Hz, as we mentioned before for device #3.

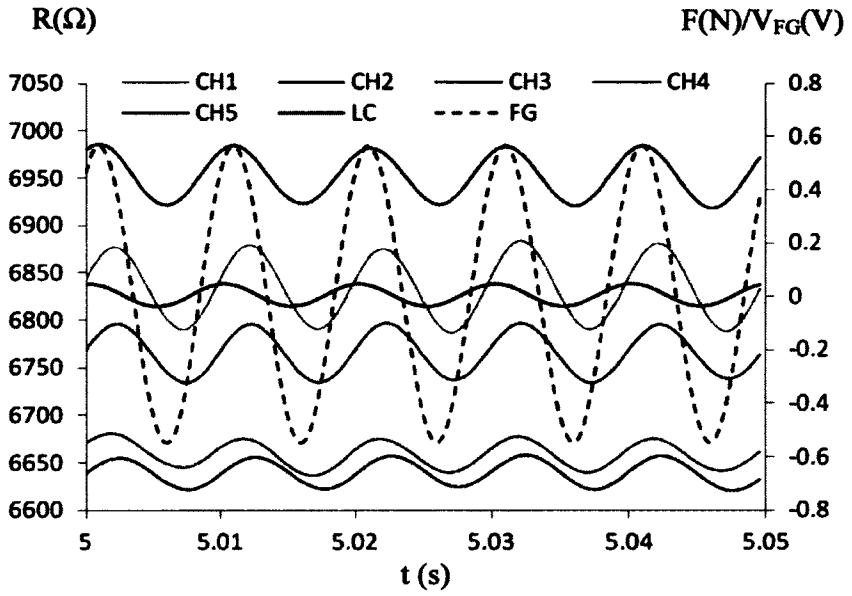


Figure 5.43 Resistance of transducers as function of time of device #4 with a sinusoidal input of 100Hz and 3V.

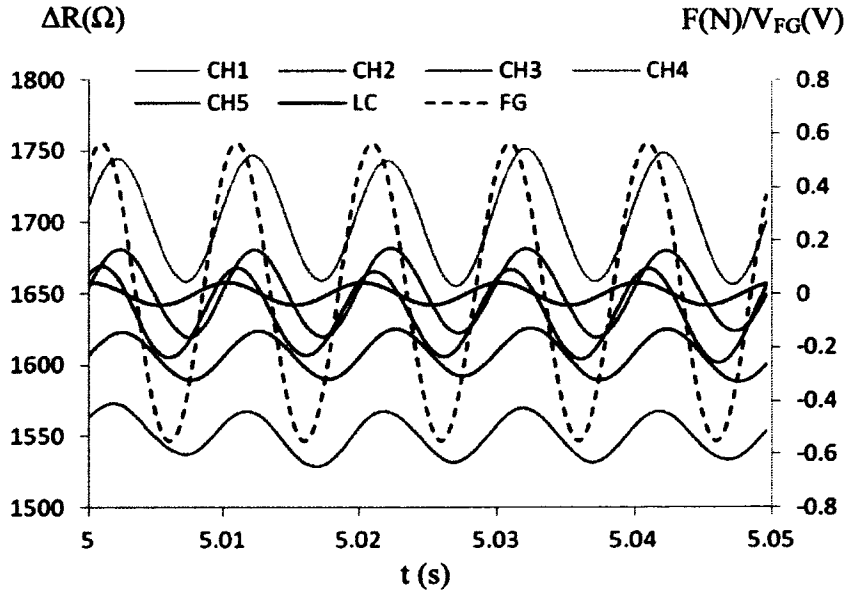


Figure 5.44 Resistance changes of transducers as function of time of device #4 with a sinusoidal input of 100Hz and 3V.

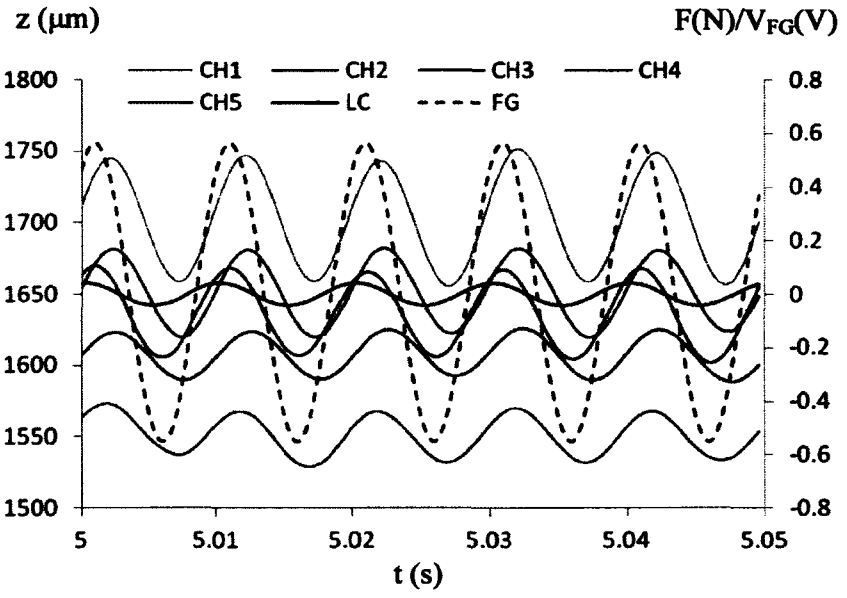


Figure 5.45 Defections of microstructure on top of different transducers as function of time of device #4 with a sinusoidal input of 100Hz and 3V.

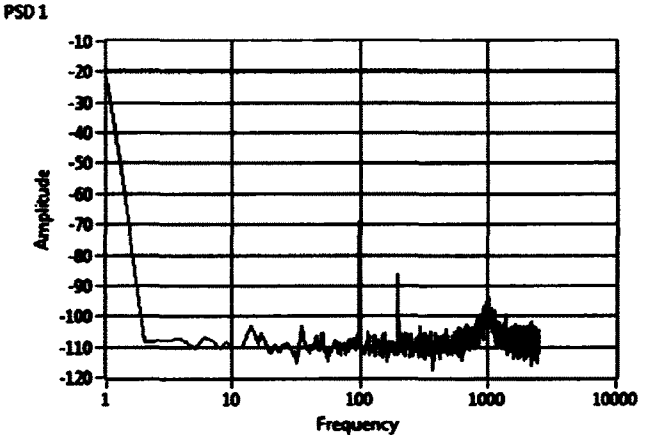


Figure 5.46 Power spectrum density of the voltage output of the 3rd transducer as a function of frequency for device #4 with a sinusoidal input of 100Hz and 3V.

# CHAPTER 6

# PERFORMANCE ANALYSIS

After static, step and dynamic responses are characterized, the performances of devices should be analyzed to obtain the performance parameters. First of all, to verify the relation between the force $F_d$ and displacement $z_p$, a finite element analysis (FEA) of the microstructure should be resorted to accurately predict the relation under uniform and non-uniform continuous distributed loads. Then a lumped-element model is built up to describe the dynamic behavior of the device. Later on, a few critical performance parameters are obtained by analyzing the device #3 to show the performance analysis procedure.

By simplifying the microstructure as five identical springs and assuming uniform continuous distributed loads, the dependence of the $F_d$-$z_p$ relation is approximately correlated to the design parameters of the microstructure. Similarly, by treating a resistive transducer as a deformable rectangular conductive block, dependence of the $\Delta R$-$z_p$ relation on the design parameters of the transducers is obtained, as given in Eq. (14).

Based on Eqs. (1) and (14), if the microstructure design varies and the transducer design is kept the same, then the same applied displacement will lead to different load magnitudes but the same resistance changes. Conversely, if the transducer design varies and the microstructure design is kept the same, then the same applied displacement will give rise to the same load magnitude but different resistance changes. As listed in Table 2.1 Dimension and key design parameters of the PDMS-based device, although the microstructure and the transducer share two common design parameters, transducer

spacing and microchannel width, they have their own design parameters, top plate thickness and microchannel height. These two design parameters can be adjusted independently for measuring extremely small and large applied displacement or loads.

Characterization of the microstructure is required to obtain the $F_d$-$z_p$ relation, and characterization of the transducers is needed to obtain the $\Delta R$-$z_p$ relation. In potential applications, the input and output of the device are the applied displacement and the resistance changes, respectively, giving rise to the $\Delta R$-$z_p$ relation. Therefore, a load cell is incorporated in the experiment in order to obtain the $F_d$-$z_p$ relation and Finite Element Analysis of the microstructure should also be conducted for its verification, as will be seen in the following subsection.

## 6.1 Finite element model

In this section, for accurate prediction of the $F_d$-$z_p$ relation of the microstructure, a FEA model is resorted to simulate the performance characterization of the devices using a FEA software COMSOL, owing to the irregular geometry of the microstructure. Since the configurations of the device #3 and device #4 are similar, only the simulation of device #3 has been analyzed here. Figure 6.1 shows the top view and bottom view of the finite element COMSOL model of the PDMS-based microfluidic device. The dimension of the device and physical properties of PDMS used here are from the Table 2.1 and Table 2.2 respectively.

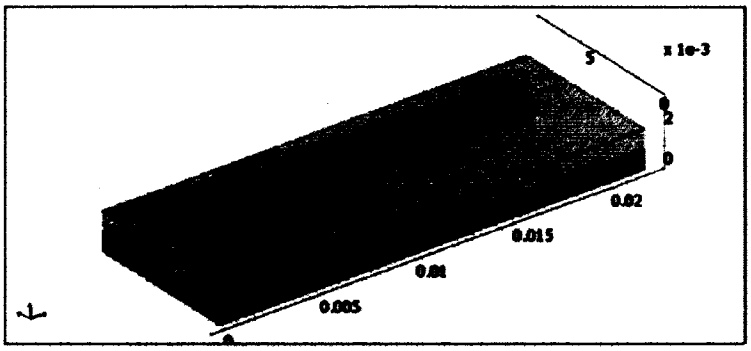


(a)

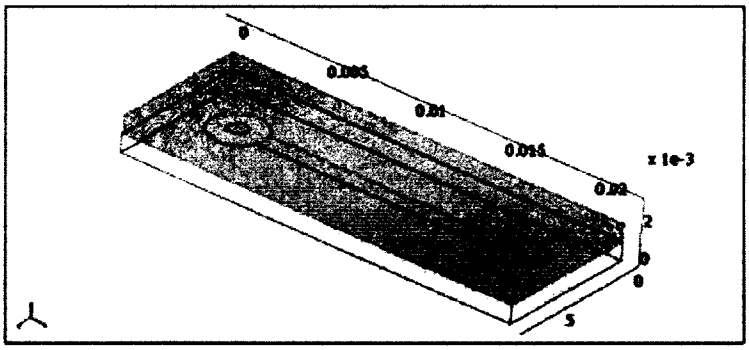


(b)

Figure 6.1 The finite element COMSOL model of PDMS-based microfluidic device (a) top view with probe (b) bottom view of the model.

Two modules are employed to simulate the static and dynamic response; one is static analysis for static response and another one is frequency response analysis for dynamic response. Under a static condition, the calculation of the microstructure stiffness will not be affected, thus, electrolyte underneath the microstructure is not included in the model. In the static simulation, several different displacements of the rigid probe are applied as the different inputs for the microstructure and then the overall reaction forces of the microstructure for different inputs are simulated. Figure 6.2 shows the simulated $F_d$-$z_p$ relation of the microstructure for static response comparing to the measured results

of load cell in static response for device #3. It should be noticed that the value of Young's modulus for PDMS varies with temperature, mixing ratio and time [48], and the range of the value is normally between 300kPa to 800kPa [49]. Since we cured the PDMS in room temperature for eliminating the bubbles and normally the Young's modules of PDMS will decrease in a lower curing temperature, the Young modulus of our PDMS microstructure should be close to the lower bound. Therefore, we chose 350kPa as the Young's modulus to do the simulation.

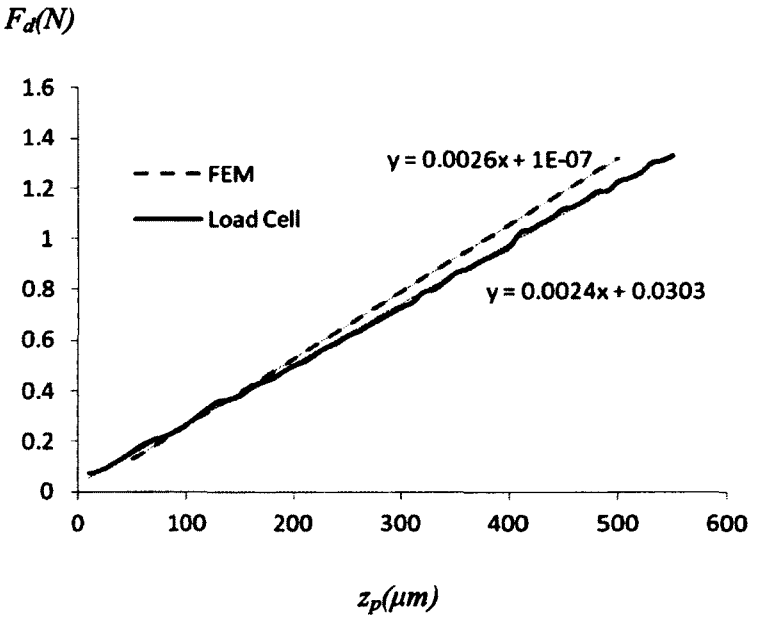


Figure 6.2 Simulation result for static response comparing to measured value from device #3.

Figure 6.3 shows the dynamic analysis of the simulation results. From the figure (a), it is very clear that the whole microstructure and the rigid probe together are separated to 25,567 finite elements, and (b) shows the simulated vibration mode for the device operation, which give us a natural frequency of 2,868Hz for the device itself.

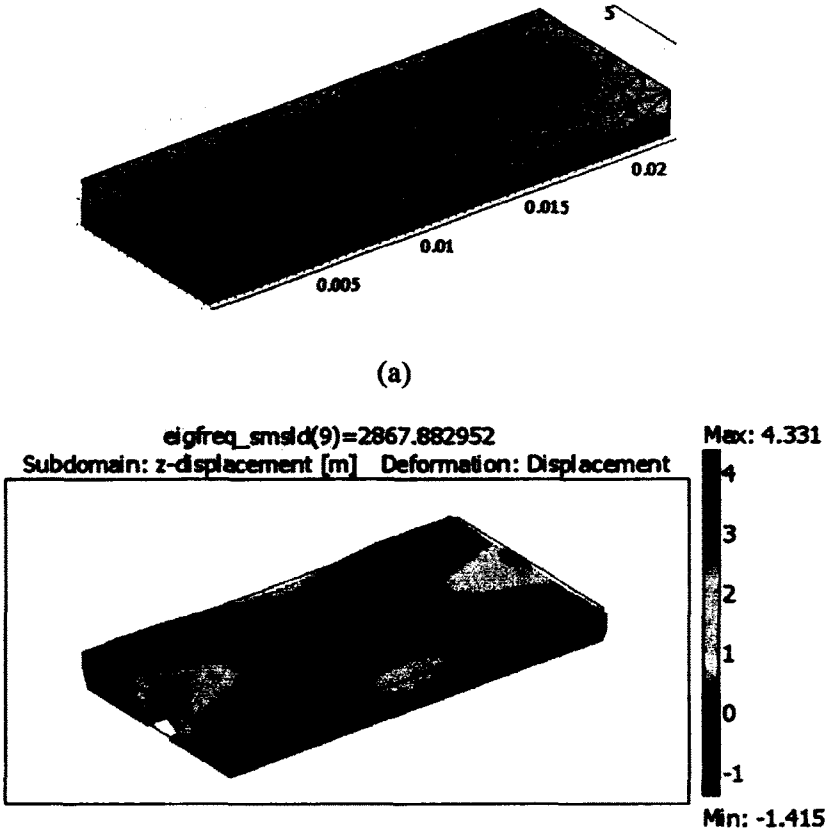


Figure 6.3 Finite element analysis of the microstructure in COMSOL (a) finite element model of 25,567 elements (b) simulated vibration mode for the device operation.

## 6.2 Lumped-element model

Let's take device #3 as the example to build the lumped-element model. Although the microstructure deflection varies continuously with the location (along its width and length or along the $x$-axis and $y$-axis) on the microstructure, the whole microstructure can

be simplified as a rigid plate with an equivalent mass of $m_d$, attached to a spring with an equivalent stiffness of $k_d$, whose value is 4.08mN/μm for device #3, as determined by the simulation result. The microstructure deflection is equal to the applied displacement of the probe, $z_p$. In the meantime, the microstructure is subjected to viscous damping of the electrolyte underneath the microstructure. Consequently, a lumped-element model shown in Figure 6.4 can be utilized to describe the dynamic behavior of the device:

$$m_d \frac{d^2 z_P}{dt^2} + c_d \frac{dz_P}{dt} + k_d z_P = F_d(z_P) \tag{17}$$

where $c_d$ denotes the damping coefficient of the microstructure and $F_d(z_p)$ is the overall load exerted by the rigid probe.

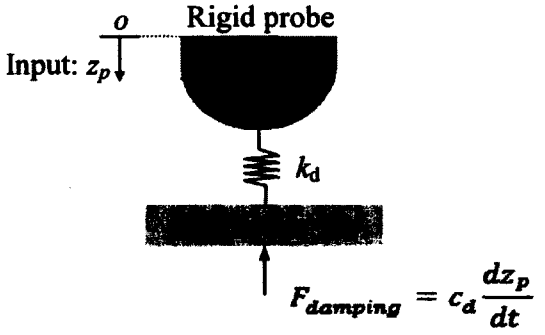


Figure 6.4 Schematic of the lumped-element model of the whole PDMS-based microfluidic device

The vibration simulation of the microstructure and the simulated natural frequency of the vibration mode for operating microstructure is around 3kHz, as shown in Figure 6.3 (b). Therefore, the equivalent mass of the device is estimated as $m_d = 1.26\times10^{-5}$kg using the formula

$$m_d = \frac{k_d}{\omega_n^2}$$

Consequently, the maximum frequency of a sinusoidal input should be kept less than $f_{max} \leq f_d/5$ or 600Hz [50].

The microchannel height is very small as compared with the microchannel width ($h_E/w_E$ <<1), so electrolyte motion in the microchannel can be described using the lubrication theory [51]. The damping force is mainly the hydrodynamic force taking the following relation [51]:

$$F_{damping}(t) = \frac{\mu(w_E L)^2}{h_E^3}\frac{dz_p}{dt} \tag{18}$$

This hydrodynamic force is equivalent to the squeeze-film damping effect caused by the interaction of the microstructure motion and viscous fluid flow, where $\mu$ is the electrolyte viscosity. Thus, according to this equation, the damping coefficient $c_d$ can be estimated to be $c_d$=5.906kg/s using

$$c_d = \frac{\mu(w_E L)^2}{h_E^3}$$

Therefore, the damping factor $\zeta$ and the mechanical quality factor of the device $Q$ can be obtained using the following formula respectively:

$$\zeta = \frac{c_d}{2\sqrt{km_d}}$$

$$Q = \frac{1}{2\zeta} = \frac{\sqrt{km_d}}{c_d}$$

The calculated mechanical quality factor of the device is $Q$=0.0383, indicating that this device is well overdamped. Accordingly, the response of the device to a step input is estimated to 4.3ms by the following expression [52]:

$$t_s = \frac{3}{\zeta\omega_n - \sqrt{\zeta^2 - 1}\omega_n} \tag{19}$$

where $\zeta$ denotes the damping factor of the device. While the response time of the load cell is less than 6μs based upon the datasheet of Kistler 9712-type load cell, the response time of the interface electronics is around 12.5ms as mentioned before. Thus, the estimated response time of the device #3 is a little bit above 20ms in step response. Table 6.1 shows the components and their values of device parameters based upon the equivalent lumped-element analysis of the device #3.

Table 6.1 Components and their values of the equivalent lumped-element of the device #3

| Device parameter | Value | Symbol |
|---|---|---|
| Equivalent mass | $1.26\times10^{-5}$kg | $m_d$ |
| Equivalent stiffness | 4.08mN/μm | $k_d$ |
| Equivalent Q | 0.0383 | $Q$ |
| Natural frequency | 2.868 kHz | $\omega_d/2\pi$ |

## 6.3 Transducer spacing - spatial resolution

Spatial resolution is commonly defined as the distance between the neighboring data recording points. Therefore, spatial resolution of this device is equivalent to transducer spacing, $d_E$. Although the continuous deflection of the microstructure is advantageous [5, 29, 31, 53], the crosstalk between neighboring resistive transducers should be minimized in order to accurately capture the continuous deflection of the microstructure at discrete locations of the transducers. From our previous study, the

average initial resistances of the transducers of a device which has the identical design but filled with 0.1M NaCl were measured to be 16kΩ [53]. Since the electrical resistivity of 0.1M NaCl is 1Ω·m [44], the effective length, $d_{eff}$, of a transducer is approximately half of the transducer spacing, based on Eq. (5), and thus an isolation zone exists between the neighboring resistive transducers, as shown in Figure 2.5. Then, by interpolation, the effective length of a transducer in a device filled with EMIDCA is also half of the transducer spacing. The measured average initial resistance of around 3.3kΩ of this device indicates that the electrical resistivity of EMIDCA is about 0.2Ω·m. It is worth noting that the reported electrical resistivity of EMIDCA in the literature varies significantly. Therefore, this physical property is derived here by comparing it with that of 0.1M NaCl. As long as the transducer spacing is much larger than the microchannel width (or $d_E/w_E \geq 1.5$), transducer crosstalk is not expected. Evidently, as the transducer spacing is reduced, the microchannel width must be decreased accordingly to avoid transducer crosstalk. Meanwhile, transducer spacing in a device does not need to be the same for all the transducers. As long as an isolation zone is kept between neighboring transducers, transducer spacing along the microstructure length can be adjusted to accommodate the heterogeneous structure of a soft material with varying feature sizes within it.

## 6.4 Sensitivity of the device

Load sensitivity is one of the most critical performance parameters of the device. It can determine how sensitive this device is and the ability of a device to convert a certain force into an electrical signal. In current device, the resistance change is the function of

the applied displacement or applied force. The sensitivity of the device can be obtained from Eq. (10) and Eq. (11), according to $\Delta R - z_p$ relation or $\Delta R - F_d$ relation. The sensitivity of the device in term of the applied displacement is given by the slope of the $\Delta R - z_p$ relation, while the sensitivity of the device in terms of the overall load is given by the slope of the $\Delta R - F_d$ relation. Eq. (10) and Eq. (11) are recalled here:

$$S_{z_p} = \frac{d\Delta R}{dz_p} = R_0 \frac{\eta/h_E}{\left(1 - z_p\eta/h_E\right)^2} \quad (Unit: \Omega/\mu m)$$

$$S_{F_d} = \frac{d\Delta R}{dF_d} = R_0 \frac{\eta}{k_d h_E \left(1 - \frac{F_d \eta}{h_E k_d}\right)^2} \quad (Unit: \Omega/mN)$$

Due to the nonlinear relation of the resistance change and the applied displacement, the sensitivity of the device is the function of the applied displacement. Because different segments of the microstructure have different deflections when a non-uniform distributed load or displacement is applied, the resistance values of each transducer will be different. In addition, the sensitivity of the device will also be different. Under a uniform distributed displacement input, the sensitivity of a segment to an applied displacement is the same as the sensitivity of the device since the displacement for each segment is the same. But for a uniform distributed applied load input, the sensitivity of a segment to load is five times of the overall sensitivity since the stiffness and the load in a segment are one fifth of the overall values. Figure 6.5 and Figure 6.6 illustrate the sensitivity of device #3 in terms of displacement and overall load respectively. These figures indicate that the sensitivity varies with displacement.

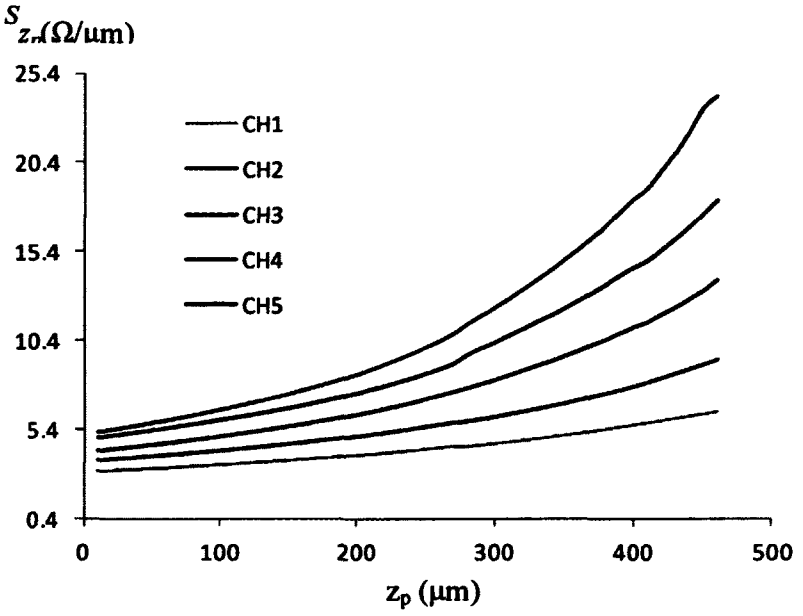


Figure 6.5 Sensitivity of device #3 in term of displacement.

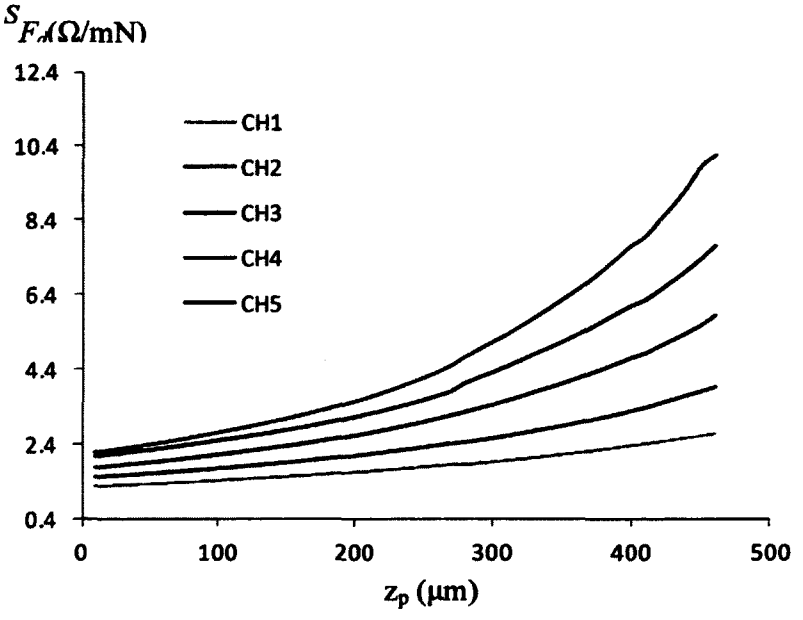


Figure 6.6 Sensitivity of device #3 in term of overall load.

Table 6.2 shows the sensitivity of the device #3 in a displacement of 300μm. It should be noticed that, in the figures and the table, the number of the segments is corresponding to the related transducers. Because the probe was not aligned perfectly and it tilted towards 5$^{th}$ transducer, so it can be considered as a non-uniform distributed load. That is why each segment has different sensitivity.

Table 6.2 Sensitivity of the device #3 in displacement of $300\mu m$ ($z_p$=$300\mu m$)

| Segment No. | 1$^{st}$ | 2$^{nd}$ | 3$^{rd}$ | 4$^{th}$ | 5$^{th}$ |
|---|---|---|---|---|---|
| Sensitivity in term of displacement ($\Omega/\mu m$) | 4.737 | 6.324 | 8.353 | 12.325 | 10.382 |
| Overall Sensitivity in term of displacement ($\Omega/\mu m$) | 8.076 | | | | |
| Overall Sensitivity in term of load ($\Omega/mN$) | 3.408 | | | | |

## 6.5 Load resolution

There are two types of intrinsic noise sources which are from the device itself and can determine the load resolution of the device. These two types of intrinsic noise sources are Brownian noise of the microstructure which is from the mechanical structure and Johnson noise of resistive transducers which is from the electrical side. These two noises of the device can be translated into the corresponding forces or the displacements of the device. Thus, the overall noise of the device can be determined by obtaining the minimum resolvable overall load and minimum resolvable displacement [54]. It should be noticed that units are added to the expressions in the following equations to show the different forms of noise sources corresponding to load or displacement.

From Brownian motion [50, 54, 55], the mechanical noise force or minimum resolvable overall load of the microstructure can be determined by:

$$F_{noise\_M} = \sqrt{\frac{4k_B T k_d \Delta f}{\omega_d Q}} \ (Unit: N) \tag{20}$$

where $k_B$ is the Boltzmann's constant; $T$ is room temperature; $k_d$ is the equivalent stiffness of device from simulation, and the value is 4.08mN/μm for device #3; $\Delta f$ is the operation bandwidth; $\omega_d$ denotes the angular natural frequency of the microstructure; and $Q$ denotes the mechanical quality factor of the microstructure. By using Hooke's law, the minimum resolvable displacement is then obtained from:

$$z_{noise\_M} = \frac{F_{noise\_M}}{k_d} \ (Unit: \mu m) \tag{21}$$

A resistive transducer suffers Johnson noise that is dependent on its resistance, R, and the temperature, $T$. This noise can be expressed as a current noise:

$$i_{noise} = \sqrt{\frac{4k_B T k_d \Delta f}{R}} \ (Unit: A) \tag{22}$$

Since the output of a transducer is virtually grounded by the transimpedance amplifier, the resistance of a transducer, in response to an applied displacement, affects its AC sense current by:

$$I_{z_p} = \frac{v_{pp}}{2R(z_p)} \ (Unit: A) \tag{23}$$

Accordingly, the total current going through a transducer is the sum of the noise current and the current going through the resistive transducer:

$$I_{z_p} + i_{noise} = \frac{v_{PP}}{2\left[R(z_p) + \Delta R_{noise}\right]} \ (Unit: A) \tag{24}$$

where the equivalent resistance change from the noise current is denoted by $\Delta R_{noise}$. When the noise current is much smaller than the current going through the resistor, $i_{noise} << I_{zp}$, the equivalent resistance of the noise current is given by:

$$\Delta R_{noise} = -\frac{2R^2(z_p)}{v_{PP}} i_{noise} = -\frac{2R^{3/2}(z_p)}{v_{PP}} \sqrt{4k_B T \Delta f} \ (Unit: \Omega) \tag{25}$$

On the other hand, the electrical noise of the device is determined by the equivalent resistance change from the noise current of the transducer divided by the sensitivity of the device, and thus the minimum resolvable load and displacement from a transducer are estimated by the following expressions:

$$F_{noise\_E} = -\frac{2R^{3/2}(z_p)}{v_{PP} S_{F_d}} \sqrt{4k_B T \Delta f} \ (Unit: \mathrm{N}) \tag{26}$$

$$z_{noise\_E} = -\frac{2R^{3/2}(z_p)}{v_{PP} S_{z_p}} \sqrt{4k_B T \Delta f} \ (Unit: \mu m) \tag{27}$$

Consequently, the minimum resolvable load and displacement of the device is a combination of its two uncorrelated noises from the microstructure and the resistive transducers:

$$F_{min} = \sqrt{F_{noise\_M}^2 + F_{noise\_E}^2} = \sqrt{4k_B T \Delta f \left( \frac{k_d}{\omega_d Q} + \frac{4R^3(z_p)}{v_{PP}^2 S_{F_d}^2} \right)} \ (Unit: \mathrm{N}) \tag{28}$$

$$z_{pmin} = \sqrt{z_{pmin\_M}^2 + z_{pmin\_E}^2} = \sqrt{4k_B T \Delta f \left( \frac{1}{k_d \omega_d Q} + \frac{4R^3(z_p)}{v_{PP}^2 S_{z_p}^2} \right)} \ (Unit: \mu m) \tag{29}$$

With an assumed bandwidth of 100Hz, the values of noise sources are estimated and summarized in Table 6.3. The sensitivities of the device used in noise estimation are 3.4Ω/mN and 8.0Ω/μm, which are obtained from Eq. (16).

Since the measured minimum resolvable displacement is well above the estimation, the noise of the device is dominated by its interface electronics. Non-ideal mounting and alignment in the experimental setup is believed to play a role as well in determining the measured resolution of the device.

The shot (1/f) noise is not considered here, due to the lack of bias voltage during operation and the number of carriers in a resistive transducer realized by electrolyte [50, 54, 56]. It is worth mentioning that the shot noise could be large or smaller than Johnson noise in a piezo-type resistive transducer, depending on its geometry [50, 54]. Meanwhile, comparison between the expression for load resolution and the expression for sensitivity reveals a design tradeoff between these two performance parameters. A large initial resistance offers a high sensitivity at the cost of a low load resolution, when the electrical noise of the device is dominant. Therefore, the initial resistance needs to be chosen according to specific performance requirement.

Table 6.3 Estimation of the noise in the device #3 with an operation bandwidth of 100Hz when $z_p$=300μm

| Noise types | Value in displacement (μm) | Value in load (mN) |
|---|---|---|
| Mechanical noise | $7.6\times10^{-7}$ | $3.1\times10^{-6}$ |
| Johnson noise | $7.2\times10^{-4}$ | $1.7\times10^{-3}$ |

From the experimental side, load resolution is actually the minimum detectable input load for the device and gives us a concept of how small load this device can detect. Normally, due to the noise from the device and electric circuit, the device's load resolution is limited and need to be distinguished from the noise. Since the total noise in reality is normally larger than that in the theoretic calculation, a lower load resolution than the numerical one is expected.

Owing to the sensitivity dependence on the applied displacement or overall load, the load resolution is expected to vary with the applied displacement or overall load. To measure the load resolution of the device, the probe is first brought down by an initial displacement, and then the probe is moved up or down to find out a minimum applied

displacement, which can be resolved by the transducers. A 10μm increment is found to be the minimum resolvable applied displacement resolvable by the transducers. Figure 6.7 shows the resistance changes of the transducers as a function of time at different initial applied displacements, in response to an increment of 10μm. The same 10μm increment of the applied displacement gives rise to the same load increase of 24mN, but different resistance change ranges (23Ω~62Ω, 32Ω~110Ω and 58Ω~240Ω) for all the transducers at different initial applied displacements (100μm, 300μm and 400μm). This is simply due to linearity of the $F_d$-$z_p$ relation and nonlinearity of the $\Delta R$-$F_d$ relation. The noise in the experiment prevents distinguishing the difference in load resolution of the device at different applied displacements.

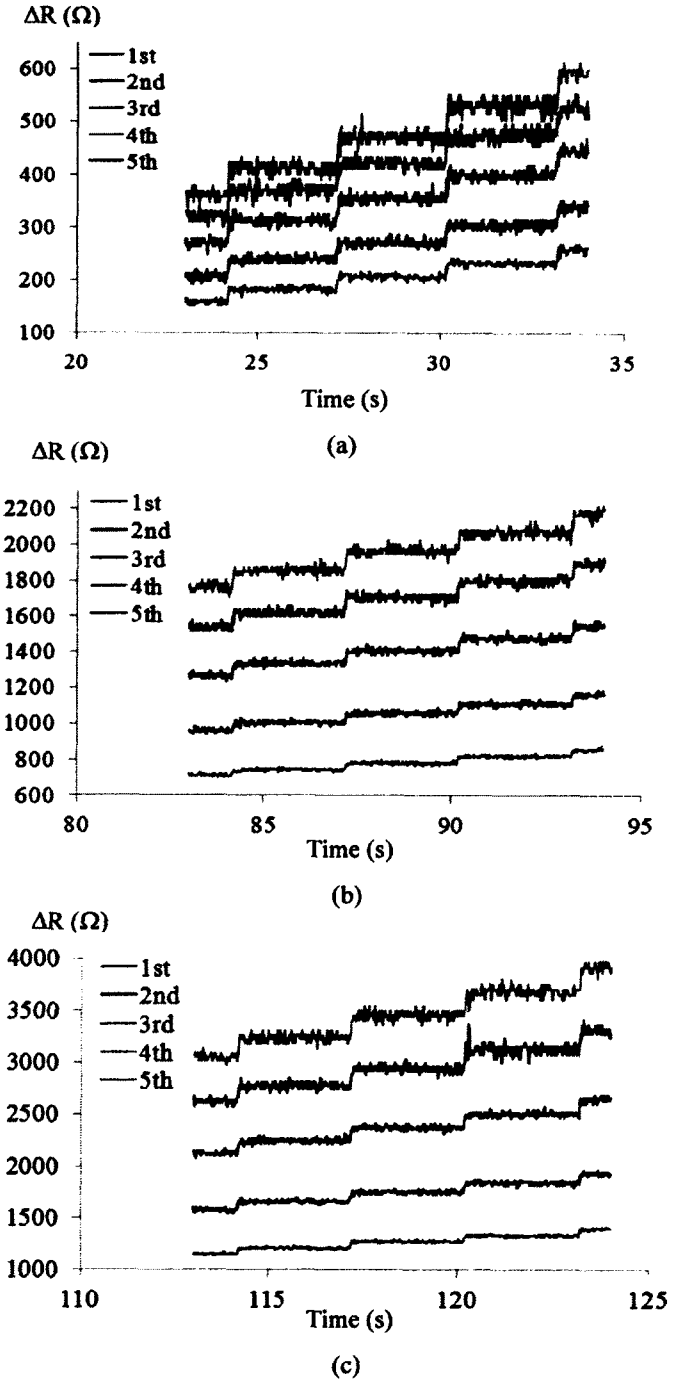


Figure 6.7 Measured load resolution of the device #3 with an input force F=24mN at different initial applied displacements (a) $z_p$=100μm (b) $z_p$=300μm and (c) $z_p$=400μm.

## 6.6 Load range and frequency range

Load range is also a very critical parameter for a device. If we take device #3 as an example, from the previous section, we know that the minimum resolvable applied displacement by the transducers is 10μm for device #3, and this applied displacement responses to an applied load of 24mN. Also from the Figure 5.14, the output voltage of the 5$^{th}$ transducer would not change when the applied displacement reached 460μm. In this case, the microchannel had been squeezed and the top of the microchannel already contacted to the bottom of the channel, and it may damage the device if we applied a larger load. Thus this is the upper bound of the applied load, which is 1.1N. Therefore, the load range for device #3 is 24mN~1.1N. The lower bound of the load range can be smaller by increasing the load resolution, which can be achieved by shrinking the transducer spacing or the dimension of the device; the upper bound can be improved by changing the mixing ratio of the PDMS elastomer base to curing agent base from 1:10 to 1:5 or even larger to increase the Young's modulus of the PDMS microstructure. The upper bound also can be improved by increasing the thickness of the mirochannel or microstructure.

For dynamic response, frequency range is also an important parameter for device. According to the experiments, the device works very well between 0 to 120Hz. Typically, this is the frequency range of the device. Beyond this range, especially for higher frequencies, because the amplitude of the shaker reduced a lot, for instance, lower than the device resolution, this tiny displacement of the shaker cannot be detected by the device. Thus, the detectable frequency is mainly related to the limitation of instruments. This does not mean that the device will not work at a higher frequency, and the frequency

range is related to the load resolution and the limitation of the whole setup. On the other hand, if the frequency is very low, the dynamic performance of the device will be similar to a static performance. In other words, a very low frequency dynamic response will be considered as a static or quasi-static performance. According to the above mentioned reasons, theoretically speaking, if the amplitude of the shaker can be increased in a higher frequency or the device resolution can be improved, the frequency range of the device will also be increased.

# CHAPTER 7

# CONCLUSION AND FUTURE WORK

In this chapter, a conclusion of the dissertation is made and through the study and analysis in this work, a future work can be expected to improve and optimize the performance of this polymer-based microfluidic device with electrolyte-enabled distributed transducers.

## 7.1 Summary of research project

In this section, a summary of this dissertation is made to list a few technical contributions of this research, which includes but is not limited to the following aspects: device design, fabrication, and performance characterization of a polymer-based microfluidic device with electrolyte-enabled distributed transducers (EEDT).

1) Design and development of a polymer-based microfluidic device and detection system. This design makes it possible to detect distributed load in just one single device with a very simple but efficient configuration. Five pairs of electrodes are deposited on the top of a pyrex substrate, a electrolyte-enabled microchannel with two reservoirs is embedded underneath a polymer-based microstructure, and this PDMS microstructure functions as not a confine of the microchannel and reservoirs, more importantly, a detector of the applied displacement. Therefore, this applied displacement can be detected by the microstructure and the electrodes, and then the output can be collected and converted to resistance change by the PCBs and LabVIEW program.

2) Fabrication process. A simple fabrication process is designed and conducted. This fabrication process comprises a lift-off process for depositing the metal layer as the electrodes, a photolithography process for making a SU8 mold and pouring the PDMS microstructure and microchannel, and an oxygen plasma bonding process for bonding the two pieces together. Every step of the process is well developed, easy to fabricate and the costs of the whole procedure are pretty low, making the devices disposable.

3) Device characterization. Three different inputs are introduced to characterize the device responses on static, step and sinusoidal inputs. This type of device demonstrates very stable and reliable performances, not just in static and step response, but also in dynamic response. Combining the potential application in bio-mechanical field, this device is a competitive sensor to detect the distributed load and other material properties. A linear relation exists between the microstructure deflection and the overall load, while the conversion of the microstructure deflection to the resistance changes of the transducers proves to be nonlinear. The experimental method for characterizing the device performance under the three types of loads is well established and can be directly adopted to characterize a material specimen. Each individual device needs to be experimentally characterized for its own $\Delta R$-$z_p$ relation and $\Delta R$-$F_d$ relation to account for unavoidable fabrication variations in the device fabrication, prior to their application for load detection or other application.

4) Performance analysis and data processing method. A comprehensive study is conducted on the performance of a PDMS-based microfluidic device for detection of continuous distributed static and dynamic loads. The performance of the device under static, step and sinusoidal inputs is experimentally analytically examined. After the

specified data processing method, some of the key device performance parameters to the device design parameters have been determined.

## 7.2 Future work

### 7.2.1 Material properties measurement

This device has the potential use of measuring spatial variation of a soft material. In the near future, the design guideline will be laid out for relating the device design parameters to the elasticity/viscoelasticity of vast soft materials with different elasticity/viscoelasticity ranges so that this device is expected to measure the material properties such as elasticity of a homogeneous or heterogeneous specimen, or do the stress relaxation measurement of a soft tissue in both dry and aqueous condition.

### 7.2.2 Configuration modification

Another future use of this device is that this device can be expanded to two-dimension version, instead of one-dimension use. This work can be done by modifying the design configuration and the drawing of the masks, either putting microstructures and the electrodes in arrays or using two or more parallel microstructures.

Also, for different purposes, the device can be modified to different versions to meet the different requirements of the tissue examination. For example, a smaller device can be used to measure micro-scale tissue or even cells.

### 7.2.3 Performance enrichment

Based upon the current design, the performances of the PDMS-based microfluidic device with EEDT need to be enhanced. First, shrinking of the size of the device, the load resolution and the sensitivity of the device could to be increased. Moreover, a higher resolution and higher sensitivity also can improve the frequency response and frequency range for a dynamic response analysis.

Other than that, for biomedical use, a higher spatial resolution is required to get more accurate results. It is expected that by shrinking the dimension of the current design, a higher spatial resolution will be achieved so as not to miss out heterogeneity at smaller scale in a material.

Load range is also a very critical parameter for a device. The load range of the device is related to the thickness of the microstructure. Normally, a thicker microstructure will give a larger load range but the load resolution and sensitivity will be sacrificed. Thus, we need to do the trade-off based upon the requirement of the application.

### 7.2.4 Development of Polyimide-version and hybrid-version devices

Polyimide (PI-2611) -based MEMS device is widely used in different area due to the low stress, high elastic modulus, and the capacity of spin-coating. Dobrzynska et al. [23] utilized polyimide to fabricate a flexible force sensor, and this force sensor can be used to measure a load-induced capacitance change. Xiao et al. [57] utilized polyimide as flexible substrates for MEMS devices. Because of the character of the polyimide, the spin-coating thickness may not be thick enough to support the microstructure, so we may still need PDMS as a structure supporter. Therefore, a polyimide-PDMS hybrid

microfluidic device may be a good choice. Based upon the material, the design and fabrication process may also need to be modified to satisfy the requirement.

# REFERENCES


[1] H. Yousef, M. Boukallel, and K. Althoefer, "Tactile sensing for dexterous in-hand manipulation in robotics—A review," *Sensors and Actuators A: Physical,* vol. 167, pp. 171-187, 2011.

[2] P. Puangmali, K. Althoefer, L. D. Seneviratne, D. Murphy, and P. Dasgupta, "State-of-the-Art in Force and Tactile Sensing for Minimally Invasive Surgery," *Sensors Journal, IEEE,* vol. 8, pp. 371-381, 2008.

[3] M. I. Tiwana, S. J. Redmond, and N. H. Lovell, "A review of tactile sensing technologies with applications in biomedical engineering," *Sensors and Actuators A: Physical,* vol. 179, pp. 17-31, June 2012 2012.

[4] A. Drimus, G. Kootstra, A. Bilberg, and D. Kragic, "Classification of rigid and deformable objects using a novel tactile sensor," in *Advanced Robotics (ICAR), 2011 15th International Conference on,* 2011, pp. 427-434.

[5] R. Ahmadi, M. Packirisamy, J. Dargahi, and R. Cecere, "Discretely Loaded Beam-Type Optical Fiber Tactile Sensor for Tissue Manipulation and Palpation in Minimally Invasive Robotic Surgery," *Ieee Sensors Journal,* vol. 12, pp. 22-32, Jan 2012.

[6] J. S. Mecomber, A. M. Stalcup, D. Hurd, H. B. Halsall, W. R. Heineman, C. J. Seliskar, K. R. Wehmeyer, and P. A. Limbach, "Analytical Performance of Polymer-Based Microfluidic Devices Fabricated By Computer Numerical Controlled Machining," *Analytical Chemistry,* vol. 78, pp. 936-941, 2006/02/01 2005.

[7] H. F. Brinson and L. C. Brinson, *Polymer Engineering science and Viscoelasticity - An Introduction.* New York: Springer, 2008.

[8] A. Kimoto, N. Sugitani, and S. Fujisaki, "A Multifunctional Tactile Sensor Based on PVDF Films for Identification of Materials," *Sensors Journal, IEEE,* vol. 10, pp. 1508-1513, 2010.

[9] C.-H. King, M. O. Culjat, M. L. Franco, C. E. Lewis, E. P. Dutson, W. S. Grundfest, and J. W. Bisley, "Tactile Feedback Induces Reduced Grasping Force in Robot-Assisted Surgery," *IEEE Transactions on,* vol. 2, pp. 103-110, 2009.

[10] S. Schostek, M. O. Schurr, and G. F. Buess, "Review on aspects of artificial tactile feedback in laparoscopic surgery," *Medical Engineering & Physics,* vol. 31, pp. 887-898, 2009.

[11] A. L. Trejos, J. Jayender, M. T. Perri, M. D. Naish, R. V. Patel, and R. A. Malthaner, "Robot-assisted Tactile Sensing for Minimally Invasive Tumor Localization," *The International Journal of Robotics Research,* vol. 28, pp. 1118-1133, September 1, 2009 2009.

[12] B. Kuebler, R. Gruber, C. Joppek, J. Port, G. Passig, J. H. Nagel, and G. Hirzinger, "Tactile feedback for artery detection in minimally invasive robotic surgery-preliminary results of a new approach," *Proc. IFMBE* vol. 25, pp. 299-302, 2009.

[13] D. N. Hohne, J. G. Younger, and M. J. Solomon, "Flexible Microfluidic Device for Mechanical Property Characterization of Soft Viscoelastic Solids Such as Bacterial Biofilms," *Langmuir,* vol. 25, pp. 7743-7751, 2009/07/07 2009.

[14] P. Peng, "Novel MEMS Tactile Sensors for In-Vivo Tissue Characterization Measurements," Ph. D. dissertation, University of Minnesota, 2011.

[15] P. Peng and R. Rajamani, "Handheld Microtactile Sensor for Elasticity Measurement," *Ieee Sensors Journal,* vol. 11, pp. 1935-1942, Sep 2011.

[16] P. Peng, R. Rajamani, and A. G. Erdman, "Flexible Tactile Sensor for Tissue Elasticity Measurements," *Journal of Microelectromechanical Systems,* vol. 18, pp. 1226-1233, Dec 2009.

[17] A. M. R. Fath El Bab, K. Sugano, T. Tsuchiya, O. Tabata, M. E. H. Eltaib, and M. M. Sallam, "Micromachined Tactile Sensor for Soft-Tissue Compliance Detection," *Microelectromechanical Systems, Journal of,* vol. 21, pp. 635-645, 2012.

[18] Y. X. Zhu, Z. X. Dong, U. C. Wejinya, S. Jin, and K. M. Ye, "Determination of mechanical properties of soft tissue scaffolds by atomic force microscopy nanoindentation," *Journal of Biomechanics,* vol. 44, pp. 2356-2361, Sep 2 2011.

[19] B. Lee, L. Han, E. H. Frank, S. Chubinskaya, C. Ortiz, and A. J. Grodzinsky, "Dynamic mechanical properties of the tissue-engineered matrix associated with individual chondrocytes," *Journal of Biomechanics,* vol. 43, pp. 469-476, Feb 10 2010.

[20] V. T. Nayar, J. D. Weiland, C. S. Nelson, and A. M. Hodge, "Elastic and viscoelastic characterization of agar," *Journal of the Mechanical Behavior of Biomedical Materials,* vol. 7, pp. 60-68, Mar 2012.

[21] E. G. Herbert, W. C. Oliver, A. Lumsdaine, and G. M. Pharr, "Measuring the constitutive behavior of viscoelastic solids in the time and frequency domain using flat punch nanoindentation," *Journal of Materials Research,* vol. 24, pp. 626-637, Mar 2009.

[22] I. K. Lin, O. Kuang-Shun, Y.-M. Liao, Y. Liu, C. Kuo-Shen, and X. Zhang, "Viscoelastic Characterization and Modeling of Polymer Transducers for Biological Applications," *Microelectromechanical Systems, Journal of,* vol. 18, pp. 1087-1099, 2009.

[23] J. A. Dobrzynska and M. A. M. Gijs, "Flexible polyimide-based force sensor," *Sensors and Actuators A: Physical,* vol. 173, pp. 127-135, 2012.

[24] H. K. Lee, J. Chung, S. I. Chang, and E. and Yoon, "Real-time measurement of the three-axis contact force distribution using a flexible capacitive polymer tactile sensor," *J. Micromech. Microeng.,* vol. 21, p. 035010, 2011.

[25] M. Lu, J. Xiong, and T. Cui, "A flexible tri-axis contact force sensor for tubular medical device applications," *J. Micromech. Microeng.,* vol. 21, p. 035004, 2011.

[26] C. A. Gutierrez and E. Meng, "Impedance-Based Force Transduction within Fluid-Filled Parylene Microstructures," *J. Micromech. Microeng.,* vol. 20, pp. 1098-1108, 2011.

[27] W.-Y. Tseng, J. S. Fisher, J. L. Prieto, K. Rinaldi, G. Alapati, and A. P. Lee, "A slow-adapting microfluidic-based tactile sensor," *J. Micromech. Microeng.,* vol. 19, p. 085002, 2009.

[28] Y.-L. Park, C. Majidi, R. Kramer, P. Berard, and R. J. Wood, "Hyperelastic pressure sensing with a liquid-embedded elastomer," *J. Micromech. Microeng.,* vol. 20, p. 125029, 2010.

[29] M. R. Buckley, L. J. Bonassar, and I. Cohen, "Localization of Viscous Behavior and Shear Energy Dissipation in Articular Cartilage Under Dynamic Shear Loading," *Journal of Biomechanical Engineering,* vol. 135, p. 031002, 2013.

[30] E. M. Darling, R. E. Wilusz, M. P. Bolognesi, S. Zauscher, and F. Guilak, "Spatial Mapping of the Biomechanical Properties of the Pericellular Matrix of Articular Cartilage Measured In Situ via Atomic Force Microscopy," *Biophysical Journal,* vol. 98, pp. 2848-2856, Jun 16 2010.

[31] M. A. McLeod, R. E. Wilusz, and F. Guilak, "Depth-dependent anisotropy of the micromechanical properties of the extracellular and pericellular matrices of articular cartilage evaluated via atomic force microscopy," *Journal of Biomechanics,* vol. 46, pp. 586-592, Feb 1 2013.

[32] S. Neethirajan, I. Kobayashi, M. Nakajima, D. Wu, S. Nandagopal, and F. Lin, "Microfluidics for food, agriculture and biosystems industries," *Lab on a Chip,* vol. 11, pp. 1574-1586, 2011.

[33] A. V. Jagtiani, J. Carletta, and J. Zhe, "A microfluidic multichannel resistive pulse sensor using frequency division multiplexing for high throughput counting of micro particles," *Journal of Micromechanics and Microengineering,* vol. 21, Jun 2011.

[34] C. Liu, "Recent Developments in Polymer MEMS," *Advanced Materials,* vol. 19, pp. 3783-3790, 2007.

[35] B. Nie, S. Xing, J. D. Brandt, and T. Pan, "Droplet-based interfacial capacitive sensing," *Lab on a Chip,* vol. 12, pp. 1110-1118, 2012.

[36] C.-Y. Wu, W.-H. Liao, and Y.-C. Tung, "Integrated ionic liquid-based electrofluidic circuits for pressure sensing within polydimethylsiloxane microfluidic systems," *Lab on a Chip,* vol. 11, pp. 1740-1746, 2011.

[37] H. B. Muhammad, C. M. Oddo, L. Beccai, C. Recchiuto, C. J. Anthony, M. J. Adams, M. C. Carrozza, D. W. L. Hukins, and M. C. L. Ward, "Development of a bioinspired MEMS based capacitive tactile sensor for a robotic finger," *Sensors and Actuators A: Physical,* vol. 165, pp. 221-229, Februry 2011.

[38] R. D. Ponce Wong, J. D. Posner, and V. J. Santos, "Flexible microfluidic normal force sensor skin for tactile feedback," *Sensors and Actuators A: Physical,* vol. 179, pp. 62-69, 2012.

[39] N. Wettels, V. J. Santos, R. S. Johansson, and G. E. Loeb, "Biomimetic Tactile Sensor Array," *Advanced Robotics,* vol. 22, pp. 829-849, 2008.

[40] W. T. Gu, P. Cheng, A. Ghosh, Y. X. Liao, B. X. Liao, A. Beskok, and Z. L. Hao, "Detection of distributed static and dynamic loads with electrolyte-enabled distributed transducers in a polymer-based microfluidic device," *Journal of Micromechanics and Microengineering,* vol. 23, Mar 2013.

[41] A. V. Jagtiani, J. Carletta, and J. A. Zhe, "An impedimetric approach for accurate particle sizing using a microfluidic Coulter counter," *Journal of Micromechanics and Microengineering,* vol. 21, Apr 2011.

[42] W. Gu, P. Cheng, A. Ghosh, Y. Liao, B. Liao, A. Beskok, and Z. Hao, "A Polymer-based microfluidic resistive sensor for detecting distributed loads," presented at the Proceedings of the ASME 2012 International Mechanical Engineering Congress & Exposition IMECE2012, Houston, Texas, USA, 2012.

[43] R. S. Lakes, "Viscoelastic measurement techniques," *Review of Scientific Instruments,* vol. 75, pp. 797-810, 2004.

[44] P. Du, C. Cheng, H. B. Lu, and X. Zhang, "Investigation of Cellular Contraction Forces in the Frequency Domain Using a PDMS Micropillar-Based Force Transducer," *Journal of Microelectromechanical Systems,* vol. 22, pp. 44-53, Feb 2013.

[45] F. B. Seely and J. O. Smith, *Advanced Mechanics of Materials*: Wiley & Sons, 1963.

[46] D. J. Beebe, G. A. Mensing, and G. M. Walker, "PHYSICS AND APPLICATIONS OF MICROFLUIDICS IN BIOLOGY," *Annual Review of Biomedical Engineering,* vol. 4, pp. 261-286, 2002.

[47] J. D. Stenger-Smith and J. A. Irvin. (2009). *Ionic Liquids for Energy Storage Applications.* Available: http://www.sigmaaldrich.com/china-mainland/zh/technical-documents/articles/material-matters/ionic-liquids-for.html

[48] H. Hocheng, C.-M. Chen, Y.-C. Chou, and C.-H. Lin, "Study of novel electrical routing and integrated packaging on bio-compatible flexible substrates," *Microsystem Technologies,* vol. 16, pp. 423-430, 2010/03/01 2010.

[49] V. J. Cadarso, J. A. Plaza, K. Zinoviev, C. Dominguez, S. de Pedro, S. Buttgenbach, and A. Llobera, "Cantilever-Based Poly(dimethylsiloxane) Microoptoelectromechanical Systems," *2009 Ieee Sensors, Vols 1-3,* pp. 413-417, 2009.

[50] J. C. Doll, S.-J. Park, and B. L. Pruitt, "Design optimization of piezoresistive cantilevers for force sensing in air and water," *Journal of Applied Physics,* vol. 106, pp. 064310-064310-12, 2009.

[51] J. H. Ni, F. L. Huang, B. Wang, B. Z. Li, and Q. A. Lin, "A planar PDMS micropump using in-contact minimized-leakage check valves," *Journal of Micromechanics and Microengineering,* vol. 20, Sep 2010.

[52] G. F. Franklin, J. D. Powell, and B. Emami-naeini, *Feedback Control of Dynamic Systems*. Englewood Cliffs, NJ: Prentice Hall, 2009.

[53] W. Gu, P. Cheng, A. Ghosh, Y. Liao, B. Liao, A. Beskok, and Z. Hao, "Detection of distributed static and dynamic loads with electrolyte-enabled distributed transducers in a polymer-based microfluidic device," *Journal of Micromechanics and Microengineering,* vol. 23, p. 035015, 2013.

[54] Z. Xiong, B. Walter, E. Mairiaux, M. Faucher, L. Buchaillot, and B. Legrand, "MEMS ring resonators for laserless AFM with sub-nanoNewton force resolution," *J. Microelectromech. Syst.,* vol. 21, p. 385, 2012.

[55] G. Tosolini, L. G. Villanueva, F. Perez-Murano, and J. Bausells, "Fast on-wafer electrical, mechanical, and electromechanical characterization of piezoresistive cantilever force sensors," *Review of Scientific Instruments,* vol. 83, pp. 015002-015002-7, 2012.

[56] J. A. Harley and T. W. Kenny, "1/F noise considerations for the design and process optimization of piezoresistive cantilevers," *Journal of Microelectromechanical Systems,* vol. 9, pp. 226-235, Jun 2000.

[57] S. Y. Xiao, L. F. Che, X. X. Li, and Y. L. Wang, "A novel fabrication process of MEMS devices on polyimide flexible substrates," *Microelectron. Eng.,* vol. 85, pp. 452-457, 2008.

# VITA

Peng Cheng received his Bachelor of Engineering in Mining Engineering and Master of Engineering in Safety Engineering and Technology from Xi'an University of Science and Technology in 1996 and 2008, respectively. He worked in Xi'an University of Science and Technology after undergraduate graduation in 1996. He is currently a PhD candidate in the Department of Mechanical and Aerospace Engineering, Old Dominion University, Norfolk, USA. His research interests are on MEMS sensors design, simulation and development, performance study and applications of a polymer-based microfluidic device for distributed load detection.